SYNTHESIS AND MAGNETIC PROPERTIES OF HIGH-ASPECT-RATIO NANOCRYSTALS

by

KINJAL GANDHA

Presented to the Faculty of the Graduate School of
The University of Texas at Arlington in Partial Fulfillment
of the Requirements
for the Degree of

DOCTOR OF PHILOSOPHY

THE UNIVERSITY OF TEXAS AT ARLINGTON
December 2015

Acknowledgements

I would like to express my gratitude to my advisor Dr. J. Ping Liu for his support and guidance throughout this thesis. I would also like to thank Professors Alex Weiss, Ali R. Koymen, Qiming Zhang and Yaowu Hao for serving in my dissertation committee. I appreciate creative discussions with my past and present colleagues Dr. Narayan Poudyal, Dr. Kevin Elkins, Dr. Xubo Liu, Dr. Nguyen Van Vuong, Dr. Yilong Ma, Dr. Guangbing Han, Dr. Xianghua Han, Dr. Jason Zhang, Dr. Wei Wang, Dr. Jinjun Liu, Dr. Zhao Guoping, Dr. Dapeng Wang, Ke wang, Hai In Choi and Zhaoguo Qiu.

I would also like to thank our collaborators, Dr. Ray Baughman, Dr. Anvar Zakhidov and Dr. Ali Aliev from University of Texas at Dallas for their help in providing SQUID and PPMS facility. I am thankful to Dr. Jiechao Jiang from Characterization Center for Materials and Biology at UTA for the technical support he provided with operating TEM and SEM. I appreciate Dr. Weixing Xia and Dr. “Max” Qinhong Hu for their help in holography and ICP measurements. I also appreciate Professor Frederick MacDonnell and Fakrul Islam for their help in BET measurements.

Most of all, I want to thank my husband Rakesh, who more than anyone has provided inspiration, counsel, friendship and love. This work is dedicated to him. I finally would like to thank my family in India for supporting me throughout my studies.

November 20, 2015

Abstract

SYNTHESIS AND MAGNETIC PROPERTIES OF HIGH-ASPECT-RATIO NANOCRYSTALS

Kinjal Gandha, PhD

The University of Texas at Arlington, 2015

Supervising Professor: J. Ping Liu

The aim of this thesis is to synthesize and investigate the structural and magnetic properties of anisotropic nanostructures in particular, nanowires and nanorods of Fe, Co, and bimetallic systems (FeCo, CoNi) and ferrites ($CoFe_2O_4$, Fe_3O_4) that have potential applications in rare-earth-free magnets, biomedical materials and magnetic recording devices. Anisotropic nanostructures with high aspect ratio were synthesized via bottom-up approach using chemical solution methods. The size and shape of the nanostructures were found to be dependent on experimental parameters such as the catalyst concentration, the surfactant ratio, the precursor concentration and the heating rate. It was observed that the uniformity in morphology, structure and composition of the nanowires was the key to achieving a high coercivity. In case of bcc Fe and FeCo nanowires, coercivity is mostly determined by shape anisotropy that results in moderate coercivity. On other hand, Co and CoNi nanowires with hcp crystallographic structure give extraordinarily high magnetic hardening, especially when the wires are aligned. Record high coercivity up to 12.5 kOe has been achieved in our experiments (corresponding to an energy product of >40 MGOe if full density is counted) which is significantly higher than any Co-based bulk or thin film materials reported to date. It has been found that the shape anisotropy plays an essential role in the magnetic hardening when the wire's long axis is along the c-axis of the hcp crystals.

We also present in this study the structural and magnetic properties of high aspect ratio Co nanowires at high temperatures (up to 650 K) using PPMS characterizations. We show that the anisotropic shapes, the structural and texture properties are preserved up to 500 K.

The magnetization reversal process in the single-crystalline nanowires was also investigated by measuring the angular dependence of the coercivity and comparing with the Stoner-Wohlfarth model. It was observed that the magnetization reversal in Co nanowires is proceeded via a coherent rotation process. In addition, surface oxidized Co nanowires have provided us a unique opportunity to study the exchange bias in the aligned Co/CoO core-shell nanostructures. Study of temperature and angular dependence of the exchange bias field and the coercive field in the Co/CoO core-shell nanowires underlines the importance of the interplay of the different magnetic anisotropy at the interface. Ferromagnetic nanowires of this type are ideal building blocks for future bonded, consolidated and thin film magnets with high energy density and high thermal stability.

Table of Contents

List of Figures

List of Tables

Chapter 1

Magnetism and Magnetic Materials

This section provides some basics about the field of magnetism. It starts with magnetism in atom to end with magnetism in fine particle such as the nanowires which have been investigated in this work.

Lots of progress arose from Quantum Mechanics which allowed to understand magnetism far deeper. Goudsmit and Uhlenbeck demonstrated in 1925 [1, 2] that an electron carries an intrinsic quantum mechanical angular moment named spin which contributes, together with the orbital angular moment, to the magnetic moment of the atom. The next step came from Heisenberg [3] and Dirac [4] who independently understood in 1926 that the interaction between two spins was given by

$$H = -J\,\overrightarrow{S_1}.\overrightarrow{S_2} \qquad (1.1)$$

where *H* is the Hamiltonian describing the interaction, *J* the exchange coupling constant and $\overrightarrow{S_1}$ and $\overrightarrow{S_2}$, the two interacting spins.

1.1 Origin of Magnetic Moments

Magnetism arises from two types of motions of electrons in atoms: one is the motion of the electrons in an orbit around the nucleus, similar to the motion of the planets in our solar system around the sun, and the other is the spin of the electrons around its axis, analogous to the rotation of the Earth about its own axis. The orbital and the spin motion independently impart a magnetic moment on each electron causing each of them to behave as a tiny magnet.

The expression of the amplitude of the magnetic orbital momentum $|\vec{L}|$ and its z-component $\vec{L}|^{z}$ are:

$$|\vec{L}| = \gamma\hbar[l(l+1)]^{\frac{1}{2}}, \qquad (1.2)$$

$$\vec{L}|^{z} = \gamma\hbar m_l, \qquad (1.3)$$

where γ is the gyromagnetic factor, l the orbital angular momentum quantum number and m_l the integer value comprised between $-l$ and l.

The second origin of magnetic moments comes from of spin angular momentum of electrons. The spin magnetic moment $|\vec{s}|$ is proportional to the spin momentum $|\vec{S}|$:

$$|\vec{S}| = \gamma\hbar[s(s+1)]^{\frac{1}{2}} , \tag{1.4}$$

$$\vec{S}|^{Z} = \gamma\hbar m_s , \tag{1.5}$$

where s is the spin quantum number and m_s the integer value comprised between $-s$ and s.

1.2 Spin–Orbit Coupling

Generally, an atomic electron possesses both spin and orbital angular momentum. They may be coupled by spin–orbit interaction to create a total electronic angular momentum $\vec{J}$, defined as

$$\vec{J} = \vec{L} + \overrightarrow{S} \tag{1.6}$$

A qualitative description is given by the Hund's rule. For the absolute value and the z-component of the angular momentum in case of the Russel-Saunders coupling we have

$$|\vec{J}| = \gamma\hbar[J(J+1)]^{\frac{1}{2}} , \tag{1.7}$$

$$\vec{J}|^{Z} = \gamma\hbar m_j , \tag{1.8}$$

where $m_j = -J, -(J-1), -(J-2), \ldots..J-2, J-1, J$ analogously to the behavior of the orbital momentum.

For the respective magnetic moment we get:

$$\mu = -g.\ \mu_B.\left[\vec{J}(\vec{J}+1)\right]^{\frac{1}{2}} , \tag{1.9}$$

$$\mu_z = g.\ \mu_B.\ m_j, \tag{1.10}$$

where the so called Lande-Factor g takes the following values:

$$g = 1 + \frac{\vec{J}(\vec{J}+1)+\vec{S}(\vec{S}+1)-\vec{L}(\vec{L}+1)}{2\vec{J}(\vec{J}+1)} , \tag{1.11}$$

The magnetic susceptibility χ, the magnetic response of a material to an external stimulus, can be expressed in terms of the magnetic moment per unit volume, known as the magnetization M, and the magnetic field strength H. The magnetic flux density B is related to the magnetic field strength H by $B = \mu_0(H + M)$. As above, for a material with a linear magnetic susceptibility in a small magnetic field the following expression is true (μ_0 and k_B are the permeability of free space and Boltzmann constants respectively):

$$\chi = \frac{M}{H} \approx \frac{\mu_0 M}{B} = \frac{\mu_0 \mu^2}{3k_B T} \qquad (1.12)$$

In fact, equation 1.12 is a statement of Curie's law, which states that magnetic susceptibility of a material is proportional to the inverse of the temperature. A system, in which Curie's law is valid, where the moments tend to align with any applied magnetic field, is known as paramagnetic. The magnetic moments associated with unpaired electrons in paramagnetic systems can be considered independent and are therefore randomly aligned in zero magnetic field. Applying a magnetic field causes the spins to align parallel to the field direction, depending on the strength of the applied field, until in a high enough field all the moments are aligned and the magnetization becomes saturated. An example of a paramagnet in a small applied magnetic field is illustrated in Figure 1.1.

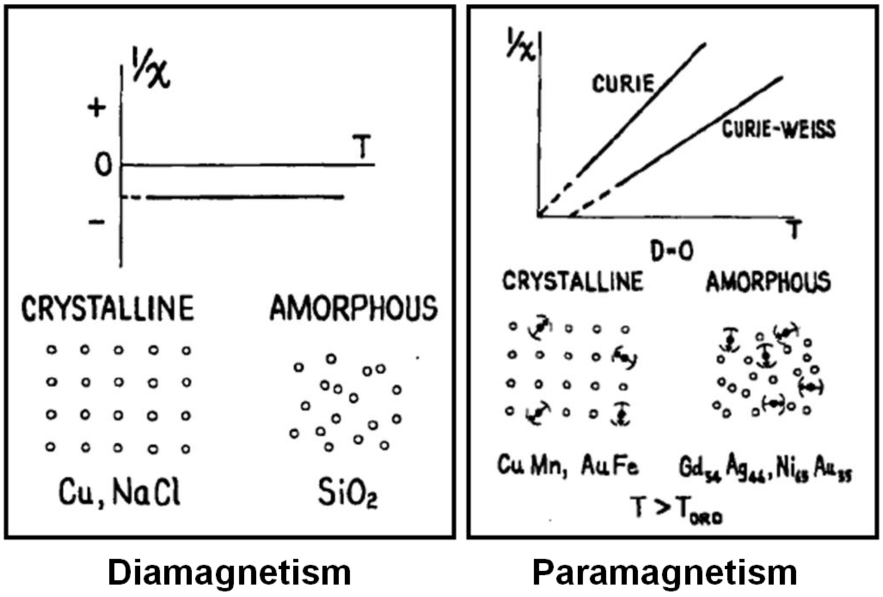

Figure 1.1 Diamagnetism and Paramagnetism [5].

In most systems, the orbital angular momentum L and intrinsic spin S interact, albeit weakly, splitting into a number of levels with different J known as the fine structure. The total angular momentum J, given in equation 1.6, is conserved through this process. The values of S, L and J for a particular atom which minimize the energy can be estimated using Hund's rules, which give an empirical prediction of the ground state of an ion.

Hund's Rules

(1) Maximise S

(2) Maximise L

(3) If the shell is less than half full $J = | L - S |$

If the shell is more than half full $J = | L + S |$

It is also necessary to consider how the magnetic moments on neighbouring atoms interact with each other. This is via an exchange interaction, which will be discussed in section 1.9. These interactions can result in a variety of different kinds of long-range magnetic order such as ferromagnetism, ferrimagnetism and antiferromagnetism. Some of these are illustrated in Figure 1.2.

Ferromagnetic systems have a Curie temperature T_C below which ferromagnetism onsets. It is related to the susceptibility by the Curie-Weiss law:

$$\chi \propto \frac{1}{T - T_C} \qquad (1.13)$$

Cobalt metal is an itinerant ferromagnet, it has a spontaneous magnetization without an applied magnetic field due to the splitting of the electron energy bands at the Fermi level. The Curie temperature for cobalt metal T_C = 1394 K with magnetic moment of μ = 1.715 μB/f.u.

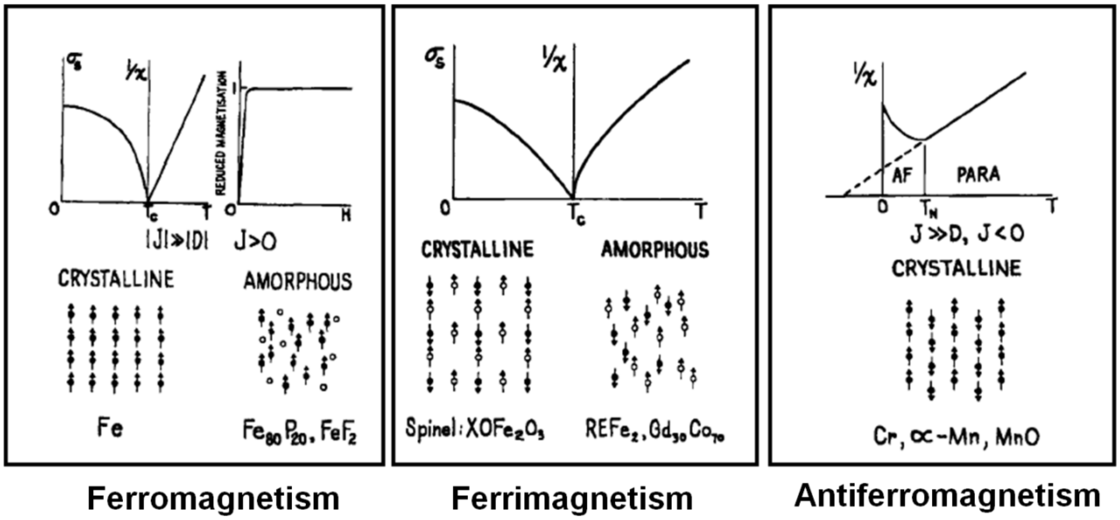

Figure 1.2 Some possible types of long-range magnetic order. Ferromagnetism, Ferrimagnetism, Anti-ferromagnetism [5].

In an antiferromagnet, the critical temperature is known as the Neel temperature T_N, and in this case $T_C = -\Theta$ in equation 1.13. We therefore expect $\Theta = -T_N$. Below T_N, the magnetic moments lie antiparallel to their nearest neighbours. In a crystal lattice the situation is further complicated as these are several possible ways of arranging an equal number of antiparallel spins on a cubic lattice, discussed in section 1.9.

The magnetic properties of a crystal are governed by a competition between different energies. The configurations of the magnetic moments are indeed driven by the energy minimization of the system. The different energies in play are described below.

1.3 The Zeeman Energy

The Zeeman energy is often referred to as the magnetic potential energy, which is simply the energy of the magnetization in an externally applied magnetic field. The Zeeman energy is always minimized when the magnetization is aligned with the applied field; it can be expressed as

$$E_z = -\vec{M}.\vec{H}, \tag{1.14}$$

where $\vec{H}$ is the external field and $\vec{M}$ is the magnetization vector.

Two important and common sources of anisotropy, which are magnetocrystalline anisotropy and shape anisotropy, are discussed next.

1.4 Magnetocrystalline Anisotropy

In a magnetic material, the electron spin is coupled to the electronic orbital (spin orbital coupling) and influenced by the local environment (crystalline electric field). Because of the arrangement of atoms in crystalline materials, magnetization along certain orientations is energetically preferred. Magnetocrystalline anisotropy is an intrinsic property. The magnetization process is different when the field is applied along different crystallographic directions, and the anisotropy reflects the crystal symmetry. For a cubic crystal, the anisotropy energy is often expressed as

$$E_{MC} = K_0 + K_1(cos^2\theta_1 cos^2\theta_2 + cos^2\theta_2 cos^2\theta_3 + cos^2\theta_3 cos^2\theta_1)$$
$$+K_2 cos^2\theta_1 cos^2\theta_2 cos^2\theta_3 + \ldots\ldots\ldots\ldots \qquad (1.15)$$

where $K_0, K_1, K_2 \ldots$ are anisotropy constants θ_1, θ_2 and θ_3 are the angles between the magnetization direction and the three crystal axes, respectively. K_0 is independent of angle and can be ignored since it is the difference in energy between different crystal orientations that is of interest. In many cases, terms involving K_2 are small and can also be neglected.

The magnetocrystalline anisotropy energy associated with a hexagonal close-packed crystal is expressed as

$$E_{MC} = K_0 + K_1 sin^2\theta + K_2 sin^4\theta \qquad (1.16)$$

where K_0, K_1, and. K_2 are anisotropy constants and θ is the angle between the magnetization direction and the *c*-axis. If $K_1 > 0$, the energy is smallest when $\theta = 0$, i.e., along the c-axis, so that this axis is the easy axis. If $K_1 < 0$, the basal plane is the easy axis. As a result of the symmetry of the hexagonal close-packed lattice, the magnetocrystalline anisotropy is a uniaxial anisotropy. Examples of K_1 for various bulk materials are given in Table 1-1

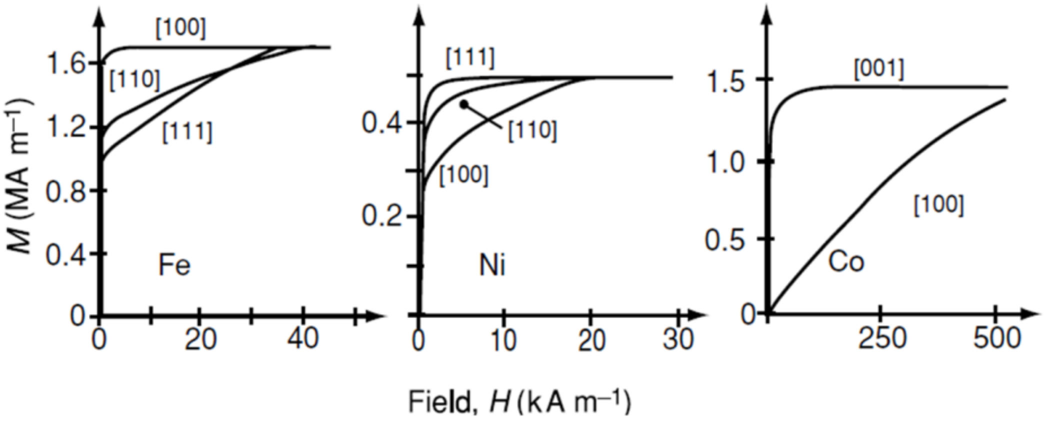

Figure 1.3 Magnetization of single crystals of Fe, Ni and Co [7].

Table 1-1 Magnitude of the magnetocrystalline anisotropy constants K_1 and K_2 of Fe, Ni and Co at room temperature [6].

Material	K_1(J/m^3)	K_2(J/m^3)
bcc-Fe	4.8×10^4	-0.5×10^4
fcc-Ni	$- 0.5 \times 10^4$	$- 0.2 \times 10^4$
hcp-Co	4.5×10^5	1.5×10^5

1.5 Shape Anisotropy

The magnetization of a spherical object in an applied magnetic field is independent on the orientation of the applied field. However, it is easier to magnetize a non spherical object along its long axis than along its short axis. If a rod-shaped object is magnetized with a north pole at one end and a south pole at the other, the field lines emanate from the north pole and end at the south pole. Inside the material the field lines are oriented from the north pole to the south pole and hence they are opposed to the magnetization of the material, since the magnetic moment points from the south pole to the north pole. Thus, the magnetic field inside the material tends to demagnetize the material and is known as the demagnetizing field $\overrightarrow{H_d}$.

In uniformly magnetized ellipsoids, if the magnetization lies along a principle direction, then the demagnetizing field is also uniform and given by:

$$\overrightarrow{H_d} = -N\vec{M}, \qquad (1.17)$$

where N is the demagnetizing factor and is dependent on the shape of the body, but can only be calculated exactly for an ellipsoid where the magnetization is uniform throughout the sample.

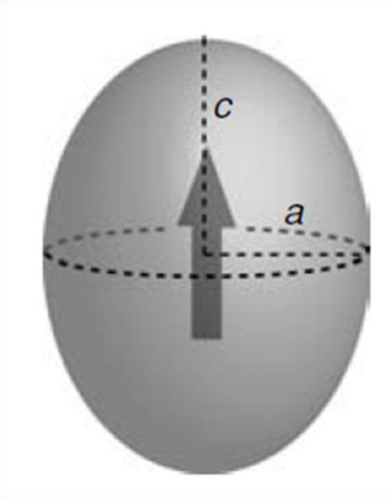

Figure 1.4 Magnetization of a prolate ellipsoid of revolution with c > a and no magnetocrystalline anisotropy. The c axis is the easy direction of magnetization [7].

The energy of demagnetizing field then becomes:

$$E_d = \frac{1}{2}\mu_0 V\vec{M}N\vec{M}, \qquad (1.18)$$

where V is the volume of the ellipsoid.

Other simple shapes can be approximated to ellipsoids. The anisotropy energy is related to the difference in energy ΔE_d when the ellipsoid is magnetized along its hard and easy directions. N is the demagnetizing factor for the easy direction; $N' = \frac{1}{2}(1 - \mathrm{N})$ is the demagnetizing factor for the perpendicular, hard directions (Table 1-2). Hence$\Delta E_d = \frac{1}{2}\mu_0 V M^2 \left[\frac{1}{2}(1 - N) - N\right]$, this gives for a prolate ellipsoid

$$K_{sh} = \frac{1}{4}\mu_0 M^2(1 - 3N) \qquad (1.19)$$

This is zero for a sphere $\left(N = \frac{1}{3}\right)$, as expected. Shape anisotropy is only fully effective in samples which are so small that they do not break up into domains.

Table 1-2 Demagnetizing factors N for finite rods magnetized parallel to long axis [8].

Aspect ratio (length/diameter)	*N*
0	1
1	0.27
2	0.14
5	0.04
10	0.0172
20	0.00617

1.6 Magnetic Domains

Many magnetic materials do not exhibit any magnetization if no external magnetic field is applied. Weiss attributed this “absence” of magnetism to the formation of domains in polycrystals: domains are magnetized in different directions so that the average net magnetization is almost zero.

The alignment of the different magnetic dipoles in a superparamagnetic, ferromagnetic or ferrimagnetic material creates a magnetic field in space that is associated to an energy value. This energy can be minimized by creating oppositely faced domains in the material, so that the field, and consequently also the energy, are decreased. The so-called ‘‘domain walls’’ that are thus created carry a certain value of energy associated as well.

The formation of domains is in fact governed by the minimization of the total energy *E*:

$$\mathrm{E} = \mathrm{E_z} + \mathrm{E_d} + \mathrm{E_{MC}} + \mathrm{E_{ex}}, \qquad (1.20)$$

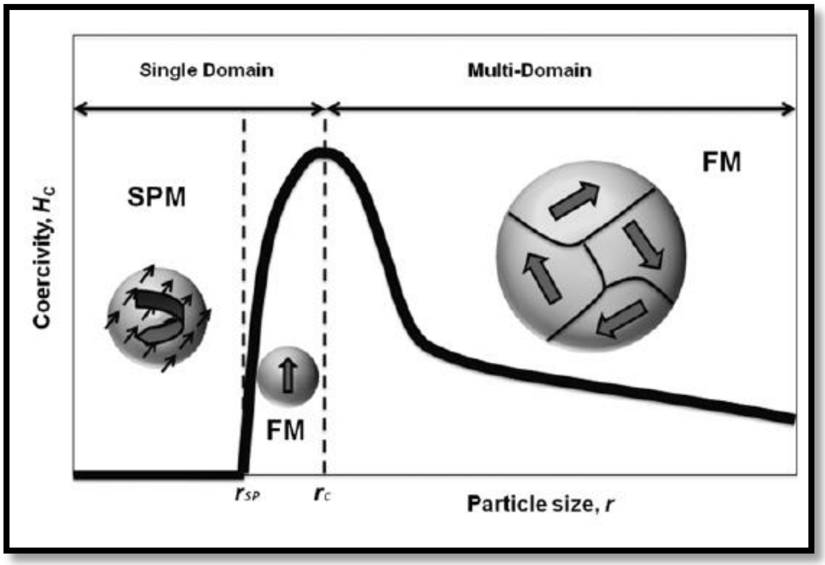

Figure 1.5 Size dependence of the coercivity of magnetic nanoparticles. The size-dependent transitions between magnetic single and multidomains [9].

Domain walls are the region between the domains. Classification of domain walls can be made according to the angle between two adjacent domains. As shown in Figure 1.6, a 180° domain wall separates domains of opposite magnetizations and a 90° domain wall separates domains with perpendicular magnetizations.

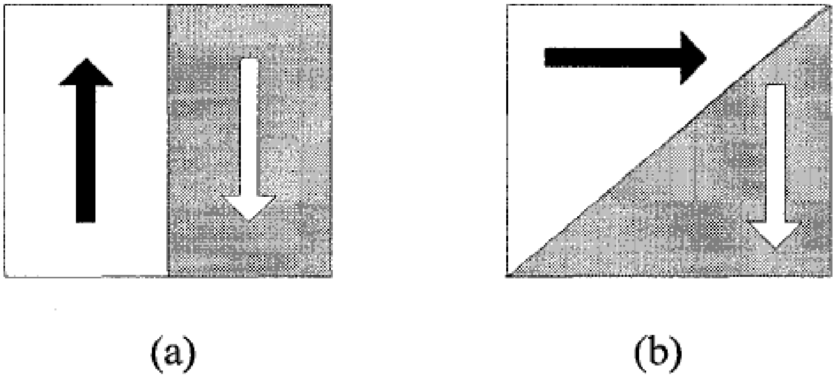

Figure 1.6 (a) 180° domain wall, (b) 90° domain wall.

The most common type of 180° domain wall is a Bloch wall in which the magnetization rotates in the plane parallel to the domain wall. The other possible configuration is the Neel wall where the magnetization in the domain wall rotates in a plane perpendicular to the plane of the wall.

It must be noted that Néel walls mainly concern surface geometry. As for Bloch walls, in the case of uniaxial magnetocrystalline anisotropy and of infinite wall, their width is given by the Bloch wall width. In a ferromagnet it costs energy to rotate the spins. In terms of exchange stiffness *A* and anisotropy constant *K* the domain wall energy for a Bloch type of wall is

$$\sigma_{BW} = \pi\sqrt{AK} \qquad (1.21)$$

where the domain wall thickness is $\delta_B = \pi\sqrt{A/_K}$.

Formation of domains saves energy associated with dipolar fields. The dipolar energy can be saved by breaking the system into domains. Whereas each domain formed costs energy due to the formation of domain walls. Dipolar energy can also determine the type of domain created. The Bloch wall is favored in bulk samples since it leads to smaller dipolar energy. However, Neel type domain wall is favored in thin films where there is an energy cost to rotate the spins out of the film plane.

1.7 Magnetism in Single-Domain Particle

Technological applications of single-domain magnetic particles depend critically on our fundamental understanding of spin rotation dynamics and their dependence on the particle's intrinsic spin structure. The simplest model proposed by Stoner and Wohlfarth [10] in their pioneering work on moment reversal in single-domain magnetic particles, assumes coherent spin rotation whereby all spins within the single-domain particle are collinear and rotate in unison. It predicts the field strength necessary to reverse the spin orientation direction or coercive field, H_C. The model assumes uniform magnetization throughout the particle, which remains so throughout the rotation process, an assumption that allows for exact solutions, but not generally observed experimentally. Additional models, allowing for non-uniform, incoherent spin reversal mechanisms have also been developed [11-14]. Generally the energies required to reverse the spin orientation within a single-domain particle are larger than those needed to induce domain wall movement, yielding coercivity larger than those of the bulk. Figure 1.7 shows the dependence of coercivity as a function of particle size for Co, Fe and iron oxide particles reproduced from the classic paper by Luborsky [15].

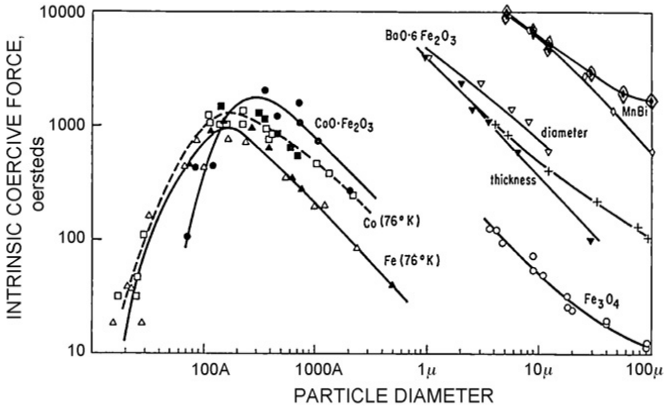

Figure 1.7 Experimental relation between coercivity and diameter for particles deriving their coercive force principally from crystal anisotropy energy.

1.8 Stoner–Wohlfarth Model

The Stoner–Wohlfarth model is the simplest analytical model which exhibits hysteresis and describes magnetization reversal in single-domain particles. Imagine a Stoner–Wohlfarth particle, a uniformly magnetized ellipsoid with uniaxial anisotropy of shape or magnetocrystalline origin in a field applied at an angle α to the anisotropy axis.

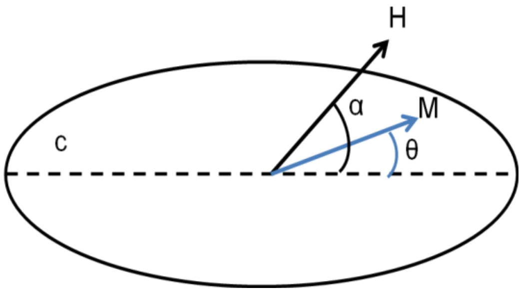

Figure 1.8 The Stoner-Wohlfarth geometry: definition of θ and α.

The energy density is given by

$$E = E_{MC} + E_{shape} + E_Z = [(K_{MC} + K_{sh})sin^2\theta - \mu_0 M_s H\, cos(\alpha - \theta)]V \qquad (1.22)$$

The hysteresis cycle as a function of the angle α between H and the easy axis C can be calculated. Figure 1.9 shows that the value of the coercive field is strongly affected by the angle α. Note that when the particles are aligned along the magnetic field H the coercive field is the sum of two contributions, one from the magnetocrystalline anisotropy H_{MC} and another one from the shape anisotropy H_{shape}.

$$H = H_{MC} + H_{shape} = \frac{2K_{MC}}{\mu_0 M_s} + \frac{1}{2}(1 - 3N)M_s \qquad (1.23)$$

where K_{MC} is the anisotropy constant, M_s the saturation magnetization and N the demagnetizing factor. N = 1⁄3 for spheres and N = 0 for infinite cylinders. Some more accurate values of N as a function of the length and the radius of the cylinder are given in Table 2-2.

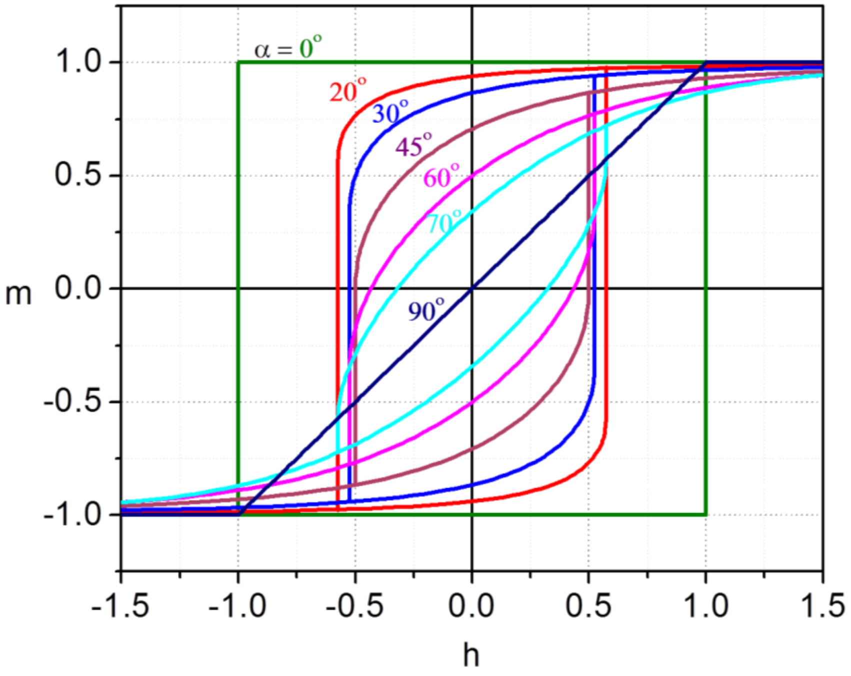

Figure 1.9 Hysteresis loops for single domain particles with uniaxial anisotropy; α is the angle between the field and the easy axis.

Stoner and Wohlfarth also calculated the hysteresis loop of an assembly of noninteracting particles, with their easy axes randomly oriented in space so that the assembly as a whole is magnetically isotropic (Figure 1.9). Secondly, Figure 1.10 shows that the remanence of randomly oriented particles is 0.5 M_s. This value strongly depends on the dimensionality of the system.

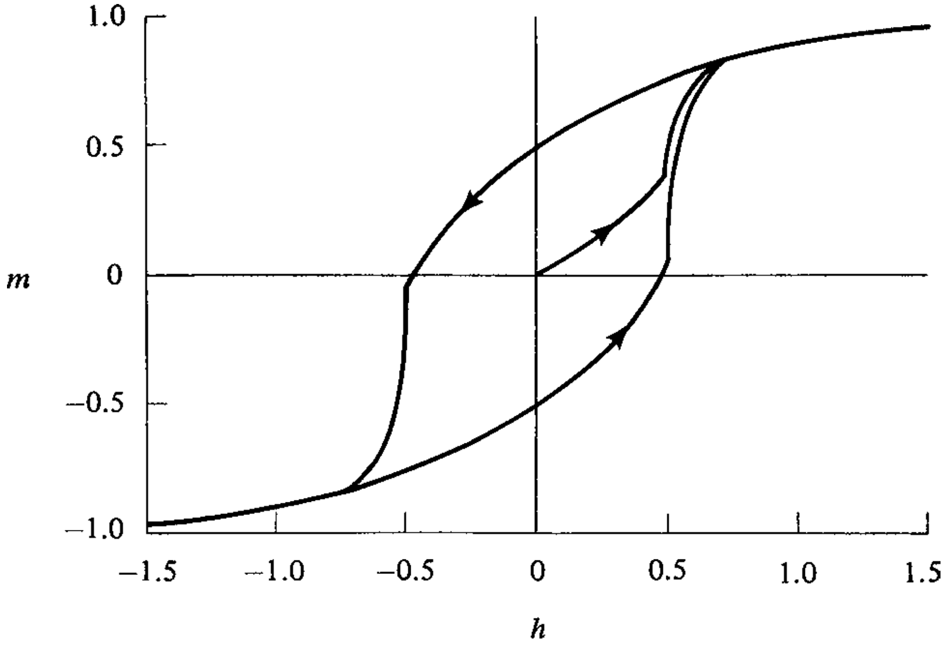

Figure 1.10 Hysteresis loop of an assembly of noninteracting, randomly oriented, uniaxial single domain particles.

Furthermore, the original Stoner-Wohlfarth model only takes the uniaxial shape or uniaxial magnetocrystalline anisotropies into account. Therefore depending on the studied system, the other anisotropies such as the magnetocrystalline, the magnetoelastic or the surface ones have to be included. The generalization of the Stoner-Wohlfarth model has been developed in three dimensions by Thiaville [16, 17] and applied to an arbitrary effective anisotropy.

Reversal models

The magnetization reversal processes in small nanostructures are traditionally analyzed in terms of analytical models. These analytical models are often based on the approximations, such as demagnetizing factors. In spite of the fact that the demagnetizing factor approximations are valid for ellipsoidal nanoparticles only, they allow a simple analytical description of nucleation fields. Additionally, the analytical models have allowed the classification of different magnetization reversal modes and the cross-over between them.

In single-domain particles, the reversal process is not necessarily uniform and cannot be always described by the Stoner-Wohlfarth model [10]. Other reversal modes such as curling or buckling may occur and ease the reversal process. These two non-uniform modes lead to lower coercive fields than in the Stoner-Wohlfarth model. In these modes, the angle between the individual magnetic moments and the cylinder axis varies from a magnetic moment to another (see Figure 1.11). They are observed in structures exhibiting a radius larger than the coherence radius R_{coh}.

In the case of spheres, the value of R_{coh} is [18]

$$R_{coh} = \sqrt{24} l_{ex} , \qquad (1.24)$$

The exchange length l_{ex} is the minimal length which is required so that the direction of the magnetic moments can change [18]. The exchange length is typically of order of few nanometers.

$$l_{ex} = \sqrt{\frac{A}{\mu_0 M_S^2}} \qquad (1.25)$$

In the case of cylinder, the value of R_{coh} is [19]

$$R_{coh} = 3.65\, l_{ex} , \qquad (1.26)$$

In the case of long cylinders, when the applied field is parallel to the nanowire axis, two main magnetization rotation modes have been considered: i) Homogeneous or in-unison coherent rotation, and ii) Magnetization curling. Shape and magnetocrystalline anisotropies and exchange energy terms compete to determine the most energetically favorable mode. An alternative way to obtain information about the actual rotational magnetization reversal mechanism is the study of the angular dependence of magnetic properties, particularly of coercivity and remanence M_r.

The classical angular dependence of the nucleation field for a coherent magnetization reversal was calculated by Stoner-Wohlfarth [10, 20], a general expression for the field making a angle α with the long axis $H_C(\alpha)$, of a reversed domain can be established as

$$H_C(\alpha) = \frac{2(K_{MC}+K_{sh})\sqrt{1-t^2+t^4}}{\mu_0 M_s^2(1+t^2)} M_s \qquad (1.27)$$

where $t = tan^{1/3}(\alpha)$

For a very long wire, coherent rotation in the whole wire may become unlike and rather a kind of domain wall extending a given length may form with transverse magnetization and propagate along the wire so, reducing the coercivity. Landeros *et al*. [21] calculated the total energy for the transverse reversal mode considering the sum of exchange and dipolar contributions. Then, they minimized the energy with regard to the domain wall width (ω_T). The calculation of nucleation or coercive field was derived by Escrig *et al*. [22] assuming that the magnetization reversal by means of the nucleation and propagation of a transverse wall is equal to the nucleation field of an equivalent system with an effective volume that reverses its magnetization by coherent rotation. Then, the Stoner-Wohlfarth model can be adapted to describe the angular dependence of a transverse reversal mode by replacing the length of the whole structure by the reduced length of the involved domain wall with width ω_T.

In a curling process, the exchange energy is increased but the magnetostatic energy is reduced as less magnetic moments point out of the easy axis at any step of the reversal process [23]. The coercive field thus becomes:

$$H_C(\theta) = \frac{2K_{MC}}{\mu_0 M_s^2} + \frac{c(D)A}{\mu_0 M_s R^2} \qquad (1.28)$$

where A is the exchange stiffness and $R = R_x = R_y$ refers to the two degenerate axes of the ellipsoid. $c(D)$ is a parameter which depends on the value of D and thus on the shape of the particle. For instance, $c = 8.666$ for spheres ($D = 1/3$) and $c = 6.678$ for needles ($D = 0$).

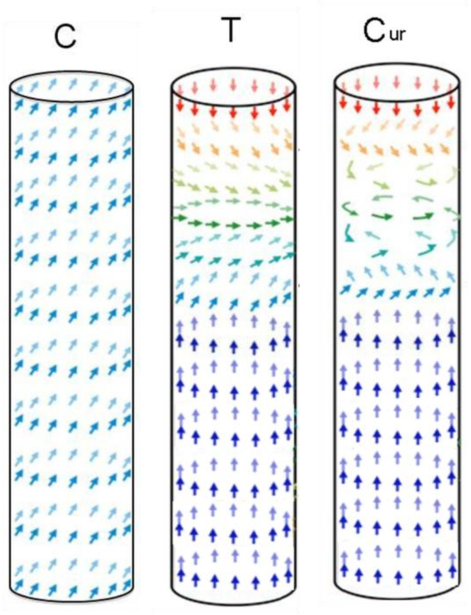

Figure 1.11 Magnetization reversal modes in nanowires. The arrows represent the orientation of magnetic moments within the wire. Left: coherent rotation mode, C. Center: transverse rotation mode T, Right: curling rotation mode, Cur [22].

1.9 Exchange Bias

Exchange bias (EB) is the shift of the hysteresis loop with respect to the zero magnetic field axis. Meiklejohn and Bean discovered it in 1956 at low temperatures when the CoO/Co system is cooled under an external magnetic field [30]. In their words EB is “A new type of magnetic anisotropy has been discovered which is best described as an exchange anisotropy. This anisotropy is the result of an interaction between an antiferromagnetic material and a ferromagnetic material" [24, 25]. Since its discovery various antiferromagnets (AFM), which are exchange coupled to ferromagnets (FM), have shown H_{EB}. There are well written reviews on the subject listing possible configurations which contains ferromagnetic/antiferromagnetic interfaces such as small particles, inhomogeneous materials and thin films [26-30]. Yet, there is no general theory applicable to all systems. Possible applications of the exchange biasing effect can be found mostly in magnetic read heads in connection with spin valves and in permanent magnet applications [26].

Simple exchange bias mechanism of an FM/AFM interface is illustrated in Figure 1.12 When materials with FM/AFM interfaces are cooled through a temperature which is larger than the Neel temperature (T_N) of AFM and smaller than the Curie temperature (T_C) of FM, an anisotropy (exchange bias) is induced in FM. When $T < T_N < T_C$ the spins of FM and AFM are ordered and coupled ferromagnetically at the interface in the 1st quadrant of Figure 1.12. When we trace the hysteresis loop starting from the 1st quadrant, the magnetization of FM resists turning to the negative field in the 2nd quadrant. At a particular negative magnetic field, Zeeman energy of FM overcomes the ferromagnetic coupling at the interface. Therefore, the magnetization of FM aligns with negative magnetic field and the FM/AFM interface becomes antiferromagnetic in the 3rd quadrant. When we retrace the hysteresis loop from 3rd quadrant back to the 1st quadrant, magnetization returns back to the original ferromagnetic alignment at the interface. However, the hysteresis loop is shifted to the left by an amount known as $H_{EB.}$

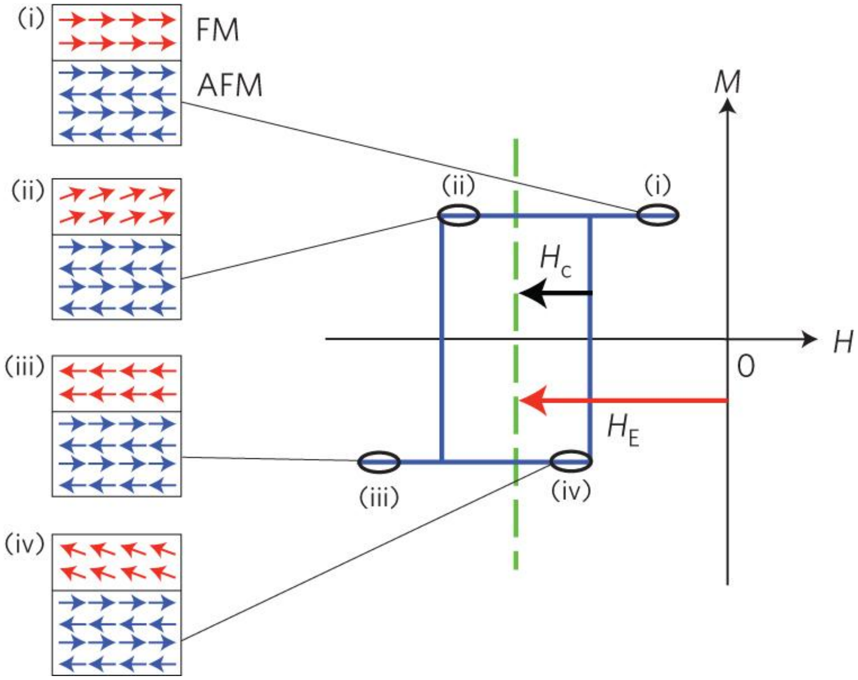

Figure 1.12 Exchange biasing of an FM/AFM interface [26].

Generally, a negative H_{EB} is observed for FM/AFM structures with respect to the positive cooling field. The fundamental effect of the exchange bias is the enhancement of the coercivity. The enhanced coercivity of small particles (nanostructures) may have potential applications in permanent magnet applications.

Industrial applications of H_{EB} are based on the thin film structure [26]. Spin valve structure in Figure 1.13 based on the giant magnetoresistance effect (GMR) [31-34] can be used as a read head, magnetic sensor or a magnetoresistive memory. GMR is the resistance between two ferromagnet separated by a nonmagnetic spacer. If one of the F's is exchange biased to an AFM then the hysteresis loop will be composed of two inner hysteresis loops. Shifted loop corresponds to the exchange biased FM/AFM layer and the other symmetric hysteresis loop corresponds to the free F's which is separated by a nonmagnetic spacer. There is a field range where the ferromagnetic layers have antiparallel magnetizations. Therefore resistance is low when the magnetizations of two F's are parallel and high when the magnetizations are antiparallel. Hence high to low resistance changes at lower field ranges makes this device attractive for applications. Since there is not a general theory for the exchange biases all first principle calculations are remained as models. Although the models help to understand the effect each has its own advantages and drawbacks.

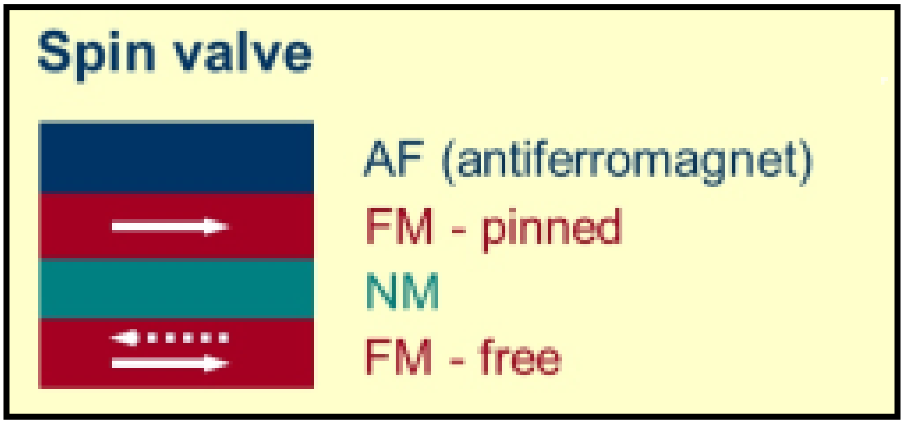

Figure 1.13 Structure of Spin valve device.

The earliest and simple model [26] is based on an ideal interface like in Figure 1.12. The ferromagnetic and antiferromagnetic layers are both single crystalline and epitaxial across atomically smooth FM/AFM interface. The AFM interface is fully uncompensated. Magnetization reversal for the ferromagnetic layer is coherent while the spins of the antiferromagnetic layer remains fixed. Therefore Hamiltonian (H) per unit interface area can simply be written as:

$$H = -HM_{FM}t_{FM} \cos\theta - J_{FM/AFM}\cos\theta + t_{FM}K_{FM}\, sin^2\theta \qquad (1.29)$$

Here, H is the magnetic field, M_{FM} is the ferromagnetic layer magnetization, t_{FM} is the thickness of the ferromagnetic layer, θ is the angle between magnetic field and M_{FM}, J_{FM}/A_{FM} is the exchange coupling coefficient and K_{FM}: is the anisotropy constant of the ferromagnetic layer. Minimization of the above Hamiltonian with respect to θ gives the exchange field as:

$$H_{EB} = \frac{J_{FM/AFM}}{M_{FM}t_{FM}} \qquad (1.30)$$

Here, exchange field is directly proportional to the coupling coefficient and inversely proportional to the magnetization and the thickness of the ferromagnetic layer.

Other origins like non-colinearity of the spins of the antiferromagnetic and ferromagnetic layers [35], grain size distribution [36] or even random anisotropy of the AFM layer [29] have also been proposed. Unfortunately, although these models suit well to a specific system, they do not account for the others.

In conclusion, exchange bias depends strongly to the interface spin structure. Spin orientation, anisotropy, crystallinity, roughness, defects etc. contribute to the exchange bias. Hence many factors effecting exchange anisotropy makes the theoretical analysis complicated.

1.10 Soft Magnets

Magnetic materials are broadly classified into two main groups: soft and hard depending on their hysteresis characteristics. Hard magnets, also referred to as permanent magnets, are magnetic materials that can retain their magnetism after being magnetized. Soft magnetic materials can be easily magnetized and demagnetized by low-strength magnetic field. When an applied field is removed, soft magnetic materials will return to a state of relatively low residual magnetization. Soft magnetic materials are used primarily to enhance or channel the flux produced by an electric current. The main parameter, which is often used as a figure of merit for soft magnetic materials, is the relative permeability, which is a measure of how readily the material responds to the applied magnetic field. The other main parameters of interest are the coercivity, the saturation magnetization, and the electrical conductivity. As shown in Figure 1.14, typical soft materials have an intrinsic coercivity of less than 100 Oe and high saturation magnetization M_S but low M_r.

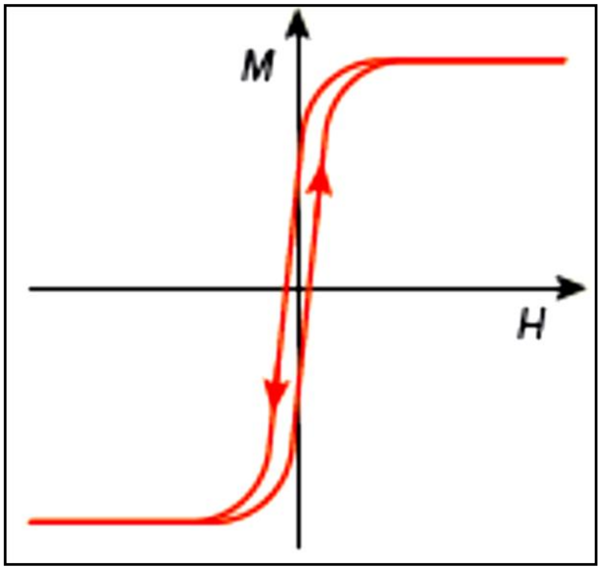

Figure 1.14 The magnetization curve and hysteresis loop of a soft magnet.

1.11 Permanent Magnets

For permanent magnet applications the spin phenomenon called ferromagnetism is the most important, since ferromagnetism is what gives the material its magnetic properties to function as a permanent magnet. In a ferromagnetic material all the spins of the electrons are oriented in the same direction, as seen in Figure 1.15 in the low temperature range. It is in this ferromagnetic region that the material has a magnetic moment. When the temperatures increases the magnetic moment decreases, which is due to a transition from a ferromagnetic state to a paramagnetic state. In the paramagnetic region all electron spins are oriented randomly in the crystal and that leads to no, or small, magnetic moment. The temperature where the shift from the ferromagnetic state and the paramagnetic state occur is called Curie temperature, T_C, named after Pierre Curie who was the first to discover this phenomenon [6].

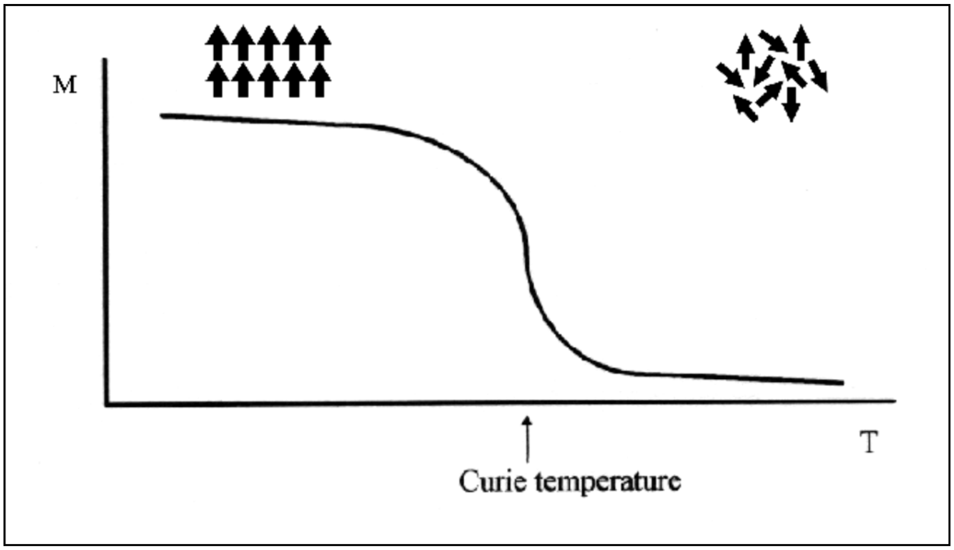

Figure 1.15 Magnetization as function of temperature for the Curie transition of a ferromagnetic material. Also the different spin ordering is displayed for the ferromagnetic region (below T_C) and the paramagnetic region (above T_C).

Besides from having a Curie temperature over the working temperature of the magnet there are some other properties that are important for a good permanent magnet. Many of them can be found in a M(H) curve (or B(H) curve since ($B = H + 4\pi M$), which is a plot of the magnetization in the material as a function of the applied magnetic field. An illustrative plot can be found in Figure 1.15. As can be seen in Figure 1.16 starting at the origin, the first point of interest is the saturation magnetization, M_S, where maximum magnetization is reached for the material. When removing the magnetic field the magnetization decreases. At the point where the magnetic field is zero the magnetization has reached remanent magnetization, M_r. Remanent magnetization is ability for the substance to retain magnetization. If a negative magnetic field is then applied the point where the magnetization is zero will be reached. That point is called coercivity, H_C, and is the magnetic field required to “coerce” the material back to zero induction.

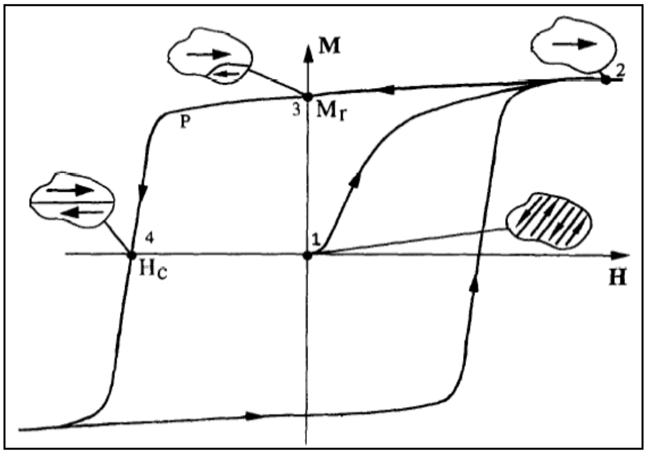

Figure 1.16 The magnetization curve and hysteresis loop of a permanent magnet showing the magnetic domain structure in the virgin state (1), at saturation (2), at remanence (3), and at the coercive field (4) [7].

At a point between M_r and H_C a key aspect for permanent magnets is found. That is $(BH)_{max}$, found in Figure 1.16 as working point, and is called the energy product. The energy product is a quantity of the stored energy in the magnetic field created in the magnet.

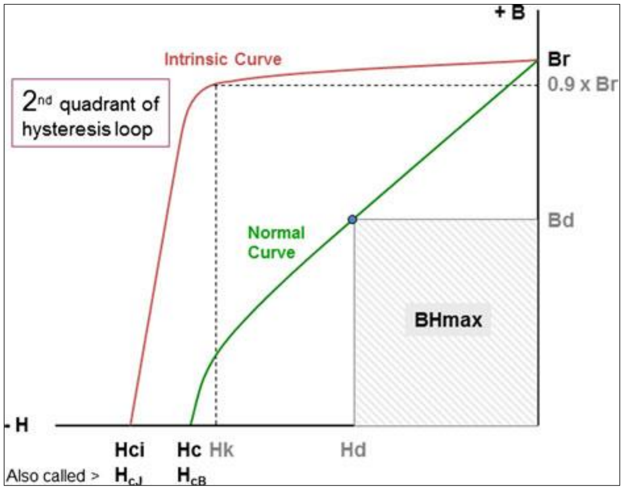

Figure 1.17 Typical M-H and B-H loops of ferromagnetic materials [37].

$(BH)_{max}$ is used as a figure of merit for permanent magnet materials. Its unit is KJ/m^3 (MGOe). For a permanent magnetic material, the $(BH)_{max}$ is twice the maximum magnetostatic energy available from a magnet of optimal shape. The product tends to increase with both increasing coercive field H_c and saturation magnetization M_S. However, for materials with sufficiently high H_C values ($H_C > 2\pi M_S$), the theoretical limit for the energy product is limited only by M_S and is given by: [38]

$$(BH)max \leq (2\pi Ms) \qquad (1.31)$$

The highest value of $(BH)_{max}$ of a material requires an ideal rectangular hysteresis loop. Several different types of permanent magnetic materials are now available including a variety of alloys, intermetallics, and ceramics. The most widely studied permanent magnetic materials are: Cobalt-rare earth alloys ($SmCo_5$, or Sm_2Co_{17}), neodymium-iron-boron ($Nd_2Fe_{14}B$), iron-platinum (FePt), cobalt-platinum (CoPt), hard ferrites ($SrO\text{-}Fe_2O_3$ or $BaO\text{-}6Fe_2O_3$), and Alnicos. To develop a new generation of novel materials for high-performance permanent magnets with the energy products $60\ kJ/m^3 < (BH)_{max} < 160\ kJ/m^3$, which do not contain any rare earths or platinum is important from both scientific and economic point of view.

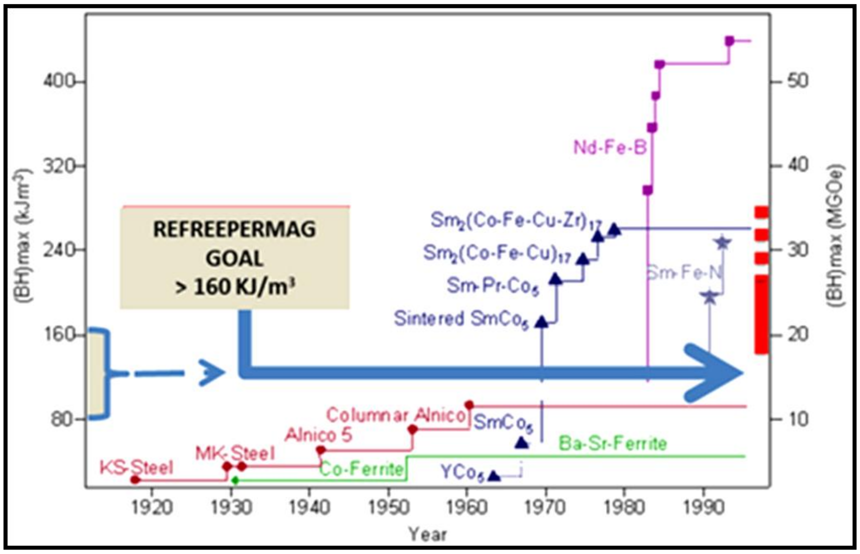

Figure 1.18 Progress in the energy product of permanent magnets [39, 40].

Chapter 2

Synthesis of Magnetic Nanostructures

Nanowires are considered as nanoparticles with diameter smaller than the length and ranges between 1-100 nm in diameter and 100 nm to tens of microns in its length. The fabrication of nanowires can be achieved from a wide range of materials which includes inorganic, electrical conductors, organic, insulators, and semiconductors [41, 9]. Like other types of inorganic materials, magnetic nanowires should be produced with controlled properties based on manipulation of processing parameters. Also, control of the processing conditions is needed to manipulate the structural characteristics of the particles allowing control of the intrinsic magnetic properties.

One of the most recent challenges has been to control the shape of the nanostructures and to synthesize anisotropic objects such as nanowires instead of isotropic objects like nanoparticles. Various fabrication and assembly techniques have been developed for generating controllable and scalable arrays of 1D nano-material. There are two basic paradigms for the fabrication of materials in the nanoscale: top-down and bottom-up approaches. The top-down approach commonly refers to the selective sculpting, or etching, of a bulk material for cutting structures down to the nanoscale regime. Conventional well-established techniques under this approach are optical and electron-beam lithography [42, 43] are currently employed to grow magnetic nanowires, which are usually expensive, does not permit any large scale fabrication and time-consuming.

2.1 Chemical Synthesis Methods

The bottom-up approach, on the other hand, aims to create structures by piecing them up together from atomic- and molecular-scale components. The bottom-up approach appears to be the most promising alternative to synthesize nanowires exhibiting a diameter of a few nanometers. Most of the top-down fabricated structures can be produced via bottom-up molecular manufacturing by synthesis of atomically precise products with lower cost and in larger quantities.

Common bottom-up techniques are the vapor-liquid-solid [44], template-assisted electrochemical deposition [45, 46] and solution-based growth approaches [47, 48].

2.1.1 Vapor-Liquid-Solid Method

The Vapor-Liquid-Solid (VLS) technique allows growing nanowires from a metal melted drop. Recently, some of successfully fabricated semiconductor nanowires are base on the vapor-liquid-solid (VLS) method. The growth of nanocrystals which directly adsorb a gas phase on to a solid surface is generally very slow. The mechanism of VLS is using catalyst such like liquid alloy phase which can rapidly adsorb a vapor to supersaturation levels, and the nucleation generates a solid precipitate of the source material. These seeds become the preferred site for material deposition at the interface of the liquid droplet. The seeds will elongate into nanowires or whiskers. The deposit which anisotropy is like a whisker whose diameter is controlled by the diameter of the liquid alloy droplet.

2.1.2 Electrochemical Deposition Method

The electrochemical deposition technique has widely studied for fabricating nanowires. It does not require a special environment (vacuum, high pressure or high temperature). The equipment and chemicals are relatively inexpensive depending on the materials that are being deposited in the pores of the template. Traditionally, this method is used to grow thin film on conducting surface. Since electrochemical growth is usually controlled in the direction normal to substrate surface, this method is really can be applied on fabricating 1D or 0D nanostructures. This method has been widely applied to synthesize metals and semiconductors nanowires.

2.1.3 Solution Phase Synthesis Method

The importance of solution based method synthesis for anisotropic nanocrystals results from many unique features. Control of nucleation and growth, restricting the size to the nanometer regime [49]. Use of a suitable surfactant, surfactant mixture, or capping molecules that selectively adsorb on specific planes of growing particles and induces symmetry-breaking steps [50, 51]. Surfactants can stabilize the interfaces of nanoparticles and prevent oxidation and aggregation processes [52]. Following are the selected solution base synthesis method used in this dissertation.

2.1.3.1 Polyol Synthesis

The polyol method, in which a polyol (Figure 2.11) acts as solvent, reducing agent, and surfactant, is a suitable method for preparing nanoscale size particles with well-defined shapes and controlled particle sizes [53-55]. Polyols are interesting solvents because they have relatively high permittivity, making them ideal for dissolving ionic and even inorganic solids [56]. Nanocrystalline powders of different metals such as Fe, Co, Ni, and their alloys (CoNi), (FeCo) and (FeNi) were synthesized using different salt precursors by this method [57-59].

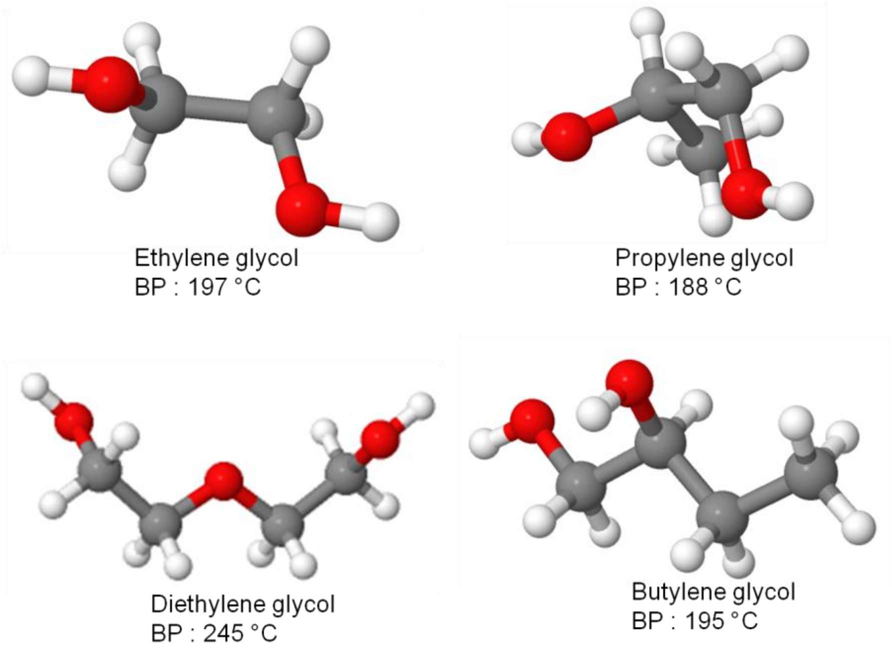
Ethylene glycol
BP : 197 °C
Propylene glycol
BP : 188 °C
Diethylene glycol
BP : 245 °C
Butylene glycol
BP : 195 °C

Figure 2.1 Different polyols used for the reduction of metal precursors.

Polyols, like alcohols, are mild reducing agents therefore the reactions can occur between room temperature and the boiling point of the solvent (up to 450 °C for light polyethylene glycols). Fievet et al. [60] have reported fabricating isolated metallic nanoparticles of different metals via polyol reduction, in ethylene glycol as media. However, they reported that in absence of additional stabilizers to control the growth of the nanoparticles, the particles were highly agglomerated and the particle size distribution was broad with irregular shapes. The polyol method was modified later by different noble strategies to overcome this deficiency; for example, by varying the temperature of the reaction or using a precursor that is partially soluble, which gives rise to an insoluble solid phase that acts as a kind of reservoir. Alternately, kinetically controlled reactions by using heterogeneous nucleation seeds to slow the nucleation step can also be employed for better dispersed metal nanoparticles [61]. Also, employing long-chain polyols that can act as protective agents (surfactants) or the use of additional protective agents (e.g., PVP) allows controlling the particle growth, which is crucial in case of magnetic metals that have higher tendency to agglomerate.

2.1.3.2 Hydrothermal Synthesis

Hydrothermal processing can be defined as any heterogeneous reaction in the presence of aqueous solvents or mineralizers under high pressure and temperature conditions to dissolve and recrystallize (recover) materials that are relatively insoluble under ordinary conditions. The hydrothermal method has become more popular for the synthesis of nanostructures of several metal oxides like titania, zinc oxide and iron oxide in the form of nanowires, nanorods, nanotube and nanoribbons [62]. Hydrothermal methods show advantages over conventional methods like sol-gel and hydrolysis of iron salts. Surfactants like sodium dodecylsulfonate (SDBS) and cetyl-trimethyl ammonium bromide (CTAB) have been used.

2.1.3.3 Solvothermal Synthesis

Solvothermal methodology is extensively employed as a solution route to produce semiconductor nanowires and nanorods. In this process, a solvent is mixed with the metal precursors and crystal growth regulating or templating agents, such as amines. This solution mixture is placed in a Teflon-lined stainless steel autoclave maintained at relatively high temperatures and pressures to carry out the crystal growth and the assembly process. The methodology is quit versatile and has enabled the synthesis of crystalline nanowires of semiconductors and other materials [63].

2.2 Nanowire Nucleation and Growth

There are two important processes in the growth of nanocrystals in solution, the nucleation and the growth of the nanocrystals. The discussion of these two processes is in the following two subsections.

2.2.1 Theory of Nucleation

LaMer et al. had study of extensively nucleation and growth in sulfursols [64, 65] from the research they developed and explained the mechanism for the formation of colloids and nanocrystals from a supersaturated, homogeneous medium. The mechanism is that the colloid synthesis should be designed in such a way that the concentration increases rapidly, then rising above the saturation concentration for a short period, and a burst of nucleation occurs with the formation of lots of nuclei in a short time. These particles grow rapidly and decrease the concentration below the nucleation level which allows the particles to grow at the rate limited by the slowest step in the growth process. By this way, the nucleation and growth of nanoparticles can be separated in time. Figure 2.2 shows the simple diagram of LaMer's mechanism. The high nucleation rate is leading to the burst of nuclei formation in a short time. These nuclei grow in a fast rate and reduce the concentration below the concentration level of rapid nucleation, and the slow growth rate leading to a longer growth period.

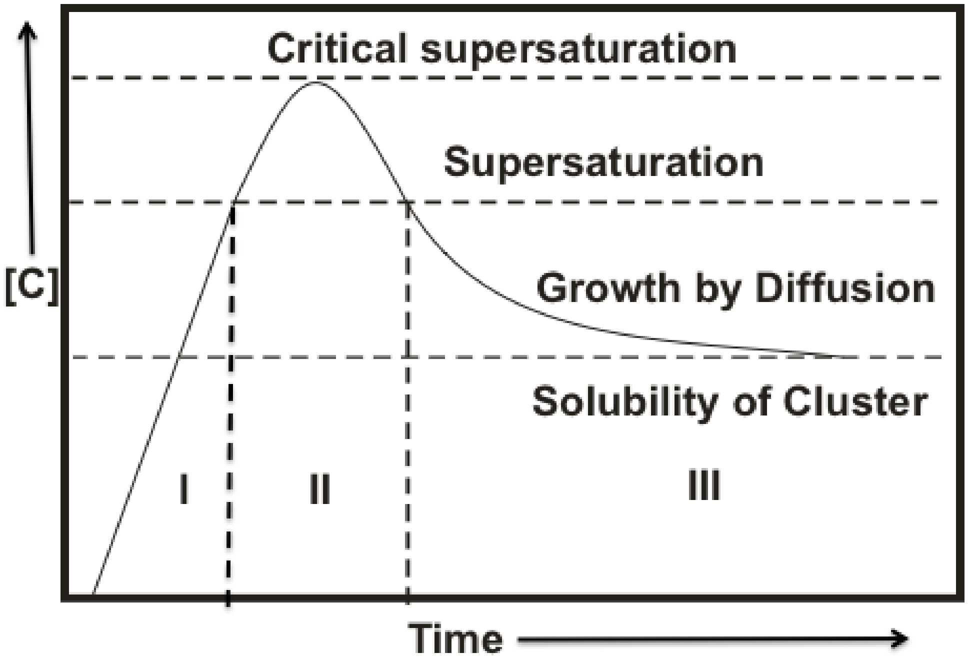

Figure 2.2 LaMer crystallization model.

The model also stated that monodispersity is a consequence of carefully separating the nucleation step from the subsequent growth step (see Figure 2.2). For metal particles, nucleation is the result of a complicated interplay of factors such as the difference between the reduction potentials of the metal salt and the reducing agent and the reaction conditions including the rate of addition, the rate of removal, the reaction temperature, the reaction duration and even the stirring rate. To achieve a monodisperse sample, the nucleation step must be complete before the growth step begins. Recently, the synthesis has been processed by mixing the reactants together, often by injecting one of chemicals into the remaining ones in a short time. This can make sure that the whole nucleation process in that short time, followed by a slower growth process, thereby attempting to separate the two stage temporally.

2.2.2 Mechanism of Growth

Nucleation occurs during some time with constant monomer concentration. The growth of particles surface start to occur which decrease the monomers supply. Nucleation ends when the concentration of monomer falls below the critical level for nucleation. Generally speaking, the surface to volume ratio in small particles is pretty high, the surface excess energy becomes very important in very small particles. For a solution which isn't in thermodynamic equilibrium, the formation of larger particles reduces the surface energy of the initial smaller particles, and this mechanism play an important role in the growth of nanocrystals. The monomers diffuse to the surface of nanocrystals and make bonding with surface atoms, and this process lets small particles become larger. Coarsening effects which controlled by mass transport or diffusion are often termed the Ostwald ripening process, and this diffusion limited Ostwald ripening process is the most important growth mechanism and was first quantified by Lifshitz and Slyozov [66], and the following related work was done by Wagner [67], known as the LSW theory.

The diffusion process is controlled by the surface energy of nanoparticles. The energy which associated with the difference between the chemical potential of atoms in an interfacial area and atoms in nearby bulk phase is called interfacial energy. In solid/liquid interface, with the chemical potential of particles increasing, the particles size decrease. The concentration of small particles in equilibrium solution is much higher than large particles, as described by the Gibbs-Thompson equation. The transportation of solution from small particles to large particles is led by concentration gradients. Depending on the local curvature of solid phase, the different curvatures of equilibrium concentration of nanocrystals in the liquid phase set up concentration gradients and provide a driving force to grow the larger particles at the expense of smaller particles [68].

2.2.3 Self-Assembly Growth of Nanowires from Solution

It is still complicated to form nanowires from solution method. The growth of nanowires generally includes three steps: (1) crystalline seed formation; (2) crystal growth by aggregation of monomers to seeds; and (3) surface stabilization by surfactants. So far, Scientists proposed several mechanisms for the anisotropy growth of nanocrystals in solution [69]. The following are three typical mechanisms.

2.2.3.1 Solution-Liquid-Solid (SLS) Growth from Seeds

During the SLS reaction, the molecular precursor is decomposed at high temperature and generates monomers. In this kind of reaction, the metal catalysts are very small and easy to be activated at low temperature. The monomers react with the metal nanoseeds to form supersaturated alloy droplets (Figure 2.3). For example, Semiconductor nanowires such like Si and Ge [70, 71] grown from Au nanocatalyst under the supercritical fluid environment have been made. The ultra-thin nanowire [70] with 2-3 nm diameters have been fabricated by this method and the interesting optical properties have been observed.

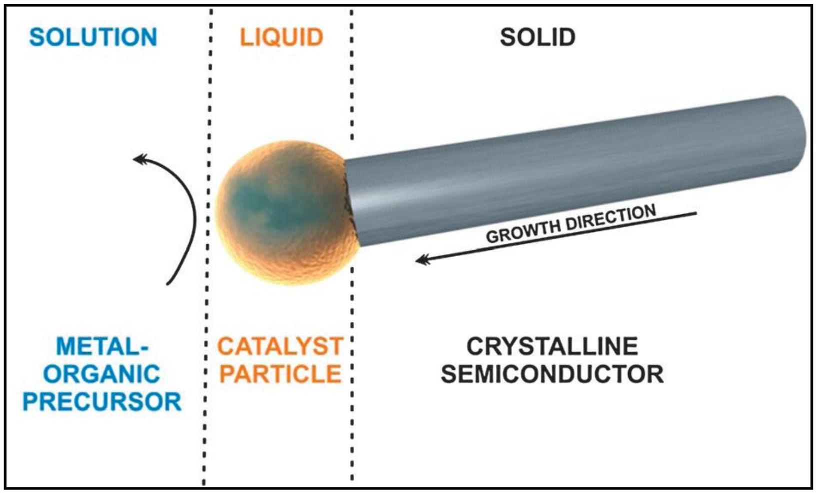

Figure 2.3 Schematics exemplifying the Solution-Liquid-Solid (SLS) growth for the generation of nanowires in solution [72].

2.2.3.2 Self-Assembly Oriented Attachment Growth

The self-assembly attachment growth is based on the fact that nanoparticles generated in solution have a large surface-to-volume ratio. In order to reduce the surface energy and the total system energy, the nanoparticles may segregate together, and oriented attachment is one of the ways for this process. Penn and Banfield [73] observed this nanowires formation mechanism in the hydrolytic synthesis of TiO_2 nanocrystals. The oriented attachment refers to the direct self organization of two particles into a single crystal caused by sharing a common crystallographic orientation. A large single crystal can form through consecutive attachment of the small nanocrystals, which is different from the simple physical assembly of nanomaterials. Because the oriented attachment involves the assembly of nanocrystal building blocks, tailoring the way of attachment generates 1-D or 2-D structures with tunable properties.TiO_2 nanoparticles mainly included three face, {001}, {121} and {101}. The {001} has the highest energy and it is reasonable to remove this face since this is thermodynamic favorable. By this oriented attachment process, the nanoparticles are congregated along the [001] direction to remove the {001} face (Figure 2.4).

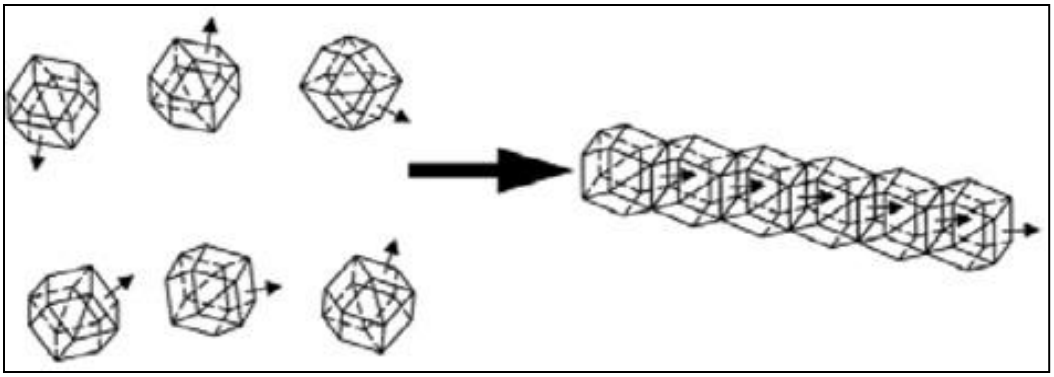

Figure 2.4 The Oriented attachment growth.

2.2.3.3 Anisotropic Growth of Crystals by Kinetic Control

Anisotropy growth caused by different surface energies is the mechanism for forming most elongated nanocrystals, but the difference of surface energies is not large enough to form highly anisotropy growth of nanowires. It is believed that the effective surface energy of nanocrystals can be modulated by adding surfactants to the reaction solution, and the surfactant molecules selectively absorb and bond on certain surfaces of the nanocrystal seeds. For example, the [001] is the first growth direction of TiO_2 nanocrystal in solution. By adding surfactants into reaction, the first growth direction can be changed to [101]. The role of surfactants is “structural directors”. This selective capping effect decreases the growth of these surfaces and increases the growth of nanocrystals in specific direction to form nanowires (Figure 2.5).

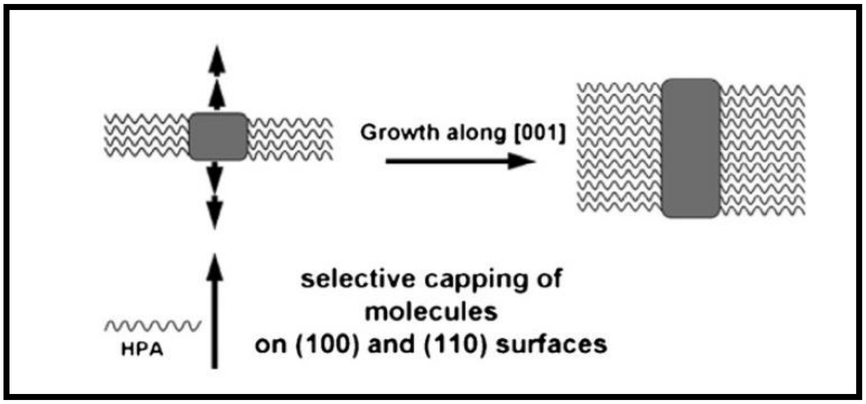

Figure 2.5 Surface selective surfactant assistant growth.

The present study deals with the synthesis and investigation of the structural and magnetic properties of nanostructures of Fe, Co, FeCo, CoNi and $CoFe_2O_4$. Bottom up approach using chemical solution phase method has been used for synthesis. It seems an elegant approach and stands out as an alternative to other sophisticated techniques such as template, lithography etc. since it offers a high degree of control in size, shape, crystal structure and high yield. The size and shape of the nanostructures were found to be dependent on experimental parameters such as the catalyst concentration, the surfactant ratio, the precursor concentration and the heating rate. It was observed that the uniformity in morphology, structure and composition of the nanowires was the key to achieving a high coercivity and saturation magnetization.

In this context, we have investigated the magnetic properties of FeCo, CoNi nanowires and nanorods synthesized using polyol process in flask; $CoFe_2O_4$, α-FeOOH nanowires and nanorods synthesized using hydrothermal process and Co and CoNi nanowires by solvothermal process.

Chapter 3

Characterization Techniques

In this chapter we present a summary of the characterization techniques that have been used throughout this PhD work. Transmission electron microscopy (TEM), high resolution TEM (HRTEM), scanning electron microscopy (SEM), and powder and X-ray diffraction (XRD) were used for structural characterization. Inductively coupled plasma-optical emission spectroscopy (ICP-OES) and energy dispersive X-ray (EDX) were used for compositional characterization of nanoparticles before and after annealing. An Alternating gradient magnetometer (AGM) and a superconducting quantum interference device (SQUID) magnetometer were used for magnetic characterization. A brief description of these equipments and characterization techniques and the techniques used to prepare samples are following.

3.1 Structural Characterization by X-ray Diffraction (XRD)

Powder X-ray diffraction (XRD) spectra were recorded on a Rigaku Ultima IV diffractometer with a Cu K-α wavelength X-ray source for crystalline structure characterization of samples. The samples were prepared by drop casting dispersions of nanowires in toluene on a glass substrate. The samples were dried under ambient conditions.

The X-ray diffraction (XRD) allows one the identification and structural characterization of crystalline nanostructures. The X-rays interact with the electrons in the atoms, when passes through the sample, resulting in scattering of the radiation. The wavelength of the X-ray radiation has values of 1 Å in the order of the lattice parameters in crystalline solids. Thus, if the distance between the atoms is close to the wavelength of the X-rays, interference of the scattered waves in these solids will occur and form a diffraction pattern with constructive and destructive interferences. The X-rays are scattered at characteristic angles based on the spaces between the atomic planes defining their crystalline structure. Since most crystals have several sets of planes passing through their atoms, each of them has a specific interplanar distance and will originate a characteristic angle of diffracted X-rays. The intensity maximum of the diffraction pattern will appear for scattering directions which are univocally related with specific reciprocal lattice vectors of the solid. These directions determine the so called Bragg reflections (giving Bragg peaks in the spectra) and a set of Miller indexes (hkl) can be assigned to them. The relationship between wavelength (λ) atomic spacing (d_{hkl}) and diffraction angle θ, is given by the Bragg's law:

$$n\,\lambda = 2d_{hkl}\,sin\,\theta, \qquad (3.1)$$

where λ is the wavelength of the incident wave, d_{hkl} is the distance between the planes with the miller indexes (hkl), and the angle θ formed by the propagating vectors of the incident and scattered waves. From the broadening it is possible to determine an average crystallite size, in Å, by Debye-Scherrer formula:

$$d_{hkl} = k\,\frac{\lambda}{\beta\,cos\,\theta}, \qquad (3.2)$$

where k = 0.8-1.39 (usually close to the unity e.g. 0.9, considering spherical grains), the wavelength λ of the radiation λ_{Cu} = 1.54056 Å, β is the full width at half maximum, or half-width in radians and θ is the position of the maximum of diffraction.

3.2 Morphological Characterization

3.2.1 Transmission Electron Microscopy (TEM)/High-resolution (HRTEM)

TEM and high-resolution transmission electron microscopy (HRTEM) are powerful imaging tools for studying nanowires at the atomic scale, and they usually provide more detailed geometrical features. TEM studies also yield information regarding the crystal structure, crystal quality, grain size, and crystal orientation of the nanowire axis. When operating in the diffraction mode, selected area electron diffraction (SAED) patterns can be made to determine the crystal structures of nanowires. A JEOL 1200 EX transmission electron microscope (TEM) operated at 120 kV was used to record low magnification bright field and dark field images and selected area electron diffraction patterns (SAED). The HRTEM work was carried out in a Hitachi H-9500 electron microscope operated at 300 kV with a point resolution of 1.8 Å. A 300-mesh copper grid with a carbon film deposited on a formvar backing, purchased from Ted Pella, were used for preparing TEM samples and with a lacey carbon film were used for preparing HRTEM samples. A drop of the nanowires dispersion solution in toluene was put on the formvar side of the TEM grid.

The solvent was allowed to evaporate in air and assemble on the grid. The dark field images can be obtained using a center dark-field method under a nearly two-beam condition. The plan-view TEM samples providing most of the detail information of nanowires morphology and microstructure and surface structures of the nanowires were investigated in HRTEM.

Several imaging analysis softwares were applied to process and analyze TEM and HRTEM images. Gatan's Digital Micrograph software installed with Hitachi H-9500 HRTEM was used for initial measurement and quantitative analysis of as-taken images, such as d-spacing and Fast Fourier Transformation (FFT) of lattices fringes.

Features observed by TEM may then be immediately analyzed to obtain the corresponding elemental composition, using the Energy Dispersive Spectroscopy (EDS) analysis of X-rays. EDS measures the energy and intensity distribution of x-rays generated by the impact of the electron beam on the surface of the sample.

3.2.2 Scanning Electron Microscopy (SEM)

The morphology of the aligned nanowires was studied by scanning electron microscopy (SEM). SEM yields images with a resolution from a few millimeters down to 5 nm. In a SEM microscope, the surface of the sample is irradiated with high energy electrons. A set of magnetic lenses moves the focused beam back and forth across the specimen. As the electron beam hits each spot on the sample, both electrons and photons are emitted by the specimen surface, and their intensity is used to form the SEM image when all the spots are convoluted. The signals most commonly used are the secondary electrons, the backscattered electrons and X-rays. Secondary electrons are specimen electrons that obtain energy from inelastic collisions caused by the incident beam electrons. They are defined as electrons emitted from the specimen with energy less than 50 eV. A Hitachi S-4800 II FE SEM operated at acceleration voltage of 0.5 - 30 kV was used to record images.

3.3 Spectroscopy Characterization

3.3.1 Raman Spectroscopy

The Raman spectra were recorded in a ThermoFisher Scientific DXR Raman microscope equipped with a DXR 532 nm excitation laser and high resolution grating for 532 nm laser. Samples were prepared by depositing the nanoparticles dispersion on (1x1) inch glass substrates and drying the organic solvent in air. Raman spectroscopy, a molecular spectroscopy which is observed as inelastically scattered light, allows for the interrogation and identification of vibrational (phonon) states of molecules. As a result, Raman spectroscopy provides an invaluable analytical tool for molecular finger printing as well as monitoring changes in molecular bond structure (e.g. state changes and stresses & strains).

3.3.2 ICP-MS Spectroscopy

Inductively Coupled Plasma Mass Spectrometry or ICP-MS is an analytical technique used for elemental determinations. PerkinElmer/SCIEX ELAN DRC II (Sheldon, CT) ICP-MS system was used to characterize the elemental distribution in the metallic nanowires. Samples were prepared by digestion and dilution, desired analyte level in 1% HNO_3.

3.4 Magnetic Characterization

3.4.1 Alternating Gradient Magnetometer (AGM)

In an AGM measurement, the sample is mounted on an extended rod attached to a piezoelectric element and then placed at the center of the poles that generates magnetic field. An alternating gradient magnetic field is generated which produces an alternating force on the sample. This force (*F*) is proportional to the magnitude of the alternating magnetic field (*B*) and the magnetic moment (*m*) of the sample. Thus,

$$E = -m \, . \, B \qquad (3.3)$$

$$F_x = -\frac{dE}{dx} = m\,\frac{dB}{dx} \qquad (3.4)$$

This force is converted into a proportional voltage by a piezoelectric element and hence the moment of the sample can be measured. The applied field is measured by a Hall probe sensor and the sensitivity of the AGM can reach up to 10 nemu. Samples with dimension up to 5 mm x 5 mm can be measured in AGM. The maximum magnetic field that can be applied by AGM is limited to 14 kOe and it can only be operated at room temperature. Therefore, samples that have high anisotropy or require low or high temperature measurements will need magnetometers that can provide much higher saturation field to get accurate magnetic measurements and capability of operating in different temperatures.

Figure 3.1 Princeton Measurements Corporation Alternating Gradient Magnetometer.

3.4.2 Superconducting Quantum Interference Device (SQUID) Magnetometer

SQUID uses a superconducting magnet, through which large amount of current can flow so that large magnetic field can be generated. The magnetic measuring mechanism of SQUID belongs to an inductive technique. During magnetic moment measurement, the sample moves through a system of superconducting detecting coils and the magnetic moment of the sample causes change in magnetic flux associated with the detecting coils, resulting in electric current produced in the detecting coils. The detecting coils are connected to the SQUID sensor, which functions as a highly linear current-to voltage converter, producing very accurate variations in the output voltage that is proportional to the moment of the sample. The SQUID can generate a magnetic field as high as 70 kOe and can be operated in temperatures from 2 K to 400 K. The sensitivity of SQUID is 10 nemu up to applied field of 2.5 kOe and 0.6 μemu above that. Liquid helium is required to operate SQUID, which makes the use of it expensive. Sample dimension requirements of SQUID are almost the same as AGM, but the sample for SQUID can be longer in one of its dimensions. AGM is much easier, faster, and less expensive to operate comparing to SQUID. Hence, room-temperature measurements of all samples that can be saturated below 14 kOe should be measured by AGM.

Figure 3.2 Quantum design SQUID magnetometer.

3.4.3 Vibrating Sample Magnetometer (VSM)

VSM is an integrated magnetometer in a Physical Property Measurement System (PPMS). VSM can generate a magnetic field as high as 140 kOe and can provide magnet moment sensitivity up to 1 μemu. The magnetic measuring mechanism is a VSM, which belongs to an inductive technique similar to the SQUID, except that the motion of a sample in the detecting coils for the VSM is much faster than in the SQUID. The normal operating temperature of VSM is between 1.9 K and 400 K, however, a VSM with an oven option can be operated from room temperature to 1000 K. The measurement of VSM is faster than SQUID but has lower sensitivity. Measurements that require a saturation field higher than 70 kOe and temperatures higher than 400 K are performed by VSM instead of SQUID.

Figure 3.3 Quantum design PPMS with VSM insert (Left) and MicroSense (formerly known as ADE Technologies) Vibrating Sample Magnetometer systems (VSM) (Right).

Angle dependence magnetic properties of Co nanowires aligned sample in epoxy are characterized using MicroSense (ADE Technologies) Vibrating Sample Magnetometer systems (VSM) with an angle measurement option at room temperature. In VSM, a uniform magnetic field generated from electromagnet is applied across an oscillating sample near a set of pick up coils. The flux of uniform field is distorted and induces a potential drop, as followed Faraday’s law of induction, across pick up coils. The potential V is proportional to the magnetic moment from the sample so that the hysteresis loop (m-H curve) can be obtained by varying applied field while measuring the magnetic moment of the sample.

Hysteresis loops were measured at different rotation angle in parallel directions of applied fields, defined as the direction of applied field respectively to c-axis of Co nanowires.

Chapter 4

Magnetic Anisotropy of $CoFe_2O_4$ Nanocrystals

4.1 Introduction

The Permanent magnets are essential components in modern technologies, being employed in a huge number of large-scale and emerging applications, such as electronic devices, hard disks, automotive, wind turbines, and hybrid−electric vehicles. Recently, there is a considerable interest in research for new methods to synthesize non rare earth based hard magnetic materials. Nanoparticle size, shape, crystal structure, and composition are often related to nanoparticles magnetism such as anisotropy, magnetization, coercivity, and ordering temperature [74-79]. Therefore, the development of novel permanent magnets based on nanoparticles, requires a careful control of the particle size, to properly balance the single domain behavior and thermally driven demagnetization effects.

One of the most promising materials to be investigated to this purpose is cobalt-ferrite ($Co_xFe_{3-x}O_4$). $CoFe_2O_4$ has been studied widely due to its interesting magnetic properties such as high coercivity and remanence, moderate saturation magnetization, excellent chemical stability, and good mechanical hardness. All these properties, together with many other outstanding characteristics, such as magnetostriction [80] and large magneto-optical coefficients, [81] make cobalt ferrite extremely appealing for application in several technological fields including exchange-coupled nanocomposite magnets, magnetic data storage, magnetic fluids, and biomedicine [82-86].

Many advances to synthesize highly crystalline, monodisperse cobalt-ferrite nanostructures have been made using a variety of chemical and physical approaches [87-91]. A number of efforts have been made to increase coercivity in cobalt ferrite. The maximum coercivity of 9.3 kOe at room temperature reported to date in thin films deposited on SiO_2 single crystal substrate that was due to the small grain size (50 nm) and lattice strain in the films [92]. The large coercivity of 4.6 kOe was reported in $CoFe_2O_4$ nanoparticles synthesized using seed mediated growth method [93]. High coercivity of 9.4 kOe was reported in oleic acid capped $CoFe_2O_4$

nanoparticles with low magnetization of 7.1 emu/g [94]. Despite the number of reports, to our knowledge, all these studies were limited to small sizes, low magnetization and low yield.

In this chapter, report on the synthesis of single crystalline ferromagnetic $CoFe_2O_4$ nanoparticles and shuttle like nanorods through a one-step hydrothermal method, which was employed along with the surfactants to control morphology, size, and composition of the nanoparticles. This method is suitable for mass production of magnetic CoFe2O4 nanoparticles. The evolution of the magnetic properties was studied as a function of the particles size and shape. We found that at room temperature, the highest $(BH)_{max}$ is observed for nanoparticles with size of ~ 40 nm. The highest $(BH)_{max}$ reported for randomly oriented cobalt-ferrite nanoparticles (2.0 MGOe). Finally, the feasibility of the application of cobalt-ferrites nanoparticles in the realization of a permanent magnet is discussed on the basis of the $(BH)_{max}$ product.

4.2 Experimental

4.2.1 Synthesis of $CoFe_2O_4$ Nanocrystals

The hydrothermal method was used to synthesize cobalt ferrite. This method provides different classes of nanostructured inorganic materials from aqueous solutions, by means of small Teflon lined autoclaves and has a lot of benefits such as: clean product with high degree of crystallinity at a relative low reaction temperature (up to 200 ºC). All reagents are commercial products of analytically pure without further purification. In a typical synthesis, $FeCl_3.6H_2O$ (1.08 g, 4 mmol), $CoCl_2$ (0.26 g, 2 mmol), NaOH (0.8 g, 20 mmol) and cetyltrimethylammonium bromide (CTAB) (1.0 g, 2.75 mmol) were dissolved in 7 ml deionized (DI) water by intensive stirring till a homogeneous solution was obtained. Subsequently, a 14 ml of ethylenediamine (EDA) was added dropwise into the above mentioned aqueous solution. After stirring for 30 min, the slurry mixture obtained was transferred into a Teflon-lined stainless steel autoclave. This autoclave was kept in a furnace and heated to 200 °C at rate of 8 °C per minute. The autoclave then maintained at 200 °C for 10 hr and was reaction then cooled to ambient room temperatures.

The composition of the particles was controlled by changing ratio of initial precursors. To obtain better control in process, we examined several parameters that may have an effect on the size and shape of $CoFe_2O_4$ nanocrystals. We found that surfactants and their concentration, and PH of the system are the key parameters which play a crucial role in size and shape control of the nanoparticles.

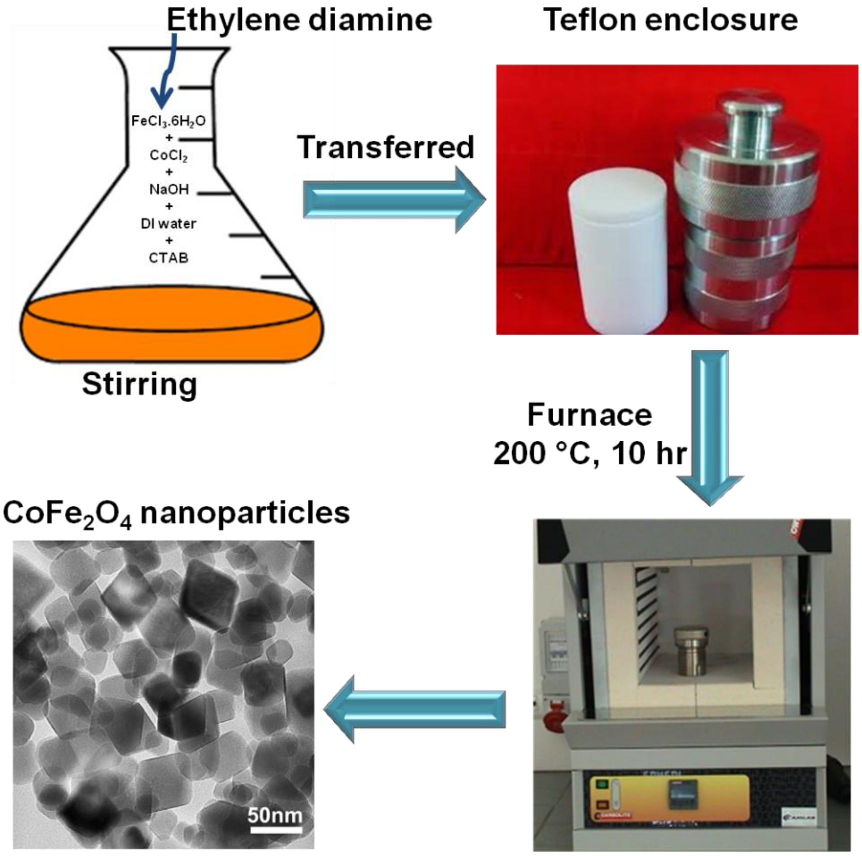

Figure 4.1 Schematic illustration showing synthesis of $CoFe_2O_4$ nanocrystals.

4.2.2 Purification and Characterization of $CoFe_2O_4$ Nanocrystals

After cooling to room temperature, the black powder consisting of cobalt ferrite nanocrystals was separated from reaction fluid by centrifugation at 6000 rpm for 15 min. The powder was collected then redispersed in 30 ml ethanol using an ultrasonic bath. The sample was centrifuged once again at 6000 rpm for 15 min and the ethanol was discarded. This purification step was repeated two more times. After washing the particles in ethanol three times, they were dispersed in ethanol and stored in glass bottles. To prepare TEM/HRTEM samples, a drop of the nanoparticles dispersion solution in ethanol was put on the formvar side of a 300-mesh carbon coated copper TEM grid. Samples for magnetic characterization were prepared by depositing a drop of the final ethanol dispersion on a silicon substrate evaporating the solvent at room temperature and by hardening randomly oriented $CoFe_2O_4$ powders in epoxy.

The transmission electron microscopy (TEM) images were recorded on a JEOL 1200 EX electron microscope at 120 kV accelerating voltage. HRTEM images were obtained with Hitachi H-9500 at 300 kV. Powder X-ray diffraction (XRD) spectra were recorded on a Rigaku Ultima IV diffractometer with a Cu Kα X-ray source. The Raman spectra measurements were carried out using DXR Raman microscope (Thermo Scientific) with a laser (532 nm and 5 mW) excitation source. Magnetic measurements of the metallic samples were performed using a Quantum Design MPMS magnetometer.

4.3 Results and Discussion

4.3.1 Morphology and Structure

$CoFe_2O_4$ nanocrystals with different size and shape were synthesized via the hydrothermal route. Various combinations of NaOH and CTAB were studied at fixed precursor concentration and fixed reaction temperature.

Figure 1 shows the TEM images for the samples prepared using different concentration of NaOH and CTAB by the hydrothermal method. Figure 4.2(a)-(b) show typical $CoFe_2O_4$ nanoparticles synthesized using 12 mmol (S1) and 20 mmol NaOH (S2) without adding surfactant CTAB into the solution mixture. The particles shown in Figure 4.2(a) have different shapes with a broad particle size distribution. Figure 4.2(b) shows a narrow size distribution of the nanoparticles with diameters of 20-40 nm.

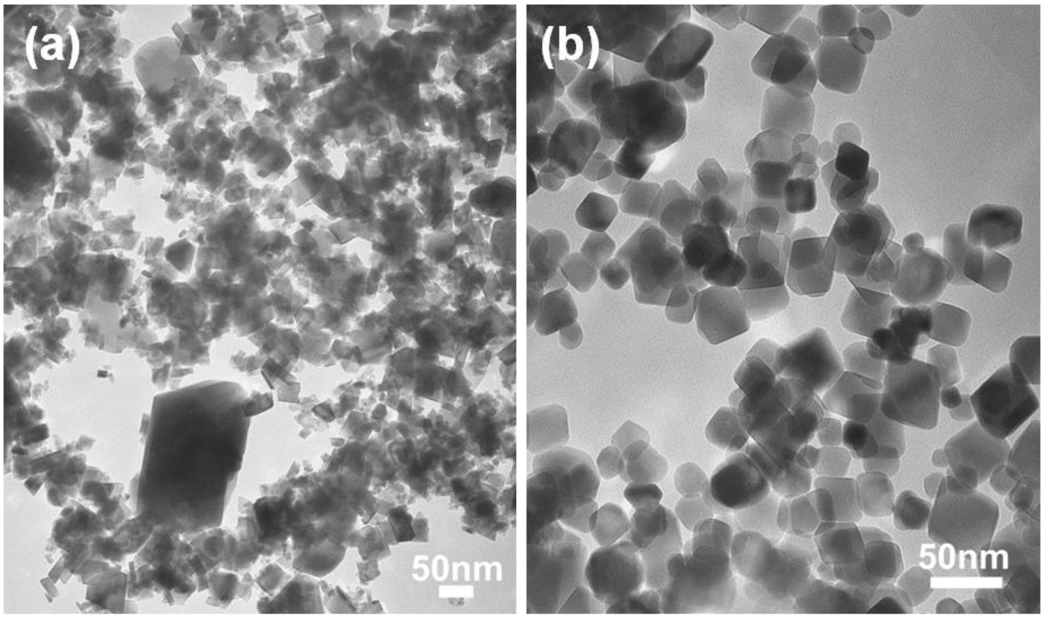

Figure 4.2 TEM images of the $CoFe_2O_4$ nanocrystals synthesized using different concentration of NaOH without adding surfactant CTAB (a) 12 mmol NaOH, (b) 20 mmol NaOH.

Surfactants typically play a crucial role in controlling the size and shape of synthesized nanoparticles. We first studied the effect of surfactant addition on size and shape of the nanocrystals. Figure 4.3(a) shows the typical TEM image of ~ 40 nm $CoFe_2O_4$ nanoparticles prepared with 2.75 mmol of CTAB and 20 mmol of NaOH (S3) while other reaction parameters are kept unchanged. When the concentration of surfactant CTAB was increased to 5.5 mmol (S4) while other reaction parameters are kept unchanged, we observed a mixture of nanoparticles with diameter 10-30 nm and shuttle like nanorods with diameter of 40-50 nm and length of 60-100 nm as shown in Figure 4.3(b). The surfactant CTAB is cationic and is responsible for the rod shape assembly of nanoparticles. Upon the ionization, CTAB constitutes the CTA^+ ion that forms the pair with negatively charged Fe–OH–Co, thus constituting the crystal growth initializers [95].

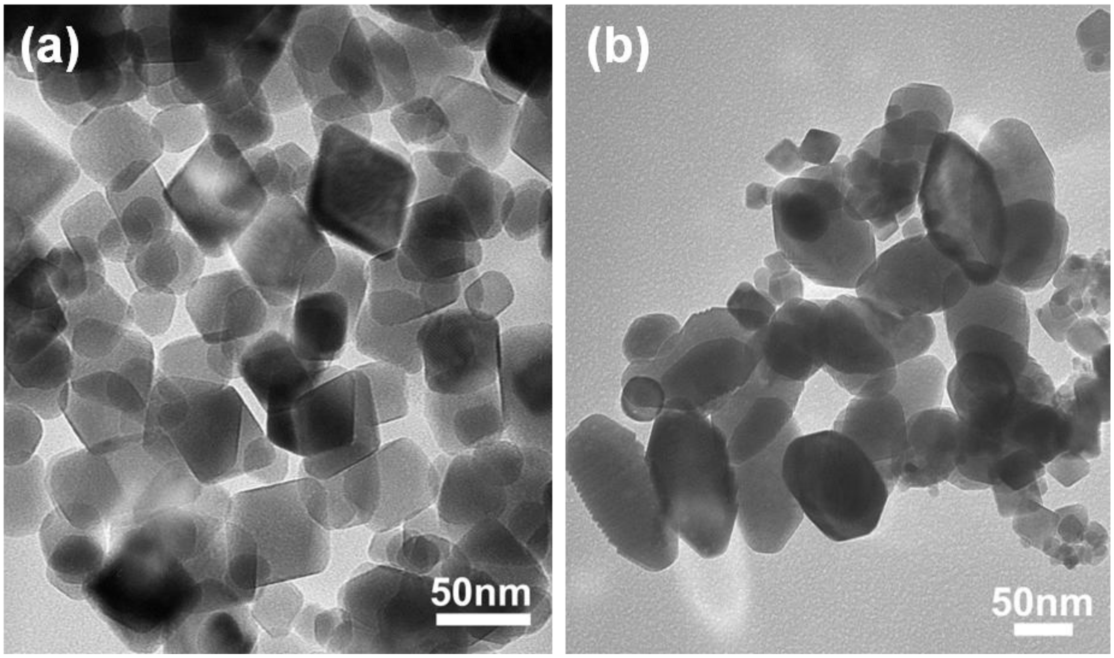

Figure 4.3 TEM images of the $CoFe_2O_4$ nanocrystals synthesized using different concentration of CTAB with 20 mmol NaOH (a) 2.75 mmol CTAB, (b) 5.5 mmol CTAB.

The HRTEM and electron diffraction pattern of the as-synthesized $CoFe_2O_4$ nanocrystals reveals good crystallinity and clear lattice fringes, as shown in Figure 4.4 and 4.5, respectively. Figure 4.4(a)-(b) shows the HRTEM image of representative ~ 40 nm $CoFe_2O_4$ nanoparticles and shuttle like nanorods with diameter of 40-50 nm of sample S3 and S4. The nanoparticle is single crystalline and has a lattice fringes of 0.48 nm spacing of the (111) planes in inverse spinel structured face centered cubic (fcc) $CoFe_2O_4$. Theoretically, cubic spinel structures should generate a cubic crystal habit, reflecting the growth along the preferential ⟨100⟩ axes, but our experimental result suggests that with our synthetic procedure, octahedral shapes are the most favored, depending on the size.

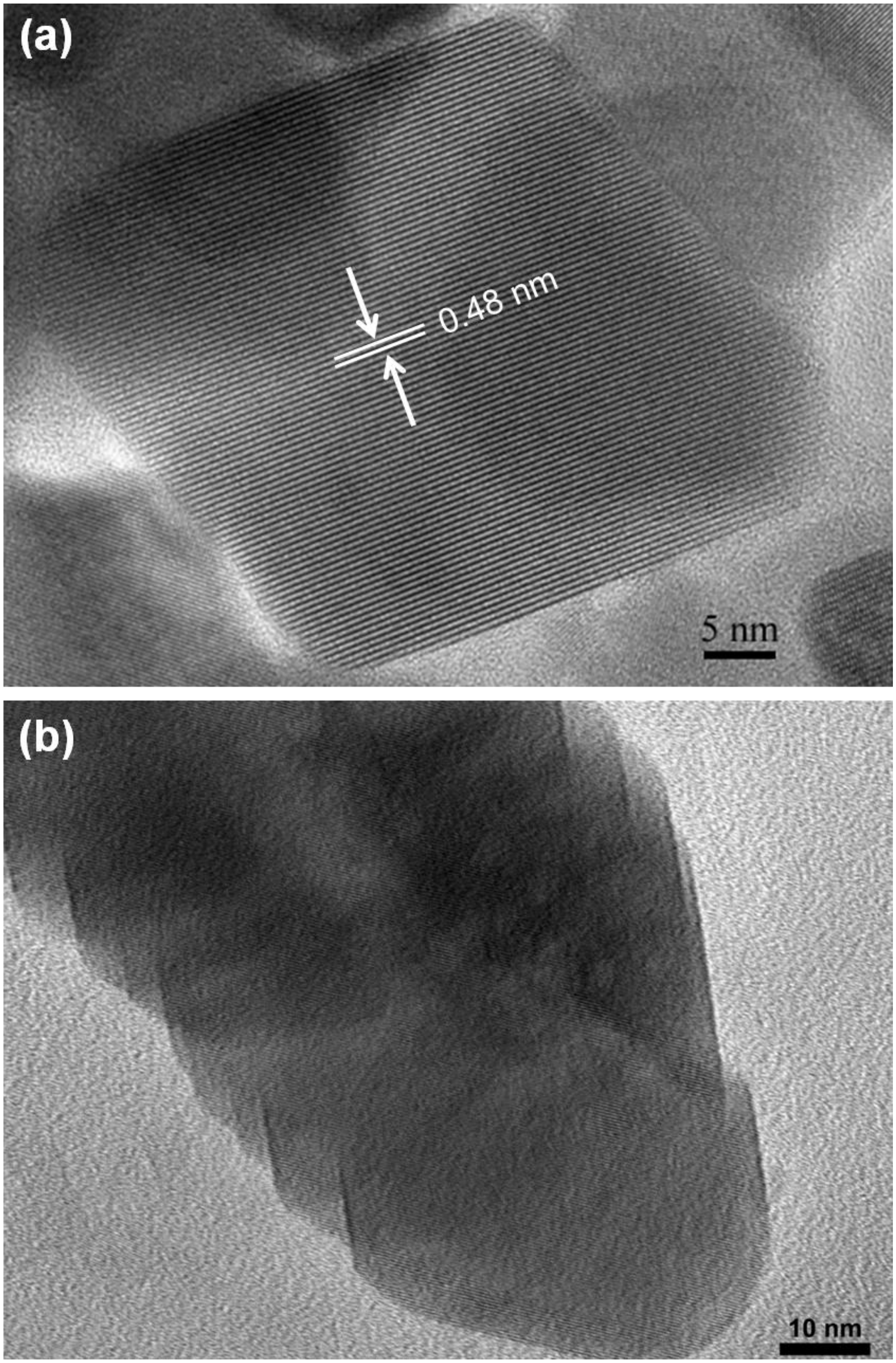

Figure 4.4 HRTEM images of $CoFe_2O_4$ (a) nanoparticle and (b) shuttle like nanorod.

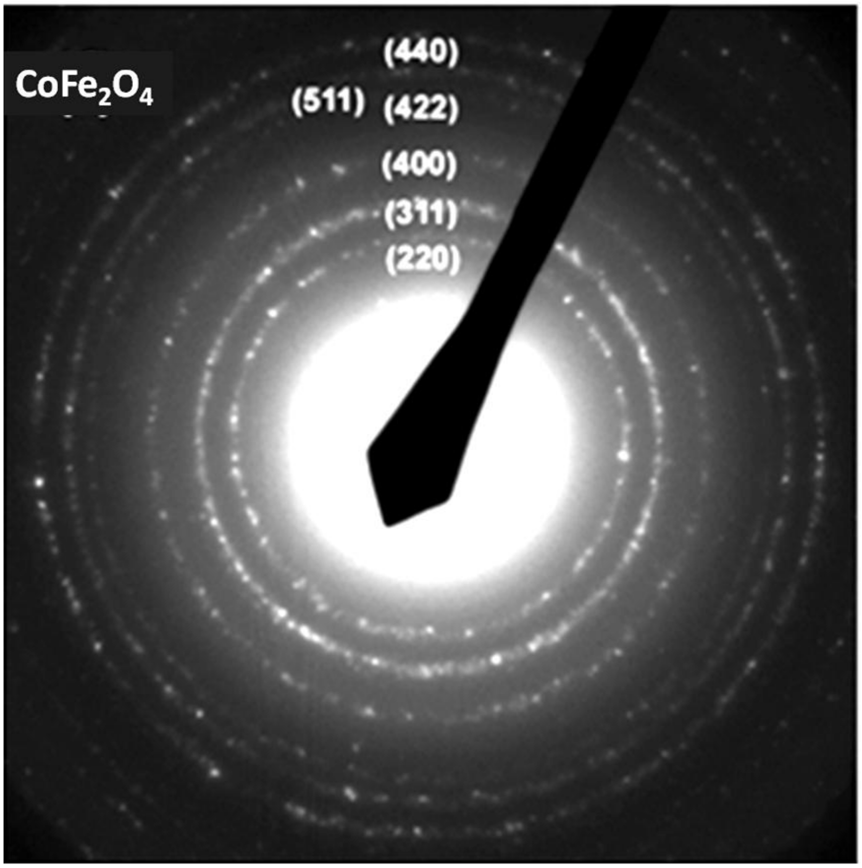

Figure 4.5 Electron diffraction pattern of the $CoFe_2O_4$ nanoparticles

The crystal structure of nanoparticles was further characterized using XRD. Figure 4.6 shows the XRD patterns of the CoFe2O4 nanocrystals prepared by varying the concentration of NaOH and CTAB. It shows the characteristic (220), (311), (222), (400), (422), (511), (440) and (533) diffraction peaks of $CoFe_2O_4$ phase with fcc crystal structure (Figure 4.6(a)-(c)). The average crystallite size of $CoFe_2O_4$ nanoparticles was estimated from x-ray diffraction patterns using Scherrer formula ($d=0.9\ \lambda/\beta\ \cos\theta_B$). The average crystallite size values determined from XRD patterns for the samples shown in Figure 4.6(a-c) were ~ 28 nm, ~ 38 nm, ~ 42 nm respectively, which are in good agreement with the particles size observed by TEM. Figure 4.4(a) that further confirm $CoFe_2O_4$ nanoparticles are single crystalline.

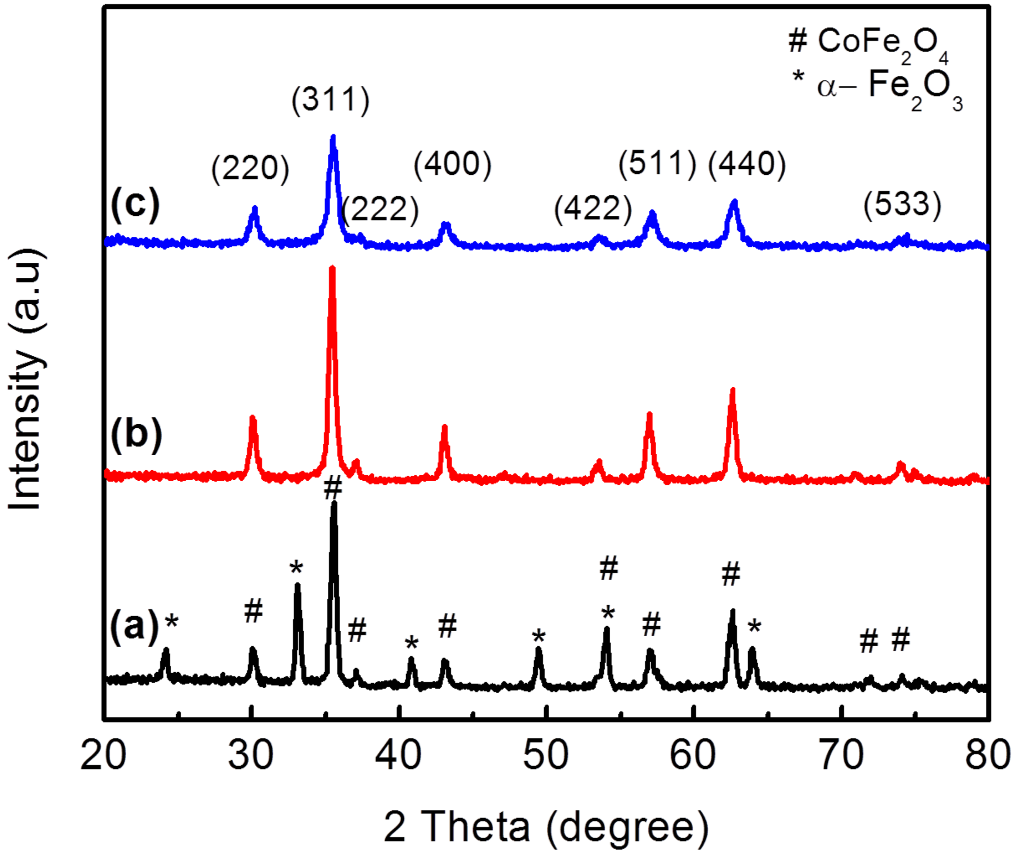

Figure 4.6 XRD of $CoFe_2O_4$ nanocrystals synthesized using different concentration of (a) 12 mmol NaOH, (b) 20 mmol NaOH, 2.75 mmol CTAB, and (c) 20 mmol NaOH, 5.5mmol CTAB.

We observed the presence of α-Fe_2O_3 phase along with $CoFe_2O_4$ phase (Figure 4.6(a)) in the XRD pattern when 12 mmol of NaOH (S1) was used in the reaction. When NaOH amount was increased to 20 mmol the final product obtained was pure $CoFe_2O_4$ phase without the α-Fe_2O_3 impurity as seen in Figure 4.6(b)-(c).

The information on the coordination of the metal ions in the nanocrystals was obtained from the Raman spectroscopy. $CoFe_2O_4$ also has the inverse spinel structure like Fe_3O_4 with cubic $O_h^7(Fd\bar{3}m)$ symmetry [96-98]. According to previous studies the low-frequency vibrations (below 600 cm^{-1}) are attributed to the motion of oxygen around the octahedral lattice site whereas the higher frequencies are attributed to oxygen around tetrahedral sites [99]. In this work, the intense band in the Raman spectra of the two samples at 682 cm^{-1} is characteristic of the tetrahedral site and the band at 470 cm^{-1} is due to Co^{2+} at octahedral sites (Figure 4.7).

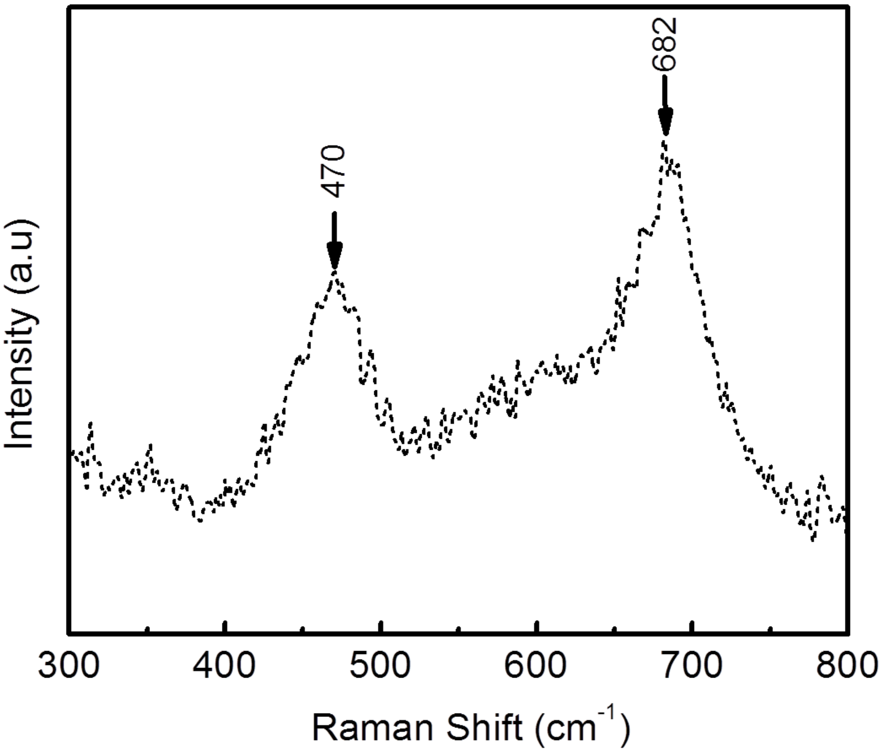

Figure 4.7 Raman spectra of $CoFe_2O_4$ nanoparticles synthesized using 20 mmol NaOH and 2.75 mmol CTAB.

4.3.2 Magnetic Properties

In order to evaluate the magnetic performance of the as prepared $CoFe_2O_4$ nanocrystals, a deep analysis of their static magnetic properties was performed by standard magnetometric technique. Figure 4.8(a) shows the hysteresis loops of $CoFe_2O_4$ nanoparticles (S3) measured as a function of temperature, using an applied field of 50 kOe. The maximum coercivity of 5.0 kOe and a saturation magnetization of 73 emu/g were obtained at 300 K for the 40 nm particles (S3). At 5 K, the coercivity of 17.7 kOe and saturation magnetization of 79.7 emu/g were obtained which can be attributed to the increase in magnetocrystalline anisotropy at low temperatures. The value of squareness ratio (Mar/M_S) of 0.66 indicates that the system consists of randomly oriented equiaxial particles with cubic magnetocrystalline anisotropy. Figure 4.8(b) shows the variation of coercivity and magnetization as a function of temperature. Both the coercivity and the magnetization for the 40 nm particle size (S3) decreases with temperature.

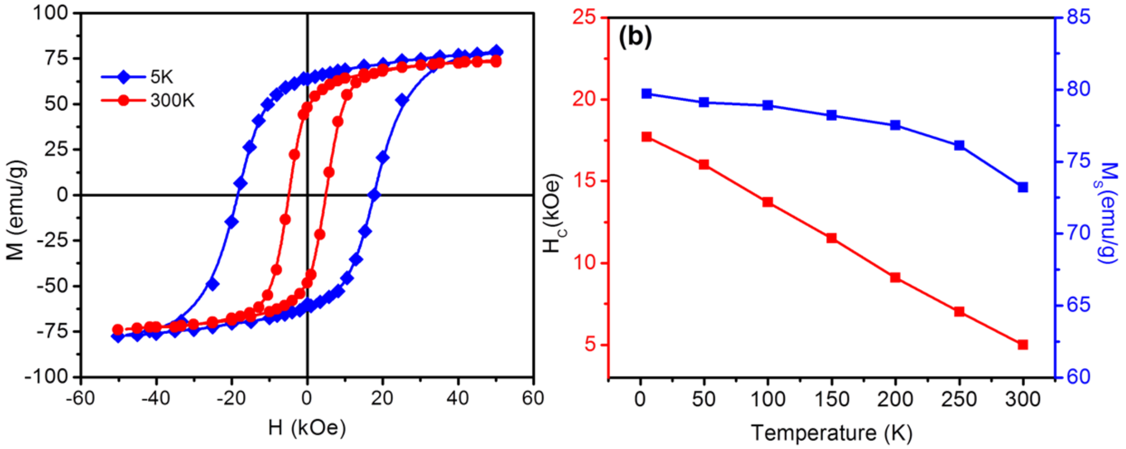

Figure 4.8 (a) Hysteresis loops of 40 nm $CoFe_2O_4$ nanoparticles (S3) measured at 5 K- 300 K, and (b) dependence of H_C and M_S on temperature.

The magnetic parameters obtained from hysteresis loops, such as saturation magnetization (M_S), coercivity (H_C) for all four samples are shown in Table 4-1. The presence of Co^{2+} ions on the octahedral sites of the spinel structure is the primary reason for the strong anisotropy of cobalt ferrite [100]. Furthermore the larger anisotropy in nanosized materials compared to bulk materials is expected due to the additional contributions from surface anisotropy and size-related effects [101]. It has been reported that the critical size of single-domain $CoFe_2O_4$ particles is about 40 nm from both the high switching field obtained by the magnetic torque analysis and the relatively high coercive field obtained for $CoFe_2O_4$ particles [93]. It is therefore expected that $CoFe_2O_4$ particles about 40 nm can have high coercivity. The method of synthesis applied in the present work favors good crystallinity and magnetic ordering resulting in a high saturation magnetization.

Table 4-1 Magnetic properties of $CoFe_2O_4$ nanocrystals

Sample	H_C (kOe) (at 300K)	M_S (emu/g)
S1	2.8	43.8
S 2	4.2	72.4
S3	5.0	73.0
S4	4.2	70.1

In order to quantify the performance as permanent magnets of the family of $CoFe_2O_4$ nanoparticles, we evaluated the maximum energy product, $(BH)_{max}$, at low and room temperature. $(BH)_{max}$, where B and H are the magnetic induction and the applied field, respectively, is the figure of merit of permanent magnets and is defined as twice the maximum magnetostatic energy available from a magnet of optimal shape. Figure 4.9 and 4.10 shows the $B=\mu_o(H + M)$ versus H curve for sample S3 measured at 300 K and 5 K. An important parameter for hard magnetic materials is the $(BH)_{max}$ value, which is the largest area of the rectangle that can fit in the demagnetizing B versus H curve at the second quadrant, Figure 4.9(b) - 4.10(b). The maximum values we found were 4.4 and 2.0 MGOe at 5 K and 300 K, respectively.

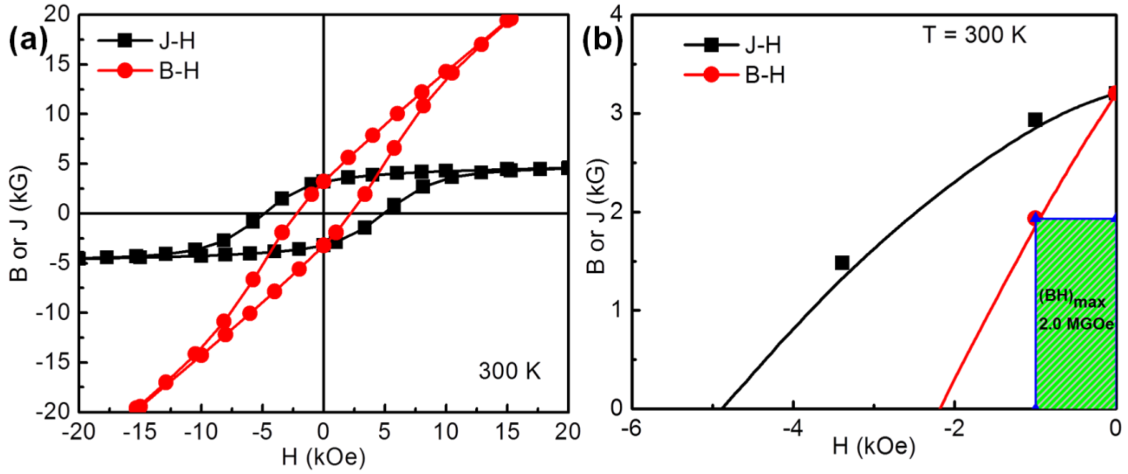

Figure 4.9 (a) B and J vs H loops for sample S3 at 300 K and (b) $(BH)_{max}$ at 300 K.

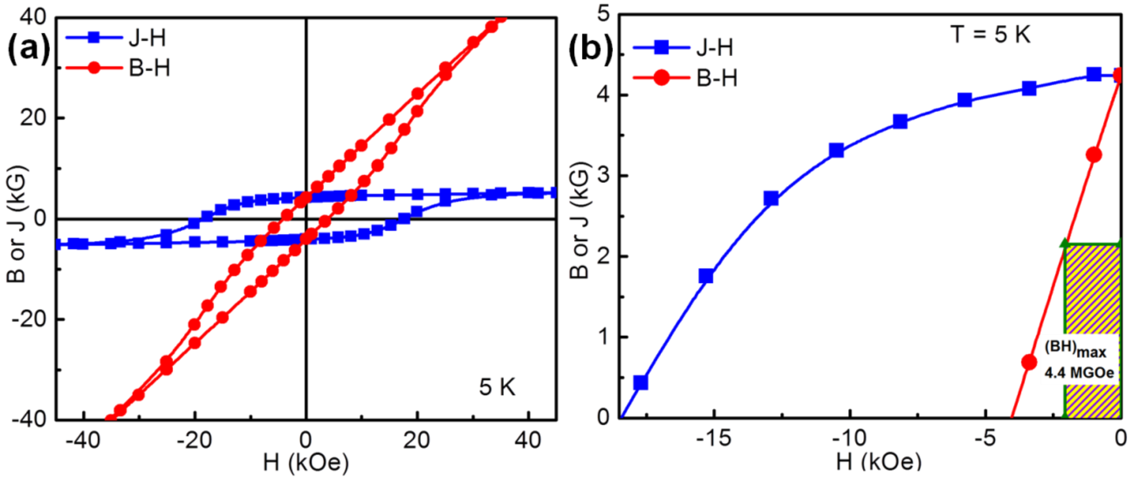

Figure 4.10 (a) B and J vs H loops for sample S3 at 5 K and (b) $(BH)_{max}$ at 5 K.

4.4 Conclusion

In summary, single crystalline $CoFe_2O_4$ nanoparticles were prepared using a simple hydrothermal method. The size and shape of the $CoFe_2O_4$ nanocrystals were found to be dependent on the reaction conditions such as NaOH concentration and CTAB surfactant concentration. A maximum saturation magnetization of 73 emu/g and coercive force of 5.0 kOe were obtained at 300 K which is the highest reported via one step hydrothermal method to our best knowledge. An in-depth evaluation of the influence of the bases on the morphology, structure, chemical composition, and magnetic properties of the nanocrystals is provided. This work sheds new light on the design of magnetic nanoparticles with improved properties through the hydrothermal method. In order to assess the suitability of our $CoFe_2O_4$ nanoparticles as permanent magnet, the $(BH)_{max}$ energy product was evaluated. Interestingly, we found the maximum value for $CoFe_2O_4$ nanoparticles at room temperature (i.e., 2.0 MGOe for 40 nm nanoparticles). Moreover, this investigation allowed us to establish, at least on the basis of $(BH)_{max}$, the potentiality of cobalt-ferrite nanoparticles for the realization of RE free permanent magnet. The obtained results also suggest the possibility to optimize magnetic property of $CoFe_2O_4$ nanoparticles with controlled magnetic alignment for magnetic energy, exchange-coupled system and data storage applications.

Chapter 5

Mesoporous Iron and Iron Based Oxides Nanostructures

5.1 Introduction

Iron oxides, being the oldest known magnetic materials in history, are by far the most studied ones, both in bulk systems and in their nanoscale counterparts. Iron oxide can grow in different structures, depending on formation conditions. Hence, clearly different magnetic features can be observed depending on their chemical nature and crystal ordering. Synthesis of Fe-based low-dimensional nanomaterials is gaining increasing interest from a broad range of scientific disciplines and has found many potential applications. Hematite (α-Fe_2O_3), the most stable iron oxide under ambient conditions, is commonly used in catalysts [102], gas-sensors [103] and electrode materials [104]. Magnetite (Fe_3O_4), owing to its high saturation magnetization is used for biomedical applications including MRI contrast agents and magnetic guided drug delivery [105, 106]. High magnetization and tunable coercivity of Fe-based nanocrystals make them desirable for potential applications in high-density data storage and other magnetic device applications [107-109].

A well-known characteristic of the iron/iron–oxide system is the variety of possible interconversions among the different phases. The presence of three different nanocrystalline phases, i.e., iron, magnetite and hematite exhibits complex shape and structure dependent properties as they undergo structural and magnetic transitions with temperatures. In particular, porous Fe based nanomaterials may exhibit unique physical and magnetic properties attributed to pores and surface conditions. Collectively, these issues make the study particularly challenging, both from a fundamental physics and experimental point of view and have fueled constant interest over the past decades. Much effort has been expended in the preparation of 1D nanowires to precisely control the nanostructures with uniform shape, size and stability. The current methods involve the use of template assisted electrodeposition [110-112], metal evaporation [113], organometallic chemistry [47], electrospinning technique [114], and nanolithography [115]. These methods differ in the degree of complexity, production, cost, purity of the materials and environmental hazard. Nevertheless, it still remains a top challenge to develop a simple approach to synthesize mesoporous 1-D nanostructures of Fe based nanomaterials, particularly α- Fe with controllable morphology.

In this chapter, a novel method to prepare porous iron and iron oxides nanowires/nanorods with well-controlled morphology and composition without using a template or surfactant has been reported. The synthesis consists of producing α-FeOOH nanowires by a hydrothermal method using $FeCl_3$ salt. The iron hydroxide nanowires were then converted into the mesoporous iron oxides nanowire arrays and eventually to mesoporous α-Fe nanorods in the presence of forming gas using a fluidized bed reactor. Changes in the material phase, composition, shape and porosity of these nanowires is controlled by process parameters such as reaction time and temperature. To the best of our knowledge this is the first report to synthesize α-Fe nanorods using fluid bed process without template. The as-prepared Fe based mesoporous nanowires/nanorods exhibited high specific surface area. The effect of shape anisotropy was observed with the alignment of nanowires/nanorods in magnetic field.

5.2 Experimental

5.2.1 Synthesis of α-FeOOH Nanowires

α-FeOOH nanowires were synthesized by a simple hydrothermal method. In a typical experiment 0.6876 g of $FeCl_3.6H_2O$ was dissolved in 30 ml of DI water using a magnetic stirrer. Then, 0.8 g of NaOH was dissolved in 10 ml DI water and added dropwise into the above ferric chloride solution followed by further stirring for 30 min. The reaction solution was transferred to a Teflon-lined 60 mL stainless autoclave and then kept at 160 °C for 12 h. After cooling down naturally, the obtained yellow precipitates were harvested via centrifugation, washed with ethanol several times and then dried overnight.

Fluidization can be obtained using liquid, gas, or a liquid-gas combination, as the fluid passes through the solid material. A typical packed bed is a cylindrical column that is filled with a suitable packing material such as bead. The fluidized bed reactor long tube was placed vertically into electrical resistance furnace capable of attaining 1000 °C (Figure 5.1). For annealing process, 250 mg of as-prepared α-FeOOH nanowires dried powder sample was charged into the reactor from the top (outlet), which sits on a porous gas distributor plate. A reducing forming gas was admitted at a constant flow rate from the bottom (inlet), and flows upward, and the temperature of the furnace was varied in the range 200 °C - 450 °C. After the experiment, the powder was collected from the tube.

Formation of α-Fe_2O_3 nanowires

In order to get α-Fe_2O_3 nanowires, the as-prepared α-FeOOH nanowires were annealed at 200 °C for 3 h in fluidized bed reactor in Ar+H_2 atmosphere. After annealing, α-FeOOH nanowires changed from yellow to red, indicating phase transformation of α-FeOOH to α-Fe_2O_3.

Formation of Fe_3O_4 nanowires

In order to get Fe3O4 nanowires, the as-prepared α-FeOOH nanowires were annealed at 300 °C for 3 h in fluidized bed reactor in Ar+H_2 atmosphere. After annealing, α-FeOOH nanowires changed from yellow to black, indicating phase transformation of α-FeOOH to Fe_3O_4.

Formation of Fe nanorods

In order to get Fe nanowires, the as-prepared α-FeOOH nanowires were annealed at 450 °C for 30 min in fluidized bed reactor in Ar+H_2 atmosphere. After annealing, α-FeOOH nanowires changed from yellow to black, indicating phase transformation of α-FeOOH to Fe.

5.2.2 Characterization of Nanowires/Nanorods

After cooling to room temperature, the annealed red and black powder consisting of α-Fe_2O_3, Fe_3O_4 and Fe was collected then redispersed in 30 ml ethanol using an ultrasonic bath. To prepare TEM/HRTEM samples, a drop of the nanowires/nanorods dispersion solution in ethanol was put on the formvar side of a 300-mesh carbon coated copper TEM grid. The transmission electron microscopy (TEM) images were recorded on a JEOL 1200 EX electron microscope operated at 120 kV. High resolution TEM (HRTEM) images were obtained with Hitachi H-9500 operated at 300 kV. HRSEM was performed using a Hitachi S-5000H instrument equipped with a cold field emission cathode. Powder X-ray diffraction (XRD) spectra were recorded on a Rigaku Ultima IV diffractometer with a Cu Kα X-ray source. Nitrogen adsorption-desorption was determined at 77 K by Brunauer-Emmett-Teller (BET) tests using TriStar II 3020 Surface Area and Porosity System (micrometric instruments) surface area and pore analyzers. The magnetic hysteresis measurements have been carried out using an Alternating Gradient Magnetometer (AGM) with magnetic field of 14 kOe. Randomly oriented nanowire samples for magnetic characterization were prepared by depositing a drop of the ethanol dispersion on a silicon substrate evaporating the solvent at room temperature and then curing in a rapid-set epoxy resin. Aligned nanowires samples were prepared by sonicating the ethanol dispersion for 5 min then adding the epoxy into the dispersion and again sonicating for 2 min. This composite was then poured into a mold and allowed to cure under the external magnetic field of 2.0 T in an electromagnet.

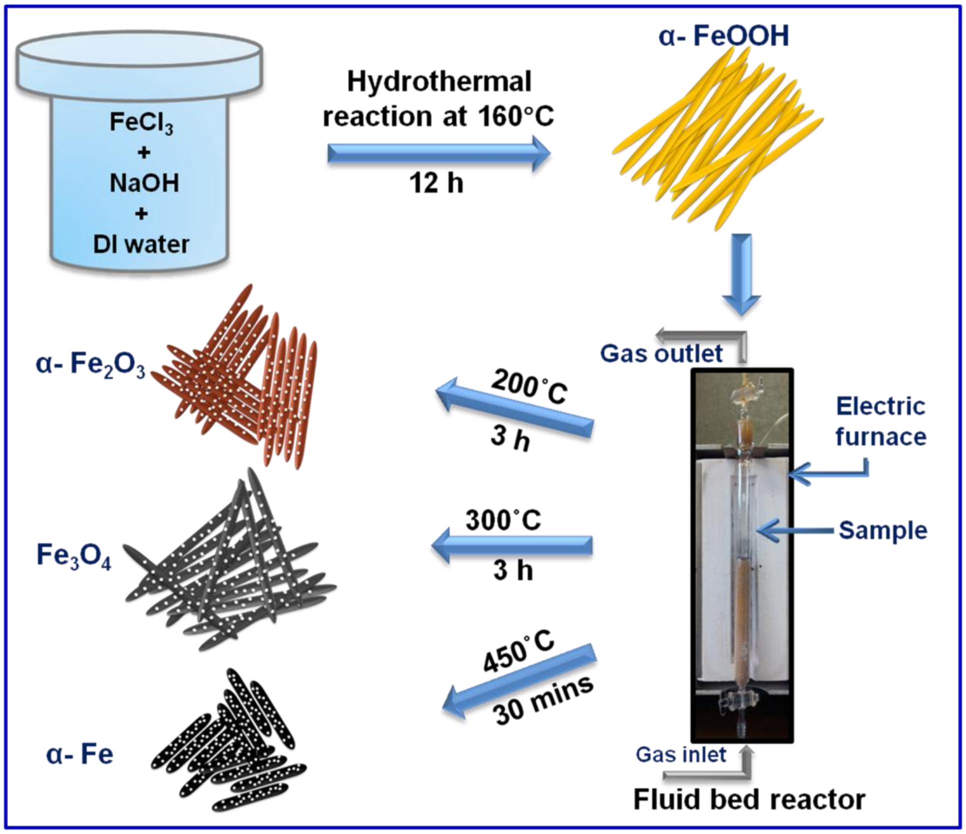

Figure 5.1 Illustration of the formation processes of α-FeOOH nanowires, α-Fe_2O_3, Fe_3O_4 and α-Fe nanowires/nanorods.

5.3 Results and Discussion

5.3.1 Morphology and Structure

In this section, detailed structural and morphological studies about phase transformation of iron-based systems have been correlated using XRD and TEM/HRTEM.

TEM/HRTEM was employed to investigate and assess the morphology and microstructure of nanowires/nanorods. Figure 5.2(a) shows a TEM image of the α-FeOOH nanowires. The length and diameter of nanowires are ~ 550 nm and ~ 30 nm, respectively. HRTEM image of a single nanowire is shown in Figure 5.2(b). Figure 5.2(c) shows a magnified view of the highlighted area marked by a white square in Figure 5.2(b). It reveals the single-crystalline structure of these nanowires. The interplanar spacing is measured to be 0.41 nm, corresponding to the (110) crystallographic orientation of α-FeOOH. The as synthesized precursor of α-FeOOH was yellow in color.

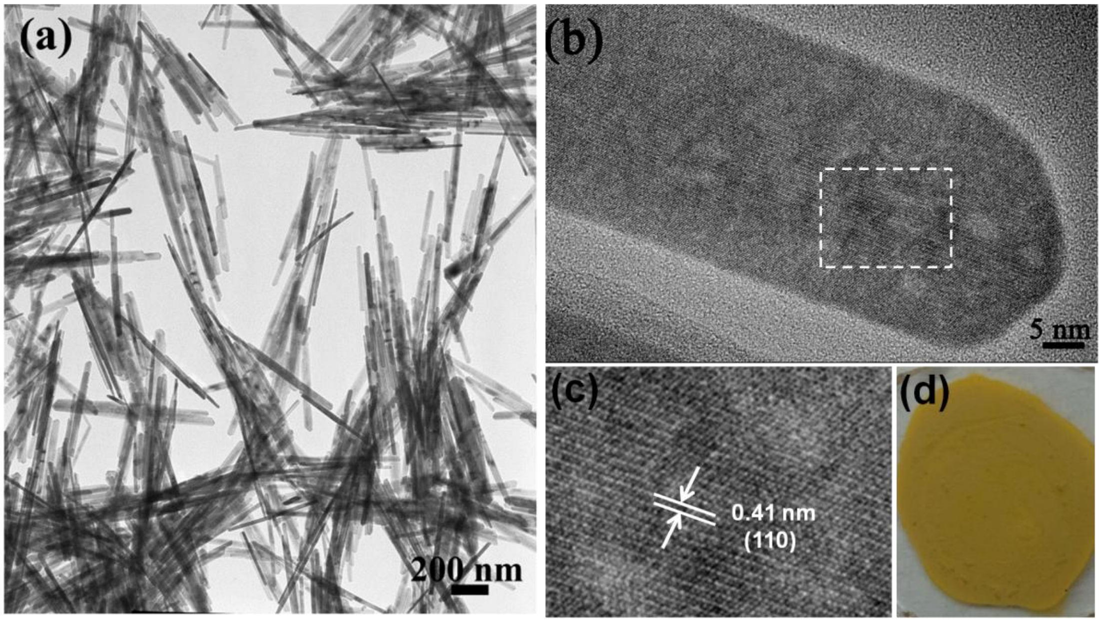

Figure 5.2 (a) TEM image, (b) Corresponding HRTEM image of α-FeOOH nanowires obtained in NaOH system at 160 °C for 12 h, (c) Magnification of selected mark zone in (b), and (d) Color of powder.

For typical morphology of nanowires, annealing at high temperature leads to undesirable aggregation and sintering, thus the characteristic of nanowires is not preserved. Fluidized reduction process is a dynamic process to induce phase transformation while preserving their morphology. It can be seen from TEM images that although thermal treatment was used to induce phase transformation, nanowires/nanorods have maintained 1D morphology. Figure 5.3(a) shows TEM image of α-Fe_2O_3 nanowires. By comparison with the precursor α-FeOOH, we can observe that on conversion from α-FeOOH to α-Fe_2O_3 phase, not only the nanowire shape but also the size are perfectly maintained. However, it should be noted that the α-FeOOH transforms into α-Fe_2O_3 with minor structural modifications, as expected for a topotactic transformation [116]. HRTEM image of a single nanowire in Figure 5.3(b) provides further insight into the surface modifications of α-Fe_2O_3. By careful observation of the HRTEM image in Figure 5.3(b), it is seen that there are many pores on the α-Fe_2O_3 nanowires. It is worth noting that the pores appeared to be contained within the annealed α-Fe_2O_3 nanowires. It can also be seen from the HRTEM image that along axial length of a nanowire there is variation in contrast, which signifies variation in surface thickness. This provides an additional insight into validity towards formation of pores. The origin of these pores in the α-Fe_2O_3 nanowires could be due to the decomposition of the α-FeOOH. HRTEM image and magnified view (Figure 5.3(c)) of highlighted area marked by a white square in Figure 5.3(b) reveal the single-crystalline structure of these nanowires. The interplanar spacing is measured to be 0.25 nm, which corresponds to the (110) crystallographic orientation of rhombohedral α-Fe_2O_3. We also noticed that the color of the dried precipitates changed from yellow to reddish brown after heating at 200 °C, suggesting a possible phase transition to hematite (Figure 5.3(d)).

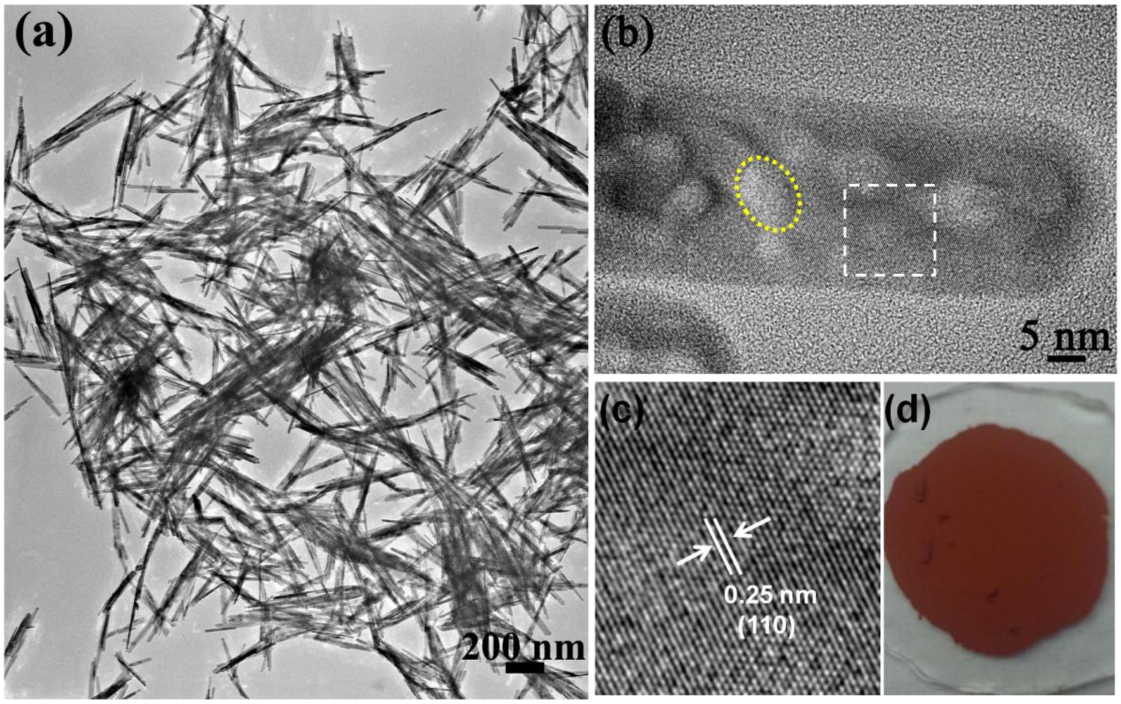

Figure 5.3 (a) TEM image, (b) Corresponding HRTEM image of α-Fe_2O_3 nanowires obtained by heating α-FeOOH nanowires at 200 °C for 3 h, (c) Magnification of selected white square mark zone in (b), and (d) Color of powder.

TEM observation (Figure 5.4(a)) of Fe_3O_4 nanowires reveals that the shape and length of these nanowires were maintained after the thermal annealing and reduction of the α-FeOOH precursor to Fe_3O_4. However, HRTEM image (Figure 5.4(b)) of a single nanowire shows that the diameter is increased and the pores are extended to the outer surface. This extension of pores leads to surface roughness at the edge of nanowires. It should be noted that the conversion from α-Fe_2O_3 to Fe_3O_4 involves sheaving of the oxide ion planes from AB to ABC stacking [117]. Figure 5.4(c) shows the magnified lattice-resolution HRTEM image of the nanowires marked by a white square in Figure 5.4(b). The interplanar spacing is measured to be 0.48 nm, corresponding to the (111) crystallographic orientation of cubic Fe_3O_4. The diameter of the nanowires is ~ 35 nm. The size of the pores is in the range of 10-14 nm, which is clearly visible in the HRTEM image in Figure 5.4(b). Further observation shows that the color of the dried precipitates changed from reddish brown to black after heating at 300 °C, which suggests a phase transformation to magnetite (Figure 5.4(d)).

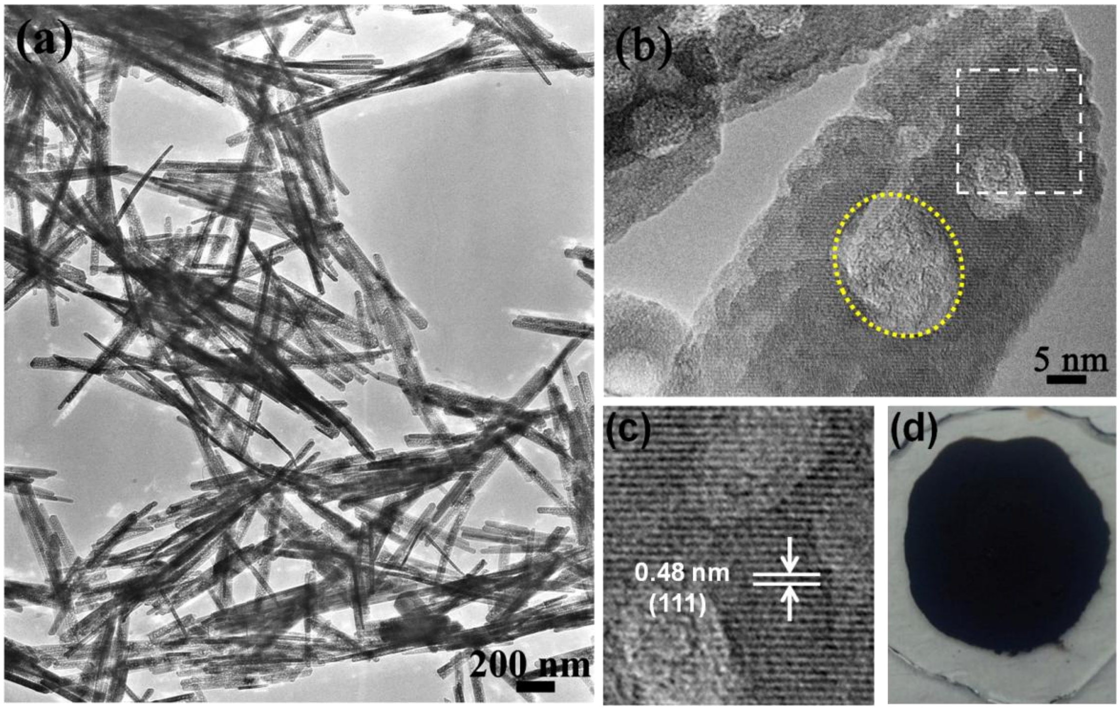

Figure 5.4 (a) TEM image, (b) Corresponding HRTEM image of Fe_3O_4 nanowires obtained by heating α-FeOOH nanowires at 300 °C for 3 h, (c) Magnification of selected white square mark zone in (b), and (d) Color of powder.

When the precursor α-FeOOH nanowires were fully reduced under an appropriate temperature, Fe nanorods were obtained, as shown in Figure 5.5. We have found that although the shape is preserved, there is a decrease in the size. In addition, some of the nanowires have broken into nanorods. The reduction of α-FeOOH to Fe phase results into elimination of all oxygen atoms from final Fe, thereby it results into decrease size and shrinkage of the structure. The length of the nanowires is reduced on conversion from α-FeOOH to Fe of ~ 200 nm. Figure 5.5(b) shows high magnification TEM image of Figure 5.5(a). Many pores have been observed on the Fe nanorods due to the reduction of the α-FeOOH and the release of H_2O. It is truly remarkable to synthesize mesoporous pure α-Fe nanorods using fluid bed process without template.

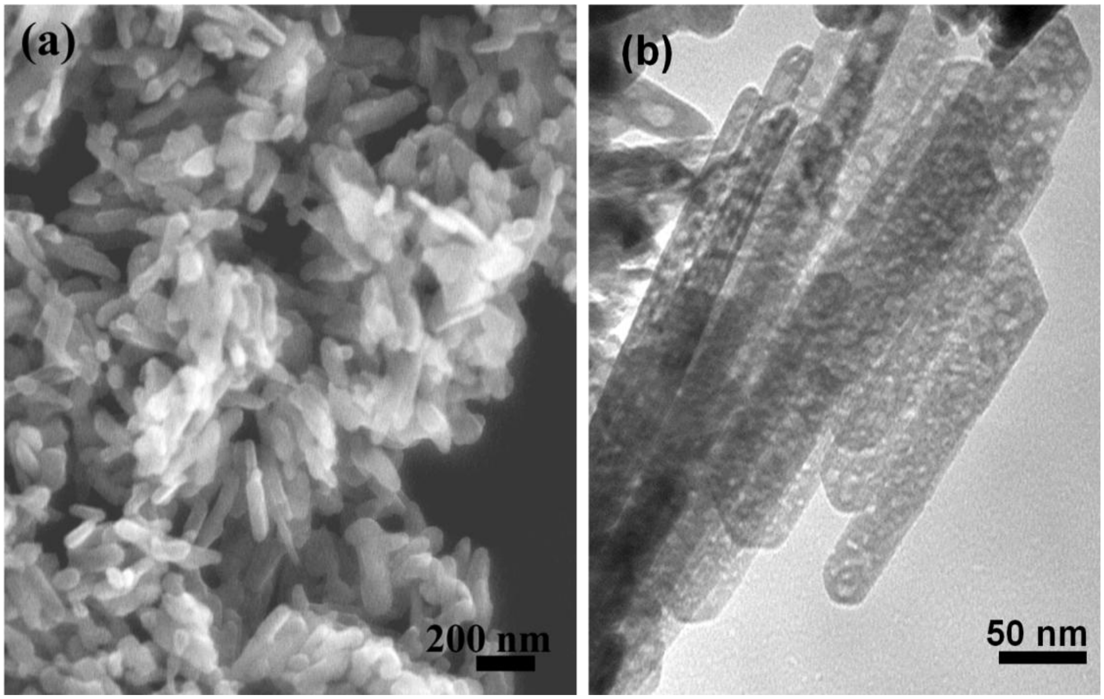

Figure 5.5 (a) HRSEM image and, (b) TEM image of α-Fe nanorods obtained by heating α-FeOOH nanowires at 450 °C for 30 min.

A detailed structural and morphological studies about phase transformation of iron-based systems have been correlated using XRD and TEM. The crystal structure and phase composition of the as-prepared precursor α-FeOOH and as-transformed samples were characterized using powder X-ray diffraction (XRD) (Figure 5.6). Figure 5.6(a) shows the XRD pattern of the as-synthesized α-FeOOH nanowires, where all the diffraction peaks can be indexed as orthorhombic α-FeOOH with lattice parameters of a = 4.618 Å, b = 9.952 Å, and c = 3.023 Å (JCPDS Card 81-0462). The crystal structure evolution of the nanowires/nanorods is clearly observed from the XRD pattern, which indicates a phase transformation upon varying annealing temperature and time. Figure 5.6(b) shows XRD pattern of α-Fe_2O_3, obtained by annealing the as-synthesized α-FeOOH nanowires in the fluidized bed reactor at 200 °C for 3 h. It is evident that all of the expected peaks can be indexed to the rhombohedral structure of α-Fe_2O_3 with lattice parameters a = b = 5.034 Å, c = 13.762 Å (JCPDS Card 85-0987). Figure 5.6(c) shows the XRD pattern of the Fe_3O_4 nanowires obtained by annealing the as-prepared α-FeOOH nanowires in the fluidized bed reactor at 300 °C for 3 h, where all the diffraction peaks can be indexed as cubic spinel structure with lattice parameter a = b = c = 8.390 Å (JCPDS Card 72-8151). It can be perceived from Figure 5.6 (b-c) that the thermal treatment induced transformation of α-FeOOH to α-Fe_2O_3 and Fe_3O_4 respectively is pure in phase. However, a mixture of Fe_3O_4 and Fe phases was obtained when the as-prepared α-FeOOH nanowires were annealed in the fluidized bed reactor at 400 °C (Figure 5.6(d)). When the as-prepared α-FeOOH nanowires were annealed in the fluidized bed reactor at 450 °C for 30 min α-Fe was obtained. XRD pattern shown in Figure 5.6(e) can be attributed to the body-centered cubic crystal structure of Fe (JCPDS No. 71-3763). It is noteworthy that only pure α-Fe is formed without any remaining precursor or other byproducts (such as magnetite Fe_3O_4 phase). It is concluded from the XRD patterns that a complete phase transformation can be achieved by this method.

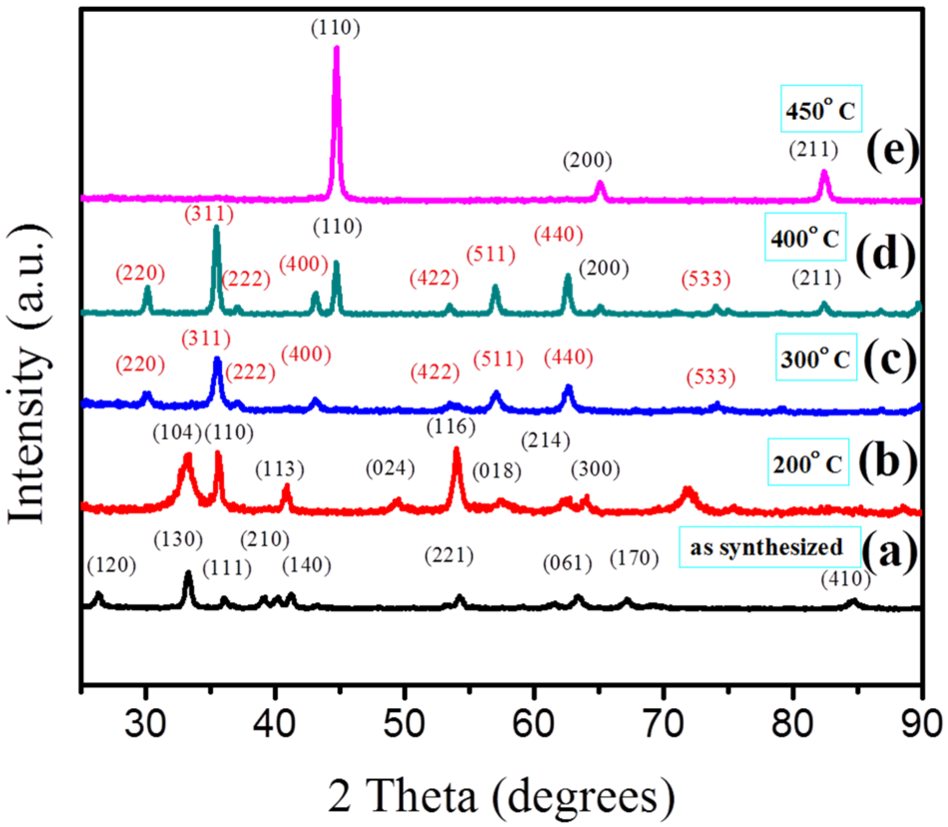

Figure 5.6 X-ray diffraction patterns of the (a) as-synthesized α-FeOOH nanowires, (b) α-Fe_2O_3 nanowires, (c) Fe_3O_4 nanowires, (d) Fe_3O_4+α-Fe nanowires mixture, and (e) α-Fe nanorods.

5.3.2 Surface Area

Porous materials owing its adsorption properties are often a prerequisite to study specific area. Mesoporous nanowires/nanorods have a higher surface to volume ratio compared to nanoparticles. Therefore it is important to better characterize its enhanced specific area. The BET specific surface areas and porosity of α-FeOOH, α-Fe_2O_3, Fe_3O_4 and Fe nanowires/nanorods were studied by nitrogen adsorption–desorption analysis. As shown in Figure 5.7, the BET specific surface area of α-FeOOH, α-Fe_2O_3, Fe_3O_4 and Fe nanowires/nanorods are 52.71, 82.00, 55.20 and 24.77 m^2g^{-1}, respectively. It is apparent that the specific surface area of the mesoporous α-Fe_2O_3 and Fe_3O_4 samples are higher than that of the non-porous α-FeOOH. The mesoporous α-Fe_2O_3 nanowires have the highest specific surface area among these phases due to the appearance of the pores on the nanowires. The total BET surface areas steadily decrease from α-Fe_2O_3 nanowires and Fe nanorods, as the reduction temperature of the samples increases. This phenomenon can be explained as a consequence of the surface self-diffusion of Fe atoms, resulting in coarsened ligaments, fragmentation and aggregation, which leads to reduced surface area and surface energy [118, 119]. The average pore diameters calculated from the nitrogen isotherms (according to the BJH plots) of the porous α-Fe_2O_3, Fe_3O_4 and Fe nanowires/nanorods were 13.7, 13.9 and 8.3 nm, respectively indicating all the samples contains mesoscale pores. The pore diameter was reduced for the Fe nanorods and it is speculated that atomic diffusion during the reduction heat treatment could cause some filling of the holes in the nanorods. Based on the above discussion, it is believed that any possibility to incorporate dopant into porous nanowires may arouse great interest in nanotechnology. These porous nanostructures could also satisfy the requirements for potential applications in the field of surface catalysis.

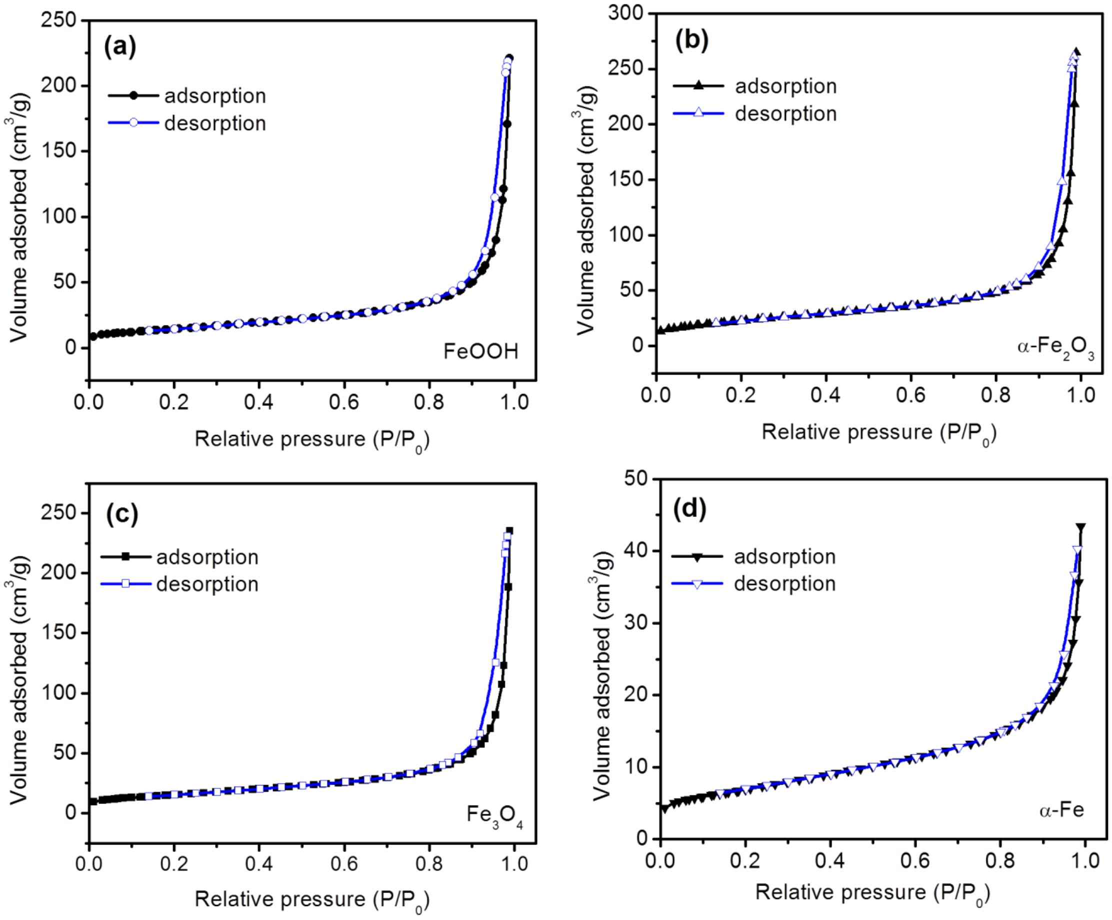

Figure 5.7 Nitrogen adsorption-desorption isotherms of the (a) α-FeOOH, (b) α-Fe_2O_3, (c) Fe_3O_4 and (d) α-Fe nanowires/nanorods.

5.3.3 Magnetic Properties

The magnetic properties of the samples before and after the thermal treatment were measured at 300 K (Figure 5.8). Figure 5.8(a) shows the M-H curve of the as-synthesized α-FeOOH nanowires. A paramagnetic response of the α-FeOOH sample is apparent. Iron based materials have intriguing magnetic properties because of their structure and morphology, owing to shape anisotropy and magnetocrystalline anisotropy. In this study of 1D nanostructures, it is expected that the effective magnetic anisotropy is dominated by the shape anisotropy. To understand the effect of the shape anisotropy, nanowires were aligned in the presence of an external magnetic field.

Figure 5.8(b) shows the magnetic hysteresis loops of the aligned α-Fe_2O_3 nanowires measured along the directions parallel and perpendicular to the alignment direction. The effect of alignment in porous nanowires is remarkable and it is clearly visible in the expanded view of hysteresis loops shown in the inset of Figure 5.8(b). A remanence magnetization M_r = 0.64 M_S (saturation magnetization) and coercive field H_C = 412 Oe are obtained when measured parallel to the alignment direction, while a M_r = 0.32 M_S and H_C = 355 Oe are obtained when measured perpendicular to the aligned wires. This observation is consistent with the previous report that alignment of the nanowires leads to enhanced remanent magnetization (to be about twice the value), due to the effect of shape anisotropy [74].

Figure 5.8(c-d) shows the magnetic hysteresis loops of Fe_3O_4 nanowires and Fe nanorods measured parallel and perpendicular to the aligned direction. The magnetization curve of the Fe_3O_4 nanowires and Fe nanorods parallel to aligned nanowires exhibited a M_r of 0.51 M_S and 0.43 M_S and a H_C of 583 Oe and 628 Oe (Figure 5.8(c-d)), respectively. When the samples were measured perpendicular to alignment direction, the M_r of 0.30 M_S and 0.27 M_S were obtained. The effect of magnetic alignment led to a change in the squareness of the magnetic hysteresis loops, indicating the influence of shape anisotropy [74]. However, this change in the loop shape does not lead to dramatic changes in the coercive field. The high-temperature annealing can cause a recrystallization (change in grain size) and the influence of preferred orientation of the crystallites in nanowires will affect the magnetic anisotropy and thereby contribute to these discrepancies [120, 121].

The saturation magnetization (M_S) values of 3, 77 and 197 emu/g were obtained for the α-Fe_2O_3, Fe_3O_4 and Fe nanowires/nanorods, respectively. As the phase transformation proceeded, the magnetic properties of the sample gradually transformed from paramagnetic to ferromagnetic. It is known that in 1D Fe nanostructures, the magneto-crystalline anisotropy is often lower than that of the shape anisotropy, so that the coercivity is mainly dominated by the shape anisotropy [122]. Thus, the large values of H_C in the as-synthesized nanowires may be attributed to the distinctive one-dimensional anisotropic structure of the magnetic nanowires with high shape anisotropy [123].

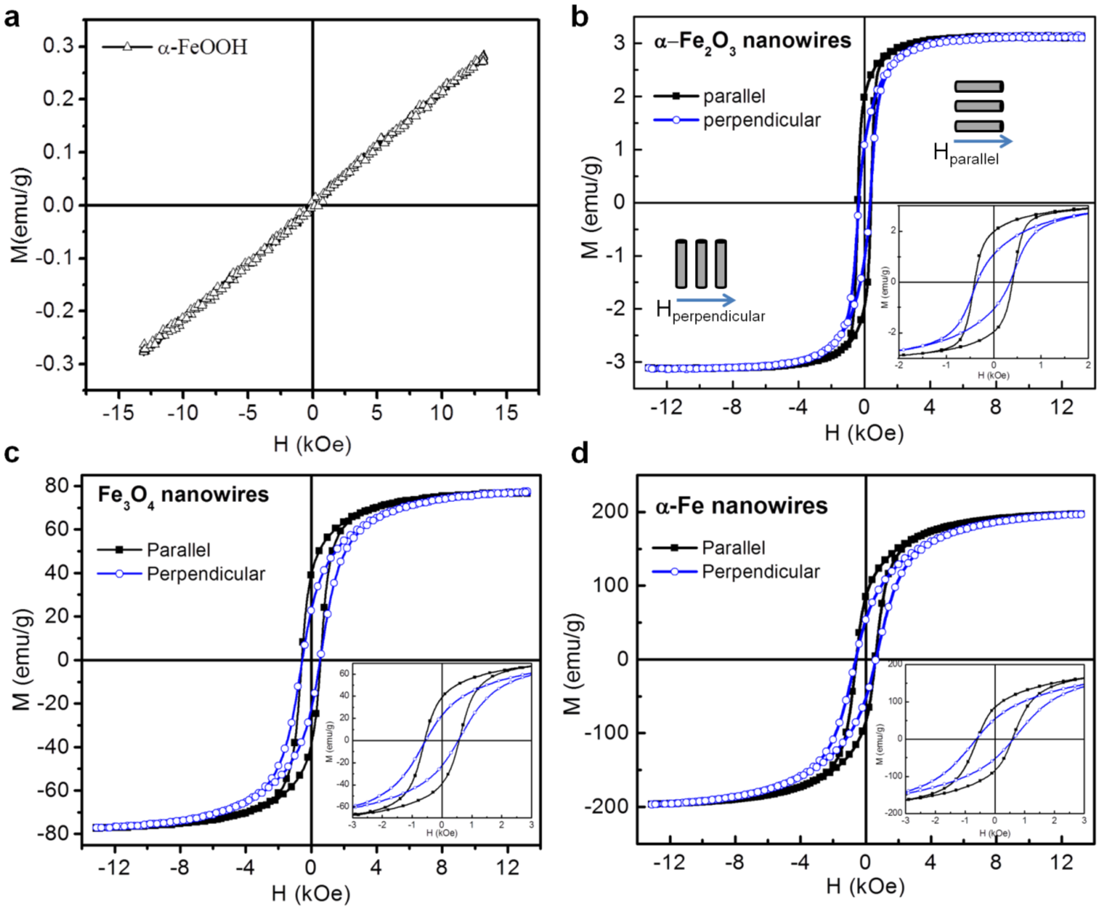

Figure 5.8 Magnetic hysteresis loops of (a) as-prepared α-FeOOH nanowires, and aligned (b) α-Fe_2O_3 nanowires, (c) Fe_3O_4 nanowires, and (d) α-Fe nanorods (along parallel and perpendicular direction). The insets show the magnification of M_r and H_C.

5.4 Conclusion

In summary, we have successfully synthesized the α-Fe_2O_3, Fe_3O_4 and α-Fe nanowires/nanorods by the fluidized bed reduction of as-synthesized α-FeOOH nanowires obtained by hydrothermal method. The structural, magnetic properties and specific-surface area of the prepared nanowires have been investigated systematically. The magnetic hysteresis measurements indicate that the as-synthesized α-Fe_2O_3, Fe_3O_4 and α-Fe nanowires/nanorods all show ferromagnetic behavior. The aligned α-Fe_2O_3, Fe_3O_4 and α-Fe nanowires/nanorods showed enhanced remanence in parallel direction compared to the perpendicular direction which indicates the effect of shape anisotropy. Owing to the excellent physical and magnetic properties of the iron and iron oxides, it is expected that the porous nanowires/nanorods may find important applications in the future for magnetic recording media, gas, and heavy metal ion adsorbents, catalysts, hydrogen and Li ion storage.

Chapter 6

Binary Alloy Nanowires: FeCo and CoNi

In this work, FeCo and CoNi nanowires were selected to study the structure and magnetic properties due to the Fe [124], Co [74, 125], Ni [126] and binary alloys of CoNi [127], FeNi [128] and FeCo [129] have higher magnetic moments than their corresponding oxides. FeCo and CoNi nanowires were synthesized using the solution-based polyol process due to its potential applications in such as exchange-coupled nanocomposite magnets, potential materials for advanced recording media, and magnetic carriers in biomedical application. By varying the reaction parameter such surfactant concentration, catalyst concentration and composition parameters, single crystal structures with different shapes such as dumbbells, rods or wires have been achieved. The possible mechanisms are also discussed. These nanostructures within nanowires may be useful for the exploration of new nanodevices. The magnetic properties of these alloy nanowires will be discussed.

6.1 FeCo Alloy Nanowires

6.1.1 Introduction

Among Fe, Co, Ni, CoNi, FeNi and FeCo materials, the FeCo nanowires are of special interest due to the unique properties of FeCo alloys including a high saturation magnetization, high permeability and high Curie temperature, which are desired for many applications [130]. FeCo alloy nanoparticles show excellent soft magnetic properties such as high saturation magnetization M_S with negligible magnetocrystalline anisotropy. Therefore, to increase coercivity of the materials, an effective strategy is to enhance effective magnetic anisotropy by introducing shape anisotropy, which is proportional to the square of M_S. FeCo nanowires are thus expected to have higher coercivity than spherical FeCo nanoparticles. Enhanced shape anisotropy of the FeCo nanowires could lead to magnetic alignment. Moreover elongated particles can also have an advantage over spherical particles in forming an ordered structure for developing texture by self-assembly. FeCo nanowires could exhibit a larger coercive force at room temperature compared to FeCo nanoparticles due to enhancement of magnetic anisotropy by shape anisotropy [131].

Several different methods have been employed to synthesize magnetic FeCo nanowires of different stoichiometry, including template-based electrodeposition methods and chemical solution methods. Most template based methods produce polycrystalline FeCo nanowires, with amorphous carbon present on the surfaces of the nanowires [132-136]. Other approaches, such as the thermal decomposition of Fe and Co carbonyls, also produce polycrystalline FeCo nanowires [137]. However, the synthesis of single-crystal FeCo magnetic nanowires by a chemical solution method without using a template or catalyst still remains a challenging task due to its unpredictable growth process [136, 138]. Moreover, it was found that single-crystal nanowires with alignment have better magnetic properties than those of polycrystalline nanowires in terms of coercivity and hysteresis loop squareness [139].

In this work, we have synthesized single-crystal FeCo nanowires using the reductive decomposition of organometallic precursors in the presence of surfactants. Study of the effects of the surfactant ratio, Fe to Co precursors ratio and the heating rate on the morphology, structure and magnetic properties of the nanomaterial is presented.

6.1.2 Experimental

In a typical nanowire synthesis procedure, 0.75 mmol of iron (III) acetylacetonate ($Fe(acac)_3$), 0.5 mmol of cobalt acetylacetonate ($Co(acac)_2$) and 1.5 mmol 1,2-hexadecanediol (HDD) were added to a 125 mL flask with a magnetic stir bar and mixed with 4.37 mmol (1.4 ml) of oleic acid (OA). After purging 20 min at room temperature using forming gas (Ar 93% + H_2 7%), 5 mmol (2.28 ml) of trioctylphosphine (TOP) was injected into the reaction mixture, after which the temperature was raised to 100 °C and kept constant for 10 min. Afterwards, the flask was heated to 200 °C at 10 °C per min and the temperature was held for 30 min. Then the flask was heated to 300 °C, where it was held for 90 min. The heating rate was varied from 2 to 15 °C per min when the reaction was heated from 200 °C to 300 °C. The reactor was purged with forming gas throughout all reactions. $Fe_{60}Co_{40}$ nanocrystals were obtained by adjusting the initial molar ratio of $Fe(acac)_3$ and $Co(acac)_2$ precursors (Figure 6.1).

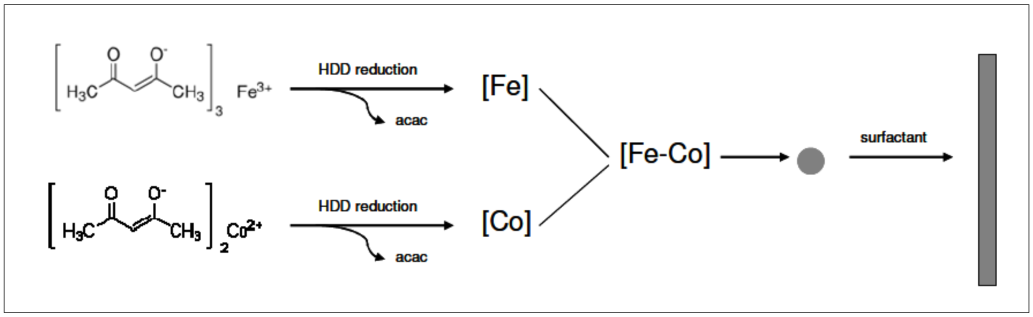

Figure 6.1 Schematic illustration of FeCo nanowires forming from the reduction $Fe(acac)_3$ and $Co(acac)_2$.

6.1.3 Purification and Characterization of FeCo Nanowires

After cooling to room temperature, the product was collected from the surface of a magnetic stir bar and dispersed in hexane (10 ml) and precipitated using absolute ethanol (40 ml). That product was washed three times using a mixture of hexane and absolute ethanol (10 ml hexane and 40 ml ethanol) and finally dispersed in hexane. To prepare TEM samples, a drop of nanocrystals dispersion solution in hexane was put on a 300-mesh carbon coated cooper TEM grid. The solvent was evaporated slowly in the air and nanocrystals were well dispersed on the grid. XRD was recorded on a Rigaku Ultima IV diffractometer with a Cu X-ray source. The magnetic hysteresis measurements were carried out using an alternating gradient magnetometer (AGM) with maximum magnetic field of 14 kOe. Samples for magnetic characterization were prepared by depositing a drop of the $Fe_{60}Co_{40}$ nanowires hexane dispersion on a silicon substrate, evaporating the solvent at room temperature and hardening the randomly oriented FeCo powders in epoxy.

6.1.4 Results and Discussion

6.1.4.1. Effect of Surfactant/Precursor Concentration Ratio

FeCo nanocrystals with different sizes and shapes were synthesized via modified reductive decomposition in a mixture of two surfactants [59]. Various combinations of OA and TOP surfactants were studied at fixed precursor concentration and fixed reaction temperature. Specific surfactants have preferential adsorption on different crystal facets, which allows growth along one facet while inhibiting growth along other facets [140]. We studied the effect of change in surfactant/precursor-concentration ratio in order to observe size and shape control of the nanocrystals. In this experiment, TOP (Trioctylphosphine) and OA (Oleic acid) are surfactants with –P and –COOH function groups (Figure 6.2).

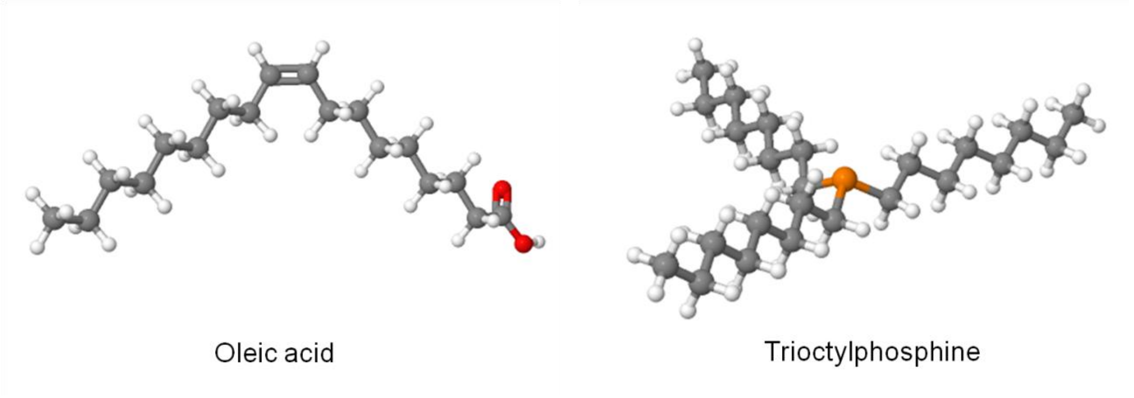

Figure 6.2 Molecular structures of surfactants Oleic acid (OA) and Trioctylphosphine (TOP).

The TEM images in Figure 6.3 show that varying the molar ratio of surfactant OA to Fe and Co metal precursor can control the size and shape of nanocrystals. During chemical synthesis, amount of metal precursors $Fe(acac)_3$ (0.75 mmol), $Co(acac)_2$ (0.5 mmol) and surfactant TOP (5.0 mmol) were held constant. The heating rate during reaction was maintained at 10 °C/min. FeCo nanoparticles with diameters of 12-25 nm were formed (Figure 6.3(a)) when the molar ratio of OA to Fe+Co metal precursor was 2.5:1. By increasing the molar ratio to 3.0:1, a mixture of particles with diameters of 6-25 nm and nanowires of length 40-60 nm and diameters of 2-3 nm were obtained. A further increase in molar ratio to 3.5:1 (Figure 6.3(c)) led to formation of nanowires of lengths of 60-140 nm and diameters of 4-8 nm. The products became a mixture of nanorods and nanoparticles (Figure 6.3(d)) when molar ratio was increased to 4.0:1.

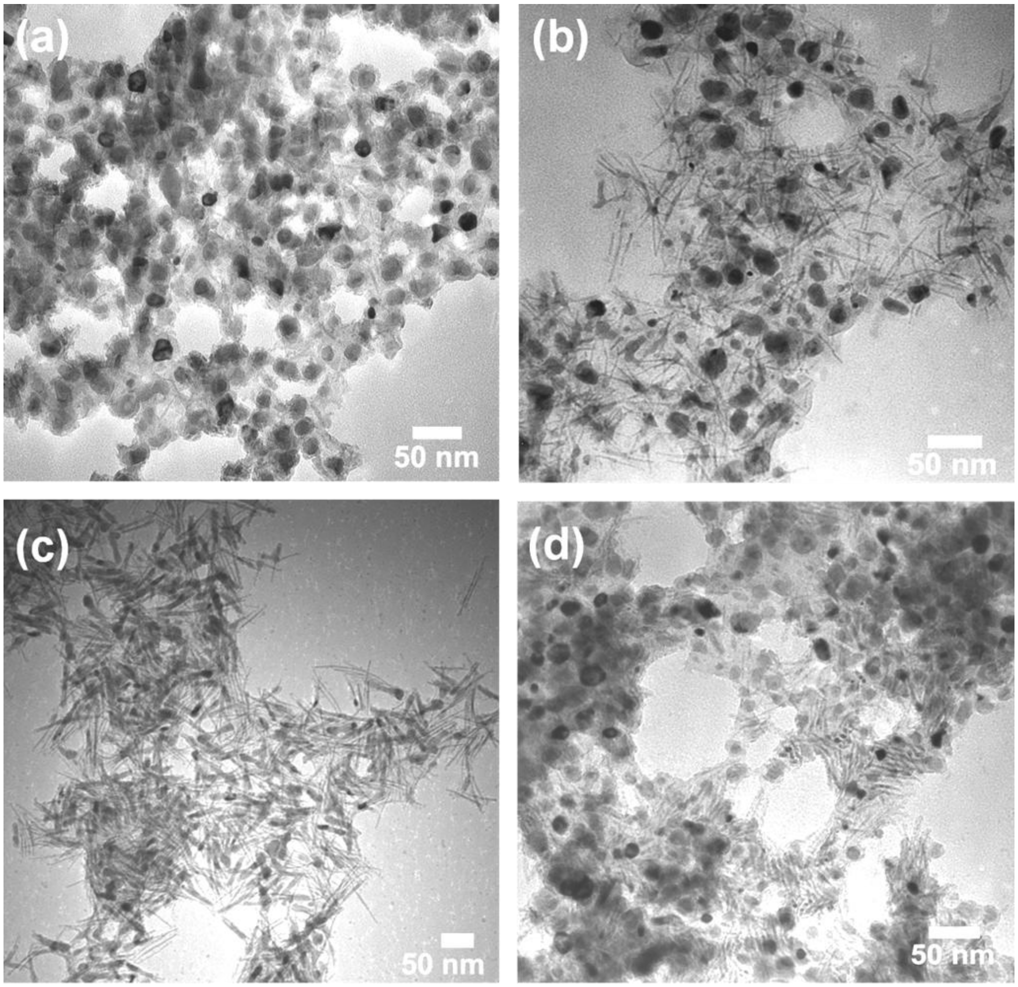

Figure 6.3 TEM images of FeCo nanocrystals synthesized by varying the molar ratio of surfactant (OA) to metal precursor (Fe+Co): (a) 2.5:1, (b) 3:1, (c) 3.5:1 and (d) 4:1.

Figure 6.4(a) shows an HRTEM image of a monocrystalline FeCo nanowire. The interplanar spacing of the nanowire is 0.20 nm, which corresponds to FeCo (110) oriented along the wire axis (Figure 6.4(b)). The fast Fourier transform (FFT) from the image shown in Figure 6.4(a) also exhibits the FeCo (110) lattice spacing (Figure 6.4(c)). We believe these results will motivate further studies on the effect of alignment and magnetic properties of FeCo nanowires oriented along the (110) plane. Elemental compositions of the nanowires were analyzed using EDX. The EDX spectra (Figure 6.4(d)) of samples give atomic composition ranges of the nanowires of Fe from 57-63 at.% and Co 43–37 at.% when 1.5:1 molar ratios of Fe to Co precursors was used. The presence of phosphorus, carbon and oxygen were due to the reaction conditions used for the synthesis of the FeCo nanowires. The excess carbon and Cu were from the TEM grid.

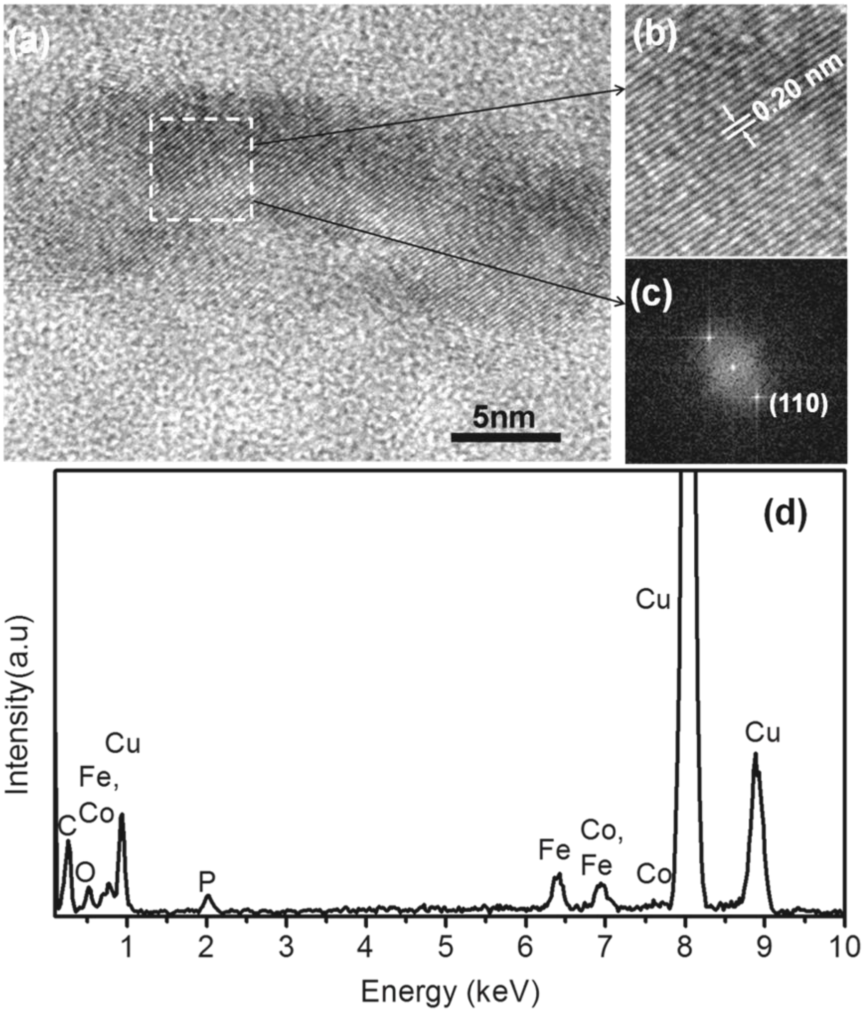

Figure 6.4 (a) HRTEM image of a FeCo nanowire, (b) magnification of FeCo nanowires in the zone marked in (a) with a dashed square, (c) FFT image of the zone marked with a dashed square, (d) EDX spectra of FeCo nanowires.

Figure 6.5 shows the TEM images of FeCo nanocrystals after varying the molar ratio of TOP to the Fe and Co metal precursors. During chemical synthesis, amount of metal precursors Fe(acac)$_3$ (0.75 mmol), Co(acac)$_2$ (0.5 mmol) and surfactant OA (4.37 mmol) were held constant. The heating rate during the reaction was maintained at 10 °C/min. As seen in Figure 6.5(a), without TOP, only spherical particles with diameters of 10-25 nm were obtained. By introducing TOP into the reaction using the (TOP/Fe+Co) molar ratio of 2:1, the average particle size increased (Figure 6.5(b)). Nanowires were obtained when (TOP/Fe+Co) molar ratios of 4:1 and 8:1 were used in the reaction (Figure 6.5(c-d)).

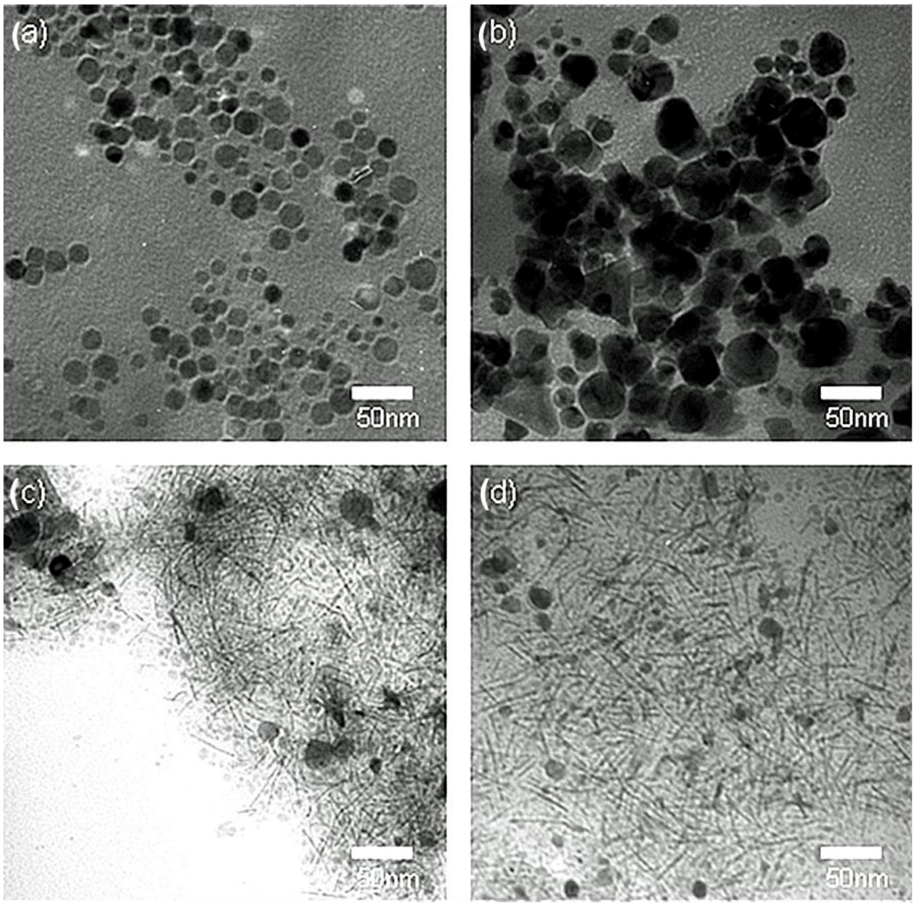

Figure 6.5 TEM images of FeCo nanocrystals synthesized with varying molar ratio between surfactant (TOP) and metal precursors (Fe+Co): (a) without addition of TOP, (b) 2:1, (c) 4:1, and (d) 8:1.

6.1.4.2. Effect of Precursor Concentration Ratio

Figure 6.6 shows the TEM images of the FeCo nanocrystals with different composition. The molar ratios of the Fe and Co in the nanoparticles were controlled using the organometallic precursor ratio. For example, FeCo nanocrystals of atomic percentage 60 to 40 for Fe to Co were obtained by feeding an initial molar ratio of 1.5:1 for Fe and Co metal precursors, whereas an atomic percentage of 50:50 for Fe:Co was obtained when an initial feeding molar ratio was 1:1 for Fe to Co metal precursors. For $Fe_{10}Co_{90}$ only spherical particles with the size of 10-25 nm were obtained (Figure 6.6(a)). When the concentration of Fe increases to $Fe_{30}Co_{70}$, a mixture of nanowires and aggregated particles was produced (Figure 6.6(b)). Further increasing Fe precursor concentration to $Fe_{60}Co_{40}$ it leads to formation of nanowires of length 60-140 nm and diameter 4-8 nm were obtained (Figure 6.6(c)). By increasing the Fe precursor amount relative to Co to $Fe_{70}Co_{30}$, nanoparticles with the size of 10-25 nm were obtained (Figure 6.6(d)).

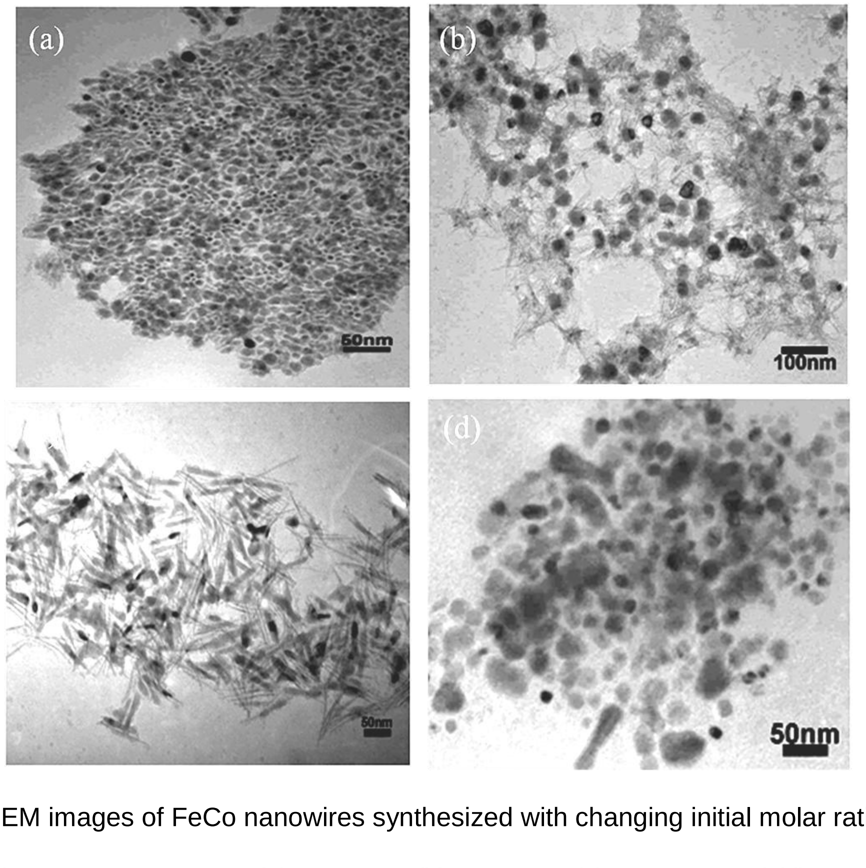

Figure 6.6 TEM images of FeCo nanowires synthesized with changing initial molar ratio between Fe and Co metal precursor: (a) $Fe_{10}Co_{90}$, (b) $Fe_{30}Co_{70}$, (c) $Fe_{60}Co_{40}$ and (d) $Fe_{70}Co_{30}$.

6.1.4.3 Growth Mechanism

The possible formation mechanism of the FeCo nanowires can be illustrated as previously reported in similarly designed studies [141, 142]. In the early stage of the synthesis, a common mild reducing agent (1,2-hexadecanediol) was used to enables co-reduction of Fe and Co ions to the corresponding reduced atomic state at an elevated temperature. The rapidly produced Fe and Co atoms reached a supersaturation level initiating a burst nucleation, depending on the level of supersaturation, which controllled the initial number of nuclei containing Fe-Co atoms. This mechanism is the classic LaMer theory, which suggests a burst nucleation followed by a diffusional growth, leading to monodisperse nanoparticles, due to the temporally discrete nucleation [64]. The remaining solvated Fe and Co atoms along with the surfactant-complexed atomic species interact with the nuclei through diffusional growth until the atoms are depleted from the fluid medium. The preferred growth direction of the nanoparticles when nanowires or rods are formed can be induced through control of the type of surfactant and the surfactant concentration. Usually, a multi-surfactant system favors the formation of an anisotropic nanostructure [143]. In our case, the employed TOP and OA both can act as surfactants to cover different crystallographic surfaces of newly formed nanocrystal seeds, and eventually lead to the anisotropic growth toward the (110) axis, forming a one-dimensional nanostructure. The shape of the nuclei can have a strong effect on the shape of the final nanocrystals, for example, through selected growth of high-energy crystal faces of the nuclei [144]. However, the metallic nanowire and nanorod structures are not thermodynamically favorable and commonly transition to a spherical shape if the reaction is not quenched at the proper time and temperature. It has also been reported that nuclei may initially follow diffusional growth to form primary small particles, which then aggregate into the final particles; this process is the so-called “aggregation of subunits” mechanism [141, 145]. Further, if nucleation is not a one-time event or if nuclei cannot grow at the same time, an Ostwald ripening process will occur. This diffusion limited Ostwald ripening process was first quantified by Lifshitz and Slyozov [66]. During this process, the smaller particles dissolve (due to their high surface energy), feeding the growth of larger particles. In this study, we propose that the nanowires were formed by the burst nucleation and diffusional growth mechanism. The lack of observed polycrystalline nanowires suggests that growth through aggregation did not occur.

Figure 6.7(A) shows the XRD patterns of the FeCo nanocrystals prepared by varying the molar ratio of surfactant OA to Fe and Co metal precursors, which show the diffraction peaks of FeCo phase with body-centered-cubic (bcc) crystal structure (Figure 6.7(A) (a)-(d)). The strongest reflection for FeCo alloy corresponded to the (110) lattice plane. Figure 6.7(B) shows the XRD patterns of the FeCo nanoparticles and nanowires prepared by varying the TOP concentration, which show that the as-synthesized FeCo nanocrystals have a bcc structure. We observed the presence of a Fe_3O_4 phase in the XRD pattern along with FeCo when no TOP was added into the reaction (Figure 6.7(B) (a)). For molar ratios of (TOP/Fe+Co) higher than 2:1, the Fe_3O_4 phase was not detected by XRD. Since TOP is very reactive with oxygen, it can consume the oxygen molecules in the solution to prevent the oxidation of the metal atoms.

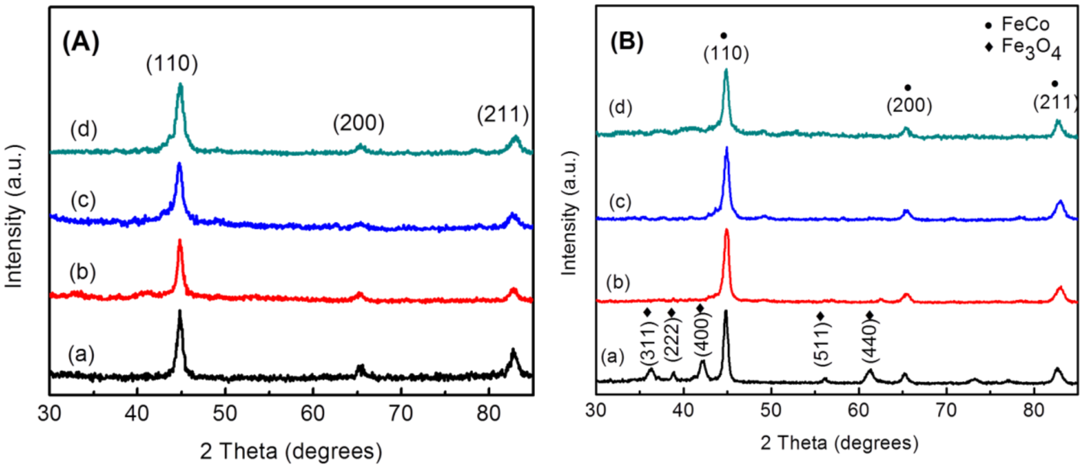

Figure 6.7 (A) XRD of FeCo nanocrystals with bcc structure synthesized with varying molar ratio between surfactant (OA) and metal precursors (Fe+Co): (a) 2.5:1, (b) 3:1, (c) 3.5:1 and (d) 4:1. (B) XRD patterns of FeCo nanocrystals synthesized with varying molar ratio between surfactant (TOP) and metal precursors (Fe+Co): (a) without addition of TOP, (b) 2:1, (c) 4:1, and (d) 8:1.

6.1.4.4 Magnetic Properties

Figure 6.8(A) shows hysteresis loops of randomly oriented as-prepared FeCo nanocrystals. All of the as-prepared FeCo nanocrystals are ferromagnetic at room temperature. It was found that magnetic properties including coercivity and saturation magnetization strongly depend on the morphology of the FeCo nanocrystals. By increasing the molar ratio (OA/Fe+Co) from 2.5 to 3.5, both the coercivity and saturation magnetization increased and then decreased with a further increase in the molar ratio to 4.0:1 (corresponding to 1.6 ml), as shown in Figure 6.8(B) and also values listed in Table 6-1. Figure 6.3 shows that OA concentration is vital in controlling the morphology, including the aspect ratio of FeCo nanocrystals, which in turn is related to magnetic properties of the nanocrystals. The highest coercive force of 1.2 kOe and a saturation magnetization of 92 emu/g were obtained when the molar ratio of (OA/Fe+Co) was 3.5. This led to formation of nanowires with the highest aspect ratio (~ 35) as seen in Figure 6.3(c). A ratio of remanence to saturation magnetization (M_r/M_S) of ~ 0.5 was obtained for the FeCo nanowire assembly of randomly oriented nanowires.

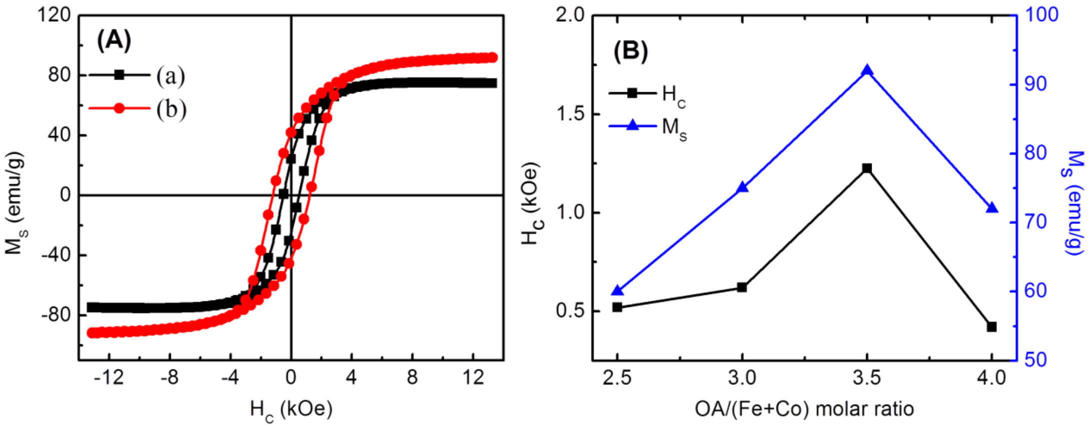

Figure 6.8 (A) Hysteresis loops of FeCo nanowires synthesized with varying molar ratio between surfactant (OA) and metal precursors (Fe+Co): (a) 2.5:1 and (b) 3.5:1. (B) Change of coercivity and saturation magnetization with varying molar ratio of (OA/Fe+Co).

Table 6-1 Coercivity and saturation magnetization with varying molar ratio of (OA/Fe+Co).

OA/Fe+Co molar ratio	H_C (kOe) (at 300K)	M_S (emu/g)
2.5:1	0.52	60
3:1	0.62	75
3.5:1	1.22	92
4:1	0.42	72

The presence of surfactants on the surface of nanocrystals causes difficulty in determining actual magnetization value [96]. It is difficult to completely remove the surfactant (mainly TOP) from the surfaces of the nanocrystals. The relatively low saturation magnetization could be attributed to a thick layer of surfactant on the surface and a surface spin-canting effect [146, 147]. On the other hand, the saturation magnetization values obtained in our measurements for each sample are independent of the sample morphology and orientation, because the field we used (>12 kOe) has overcome the anisotropy fields and reached the saturation.

6.1.5 Conclusion

Ferromagnetic FeCo nanocrystals with different morphology have been synthesized via reductive decomposition of organometallic precursors in the presence of surfactants. The sizes and shapes of the nanocrystals were found to be dependent on the reaction conditions such as the surfactant ratio, precursor concentration and heating rate. Synthesized nanocrystals have a body-centered-cubic (bcc) crystal structure for both particles and nanowires and the (110) crystalline direction is along the long axis of the nanowires. Magnetic properties including coercivity and saturation magnetization are strongly dependent on morphology of the FeCo nanocrystals. A maximum saturation magnetization of 92 emu/g and coercive force up to 1.2 kOe were obtained at room temperature for the $Fe_{60}Co_{40}$ nanowires of lengths of 60-140 nm and diameters of 4-8 nm.

6.2 CoNi Alloy Nanowires

6.2.1 Introduction

In this work, we have synthesized CoNi nanorods and nanowires by reduction in liquid polyol. CoNi nanorods and nanowires with hexagonal closed-packed (hcp) structure have shown very interesting magnetic properties because of the high shape anisotropy [122]. A variety of techniques have been used to synthesize the nanowires and nanorods including template methods [148, 149], solvothermal route [150-152], chemical vapor deposition method [153], microemulsion system [154], and direct precipitation of anisotropic metal nanoparticles from solution [155-157]. In previous studies, nucleating agents such as K_2PtCl_4, $AgNO_3$ were used for morphology control of CoNi alloy particles via heterogeneous nucleation [61]. When Ag and Pt were used as nucleating agent, final products appear to be spherical particles with main phase of face-centered cubic (fcc) structure. In this work, we report morphology control of CoNi nanowires by modifying the polyol reduction of cobalt acetate and nickel acetate using $RuCl_3$ as the catalyst [158]. The noble metal catalyst $RuCl_3$ is easy to be reduced at relatively lower temperatures, compared with Co^{2+} and Ni^{2+}. They form nanoclusters or nanoparticles serving as heterogeneous nucleation sites and facilitate the nucleation process. Due to the same structure to hcp cobalt, ruthenium becomes an ideal catalyst for the growth of CoNi nanocrystals.

By varying the catalyst concentration in proper ranges, the effect of synthetic parameters on controlling cobalt-nickel particles with different shapes such as dumbbells, rods or wires is demonstrated. We have also investigated dependence of magnetic properties on the morphology of CoNi nanocrystals.

6.2.2 Experimental

6.2.2.1 Synthesis in Flask

The synthesis was handled with a standard airless technique in an Argon atmosphere. The reagents were obtained from commercial sources and used without further purification. In typical synthesis, 0.4 g of mixture of cobalt and nickel acetate tetrahydrate and 0.126 g of NaOH were dissolved in 15 mL of 1, 2-butanediol with mechanical stirring. Then, 0.0176 g (4.3%) of

$RuCl_3$ was dissolved in 5 mL of 1, 2-butanediol separately. After purging the flask 20 min at room temperature, $RuCl_3$ dissolved in 1, 2-butanediol solutions was added, and the mixture was heated up to 100 °C for 30 min. The color of solution was changed from dark blue to black during the heating. When the precursors dissolved completely, the mixture was then heated gradually to 170 °C and then 0.397 mL of trioctylphosphine (TOP) and 0.282 mL of oleic acid (OA) was added to the solution at one minute after temperature was reached 170 °C. The flask was maintained at 170 °C for another 30 min before cooling down to room temperature under a blanket of Ar gas.

6.2.2.2 Synthesis in Solvothermal Reactor

In a typical synthesis, cobalt stearate and nickel stearate (2.07 g, 4.5 mmol), $RuCl_3$ (0.0037 g, 0.018 mmol), Hexadecylamine (0.5810 g, 2.4 mmol) and 60 mL of 1, 2 Butanediol were introduced inside a teflon enclosure (100 mL) with the Ru/Co molar ratio fixed at 0.4%. The teflon enclosure was purged with forming gas (Ar 93% + H_2 7%) for 5 min then sealed. Afterwards, the enclosure was placed in a heated, ultrasonic water bath adjusted to 80 °C. The contents within the enclosure were then mixed for 60 min using the ultrasonic function of the water bath. The temperature of the water bath was maintained at 80 ºC throughout the mixing process. Next, the teflon enclosure was removed from the water bath and fitted within an autoclave reactor. The autoclave reactor was transferred to a furnace and heated from room temperature to 200 °C at a rate of 8 ºC per minute then maintained at 200 ºC for 10 hr. $Co_{95}Ni_5$ nanowires were obtained by adjusting the initial molar ratio of Co stearate and Ni stearate precursors.

6.2.3 Purification and Characterization

After cooling to room temperature, the as-synthesized black product was precipitated when adding ethanol and separated by centrifugation at 6000 rpm for 20 min. Repeated washing step several times with ethanol. X-Ray powder diffraction (XRD) patterns of the samples were recorded with Rigaku Ultima IV diffractometer using Cu-Kα radiation. The transmission electron microscope (TEM) images were recorded using JEOL's 1200EX for observing the crystalline structures and morphologies of nanocrystals operating at 120 kV. The chemical composition of the samples was determined by energy-dispersive X-ray (EDS) spectrometry using Oxford Inca system. Magnetic measurements were carried out at room temperature using Alternating Gradient Magnetometer (AGM) with maximum field of 14 kOe. All the samples for magnetic measurements were prepared by hardening randomly oriented CoNi powders in epoxy.

6.2.4 Results and Discussion

6.2.4.1 Effect of Catalyst Concentration

Figure 6.9 shows TEM images of the as-synthesized CoNi nanocrystals with different morphologies, including nanoparticles dumbbells, nanorods, and nanowires. It is known that $RuCl_3$ as a catalyst plays a vital role in reduction and growth of nanocrystals. In our experiment $RuCl_3$ is used as catalyst to facilitate the reduction of Co^{2+} and Ni^{2+} and the morphologies of the CoNi nanocrystals were controlled by varying the Ru/(Co+Ni) molar ratio. For example, when no $RuCl_3$ was added, only spherical particles with the size of 50-150 nm was produced as seen in Figure 6.9(a). When the molar ratio of Ru/(Co+Ni) was 1%, dumbbell-shaped CoNi nanocrystals with diameter in the range of 15-20 nm and length in the range of 30-50 nm were obtained (see Figure 6.9(b)). This dumbbell-shaped of CoNi could be ascribed to large number of heterogeneous nucleation seeds mainly composed of Ru at the beginning of Co^{2+} and Ni^{2+} reduction and the following fast growth of the CoNi crystals. When the Ru/(Co+Ni) molar ratio was 2.5%, CoNi nanorods with diameter 10-12 nm and the length 50-100 nm were obtained as seen in Figure 6.9(c). Further increase in the molar ratio, CoNi nanowires with diameter about 5-6 nm and the length in the range of 100-200 nm were produced (see Figure 6.9(d)-(e)). The estimated aspect ratio of the CoNi nanocrystals are around 1, 2.2, 6.8 and 30 corresponding to Ru/(Co+Ni) molar ratio of 0.0%, 1.0%, 2.5% and 4.3% respectively. Upon further increasing the molar ratio to up to 5.0%, the diameter of nanowires remained unchanged but the length was decreased to 100 nm (see Figure 6.9(f)), with the aspect ratio around 16.6. It should be noted that the amount of Ru seeds is a key factor on controlling of the morphology of the CoNi nanocrystals under the similar reaction conditions. This observation is similar to the previous report on the effect of adding a nucleating agent on the particles size [157].

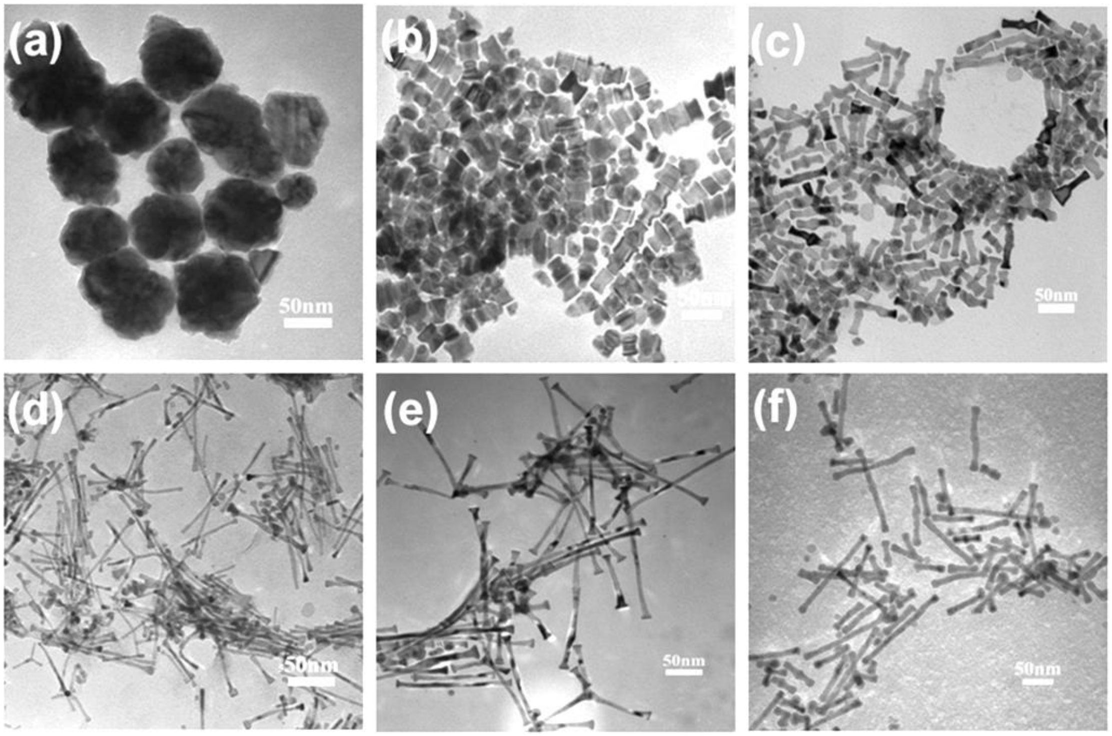

Figure 6.9 TEM images of CoNi nanowires synthesized with different Ru/(Co+Ni) molar ratio in percentage (%): a) 0.0, b) 1.0, c) 2.5, d) 3.5, e) 4.3 and f) 5.0.

Figure 6.10 shows TEM and HRTEM image of the $Co_{95}Ni_5$ nanocrystals with round tip morphology, synthesized using solvothermal process in Teflon lined autoclave reactor. As compared to flask the morphology of nanowires with conical head tip is different when synthesized using solvothermal process. Figure 6.10(a) shows the TEM image of the CoNi nanowires with a length of 200-300 nm and a diameter of about 15 nm were obtained. The high resolution TEM results (Figure 6.10(b)) indicate that each wire is a single crystal with the c-axis (002), or the easy magnetization direction, along the long axis of the wire.

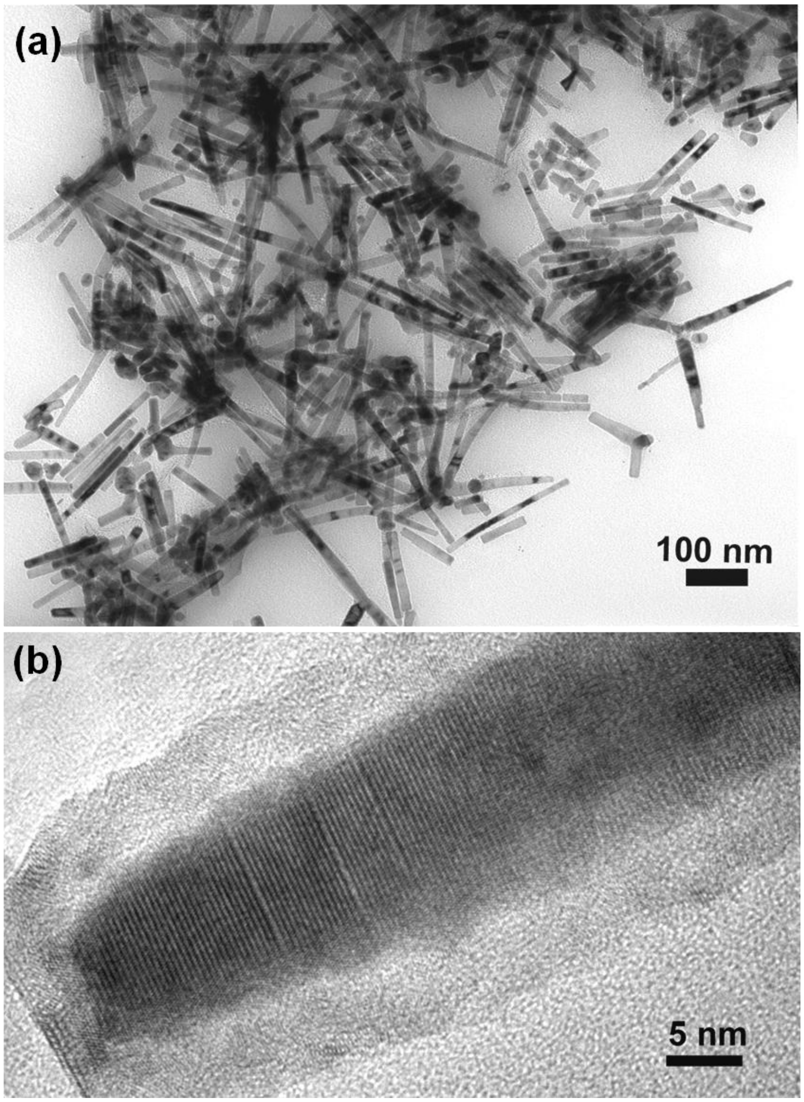

Figure 6.10 TEM analysis of CoNi nanowires synthesized using solvothermal process. (a) Bright-field TEM image of the $Co_{95}Ni_5$ nanowires, and (b) High resolution TEM image of a single nanowire.

6.2.4.2 Growth Mechanism

Relatively abundant Ru nuclei at the initial stage and a high growth rate of CoNi nanocrystals are necessary for producing CoNi nanowires. Based on our experimental observations, we propose a growth mechanism of CoNi nanowire growth with $RuCl_3$ as catalyst as shown in schematic (Figure 6.11). Ru^{3+} is first reduced by 1, 2-butanediol during the early stage of reaction and Ru nanoclusters or nanoparticles with hcp phase are formed. Then, on the basis of the catalysis of $Ru^{(0)}$, Co^{2+} and Ni^{2+} are reduced to $Co^{(0)}$ and $Ni^{(0)}$, and CoNi alloy with hcp phase will heterogeneously nucleate and grow on the surface of the Ru "seeds". So, the amount of $RuCl_3$ controls the nucleation and growth rate. Because the anisotropic hcp crystalline structure of the CoNi intrinsically allows for the anisotropic growth, and excess amount of Co(II) and Ni(II) in the reaction system kinetically controls the preferential growth of CoNi nanowires with hcp phase.

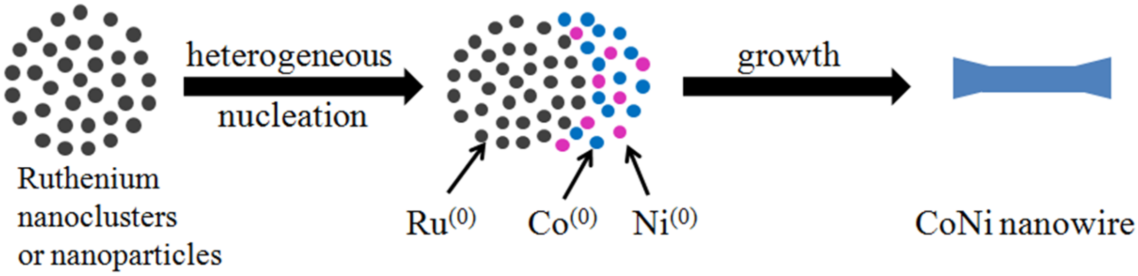

Figure 6.11 Schematic for the growth mechanism of CoNi nanowires.

Figure 6.12 shows the XRD patterns of the CoNi nanocrystals including nanoscale dumbbells, nanorods, and nanowires prepared using different Ru/(Co+Ni) molar ratio. XRD patterns show the diffraction peaks of pure metallic cobalt-nickel hcp phase (Figure 6.12(b)-(g)) except when no $RuCl_3$ was added (Figure 6.12(a)). It should be mentioned that composition of as-prepared CoNi nanocrystals was adjusted at $Co_{80}Ni_{20}$ by controlling initial Co/Ni precursor ratio. EDS performed on the samples showed that the atomic ratio of Co/Ni in the samples is very close to the ratio of the corresponding cations in the starting solution.

In case of CoNi nanocrystals obtained without $RuCl_3$ addition, the intensity of the (002) diffraction was enhanced compared to the hcp peaks indicating presence of mixture of face centered cubic (fcc) Ni phase and the hcp Co phase (as seen in Figure 6.9(a)). For all the diffraction patterns no cobalt oxide or cobalt hydroxide was detected.

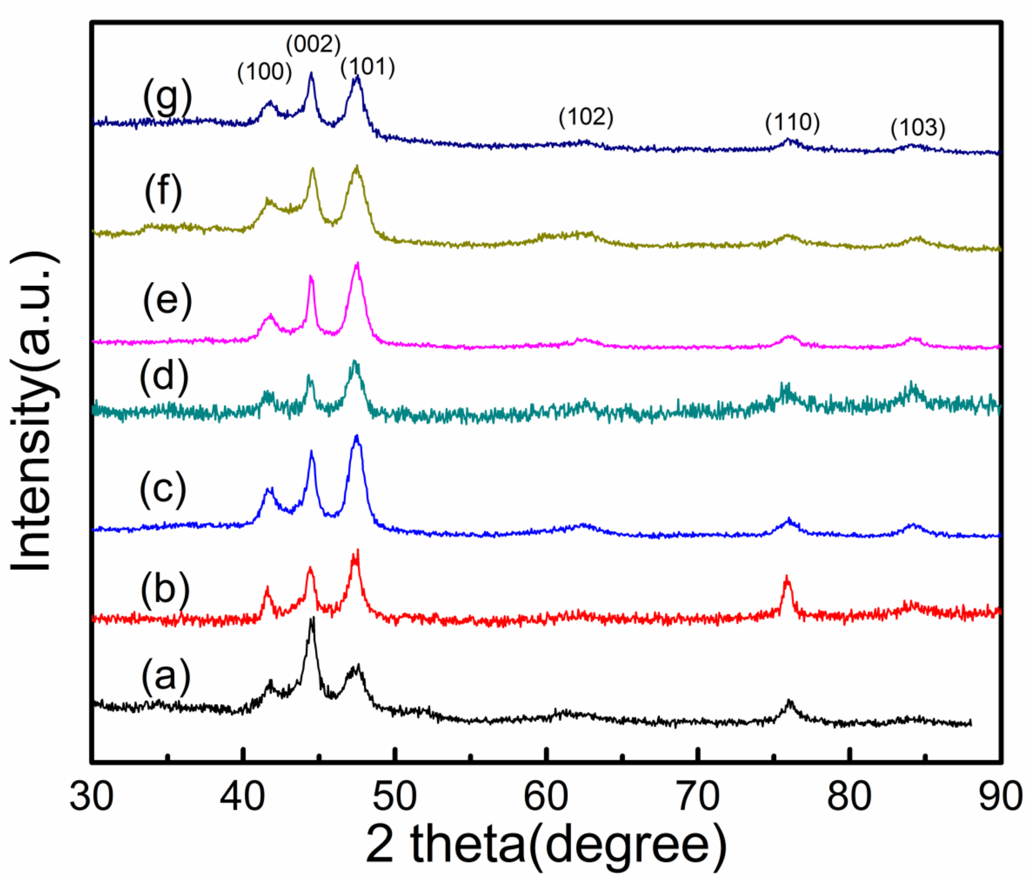

Figure 6.12 XRD of CoNi nanowires synthesized with different Ru/(Co+Ni) molar ratio in percentage (%): a) 0.0, b) 1.0, c) 2.5, d) 3.0, e) 3.5, f) 4.3 and g) 5.0.

Figure 6.13 shows the X-ray diffraction pattern of a randomly oriented $Co_{95}Ni_5$ nanowire assembly and aligned wires along the magnetic field direction synthesized using solvothermal process show the metallic HCP phase. One can see clearly from the XRD pattern that intensity of (002) increases in aligned wires which indicates that their c-axis (002) parallel to the magnetic field direction is along the long axis.

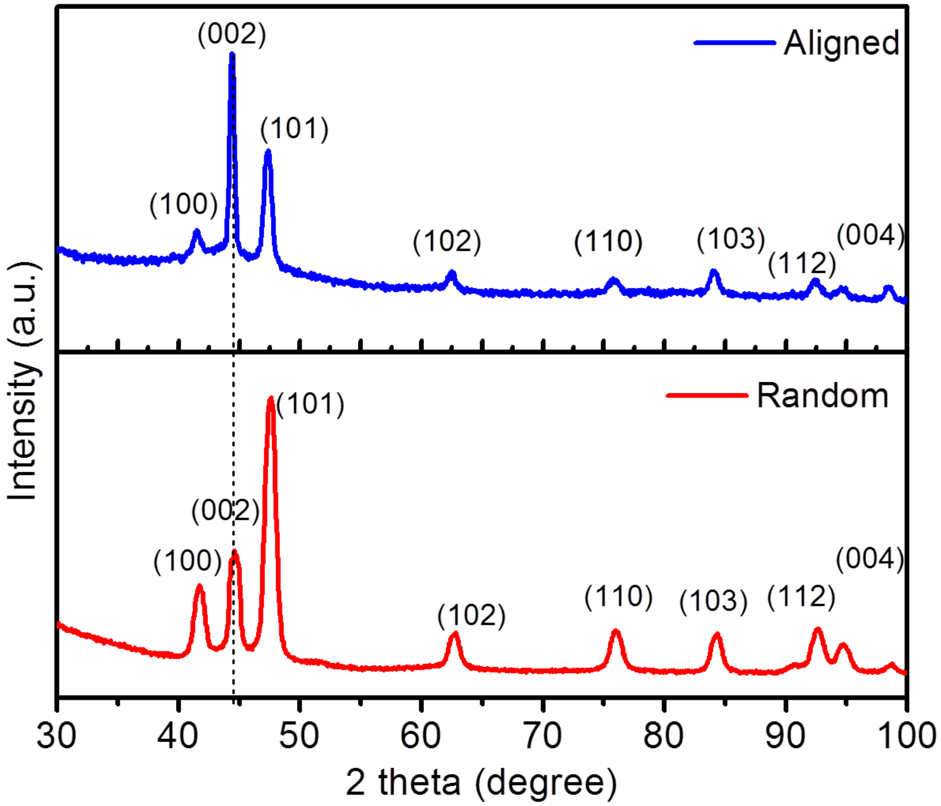

Figure 6.13 XRD of Aligned and Random CoNi nanowires synthesized with solvothermal process.

6.2.4.3 Magnetic Properties

Figure 6.14 shows represented hysteresis loops of randomly oriented as-prepared CoNi nanocrystals. All of the as-prepared CoNi nanocrystals are ferromagnetic at room temperature. It is found that magnetic properties including coercivity and saturation magnetization strongly depend on morphology of the CoNi nanocrystals. While increasing the Ru/(Co +Ni) molar ratio from 0 to 4.3%, both the coercivity and saturation magnetization increase and then decreases with further increasing Ru/(Co+Ni) molar ratio, as shown in Figure 6.15. One can also see from Figure 6.9 that the $RuCl_3$ concentration is vital in controlling the morphology including aspect ratio of CoNi nanocrystals which in turn is also related to magnetic properties of the nanocrystals. The highest coercivity value of 2.9 kOe and the saturation magnetization value of 75 emu/g were obtained when Ru/(Co+Ni) molar ratio of 4.3% was used which led to formation of nanowires with diameter about 5-6 nm and length in the range of 50-200 nm with the highest aspect ratio (~ 30) as seen in Figure 6.14 and Figure 6.15. A remanence to saturation ratio (M_r/M_s) of 0.6 was obtained for the cobalt-nickel nanowire assembly of randomly oriented nanowires. The saturation magnetization measured for the $Co_{80}Ni_{20}$ sample is lower than the value for the bulk alloy (138 emu g^{-1}), which may be related to a surface oxidation.

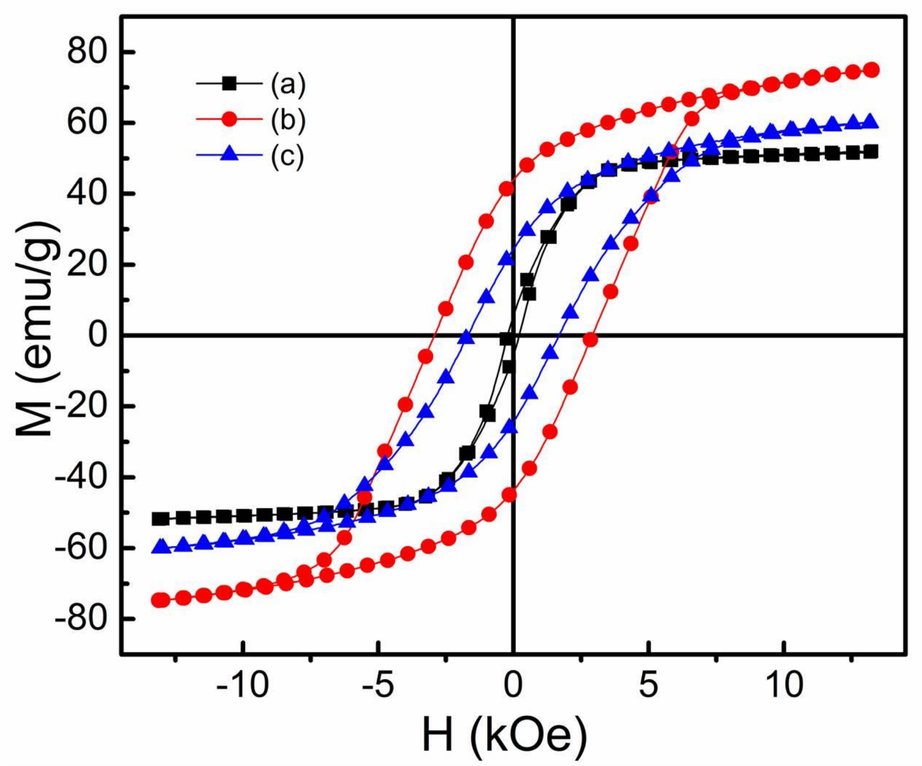

Figure 6.14 Hysteresis loops of CoNi nanowires synthesized with different Ru/(Co+Ni) molar ratio in percentage (%): a) 0.0, b) 4.3, and c) 5.0.

For the $Co_{80}Ni_{20}$ composition, the coercivity and the remanence of the nanoparticles prepared without $RuCl_3$ are much lower than for the wires and nanorods which could be attributed to the shape and purity of phase. The shape of the hysteresis loop may be strongly affected not only by the specific particle surface conditions but also by the magnetic anisotropy [6]. The magnetic anisotropy includes magnetocrystalline anisotropy, shape anisotropy, stress induced anisotropy and exchange anisotropy [6]. The strength of the shape anisotropy depends on the axial ratio c/a of the geometry and magnetization (M). Symmetrically shaped nanoparticles, such as spheres, do not have any net shape anisotropy. However, the synthesized CoNi alloy nanowires and nanorods assemblies with a high aspect ratio have shape anisotropy, which increases the coercivity. Therefore, the different coercivity may be attributed to the changing aspect ratio of the CoNi nanowires/nanorods assemblies.

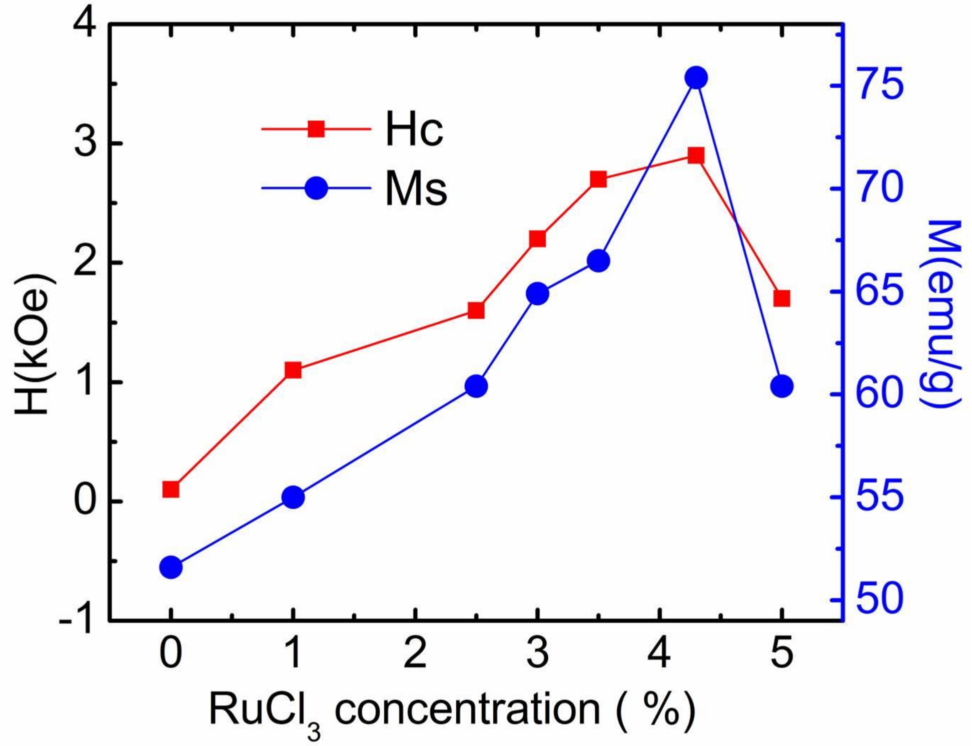

Figure 6.15 Dependence of coercivity and saturation magnetization on RuCl$_3$ concentration.

Figure 6.16 shows the magnetic hysteresis loop at room temperature of a randomly oriented and parallel oriented aligned HCP $Co_{95}Ni_5$ nanowire assembly. Significant coercivity exceeding 4.1 kOe is observed, attributed to the magnetocrystalline anisotropy and the shape anisotropy. The room-temperature coercivity of the magnetically aligned-parallel sample has increased to about 5.1 kOe when the nanowires were aligned curing in epoxy resin using electromagnets under 20 kOe magnetic field (detailed alignment method is described in chapter 7) as shown in Figure 6.16.

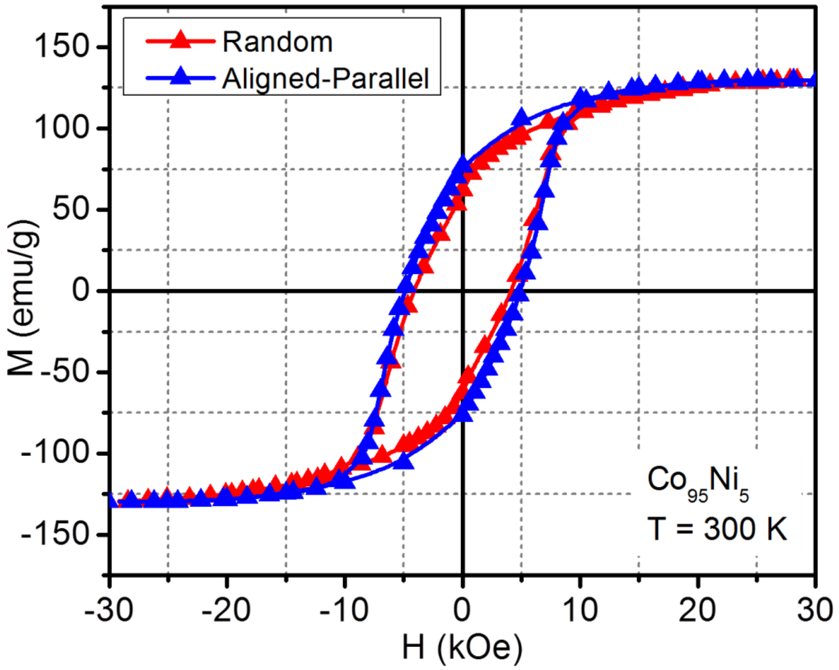

Figure 6.16 Hysteresis loops of randomly oriented and aligned parallel oriented HCP $Co_{95}Ni_5$ nanowires assembly in epoxy at 300 K.

6.2.5 Conclusion

CoNi nanocrystals with different morphologies have been synthesized by varying catalyst $RuCl_3$ concentration via polyol process. The catalyst $RuCl_3$ plays an important role in controlling the aspect ratio of CoNi nanorods and nanowires. The CoNi nanocrystals can be controlled to form nanowires or nanorods with length of 20-200 nm and diameter of 5-20 nm by using different catalyst concentration in the synthesis. The coercivity of the CoNi nanowires depends on the morphology of nanocrystals. The highest coercive force of 2.9 kOe was obtained for 50x200 nm nanowires with $Co_{80}Ni_{20}$ composition. Also, single crystal $Co_{95}Ni_5$ nanowires were synthesized using modified polyol solvothermal process. The high coercive force of 5.1 kOe and saturation magnetization of 129 emu/g was obtained in parallel oriented assembly of the nanowires.

Chapter 7

Synthesis and Characterization of Co Nanowires

7.1 Introduction

In this work, Cobalt nanowires with high aspect ratio have been synthesized via a solvothermal chemical process. The modified polyol process allows synthesizing Co nanowires with different diameters and morphologies. Since the sizes, shapes, and crystalline structures are important factors for its intrinsic properties, sufficient controls on these characteristics inevitably become the key issues in the preparation of Co nanowires. The morphology, crystallographic structure and magnetic properties were characterized by electron microscopy, X-ray diffraction and magnetic measurements. The energy products of the Co nanowires have been assessed by performing magnetic alignment.

7.2 Experimental

$CoCl_2.6H_2O$ (Alfa Aesar, 99.9%), $RuCl_3$ (Aldrich, 45-55 % Ru content), NaOH (Sigma Aldrich, ≥ 97%), 1, 2-Butanediol (Fluka, ≥ 98%), Hexadecylamine (Aldrich, 98%), methanol (VWR, Normapur) and lauric acid (C11H23COO) (Aldrich, 98%) were used without any further purification.

7.2.1 Preparation of Cobalt (II) Laurate

The cobalt (II) laurate, $Co(C_{11}H_{23}COO)_2$, was prepared following a procedure adapted from a previously published synthesis for the cobalt (II) laurate salt [123, 159]. Lauric acid (44.0 mmol) and NaOH (42.0 mmol) was added to 40 ml DI water while being mixed using a mechanical stirrer. The resulted mixture was heated to 60 °C until a clear solution was obtained. At 60 °C, 10 mL of an aqueous solution of 2M $CoCl_2.6H_2O$ (99.9%) (20.0 mmol) was added drop wise to the solution with vigorous mechanical stirring. Afterwards, a purple precipitate formed, and the mixture was stirred and kept at 60 °C for 30 min after the $CoCl_2.6H_2O$ addition. The precipitate was recovered by centrifugation (6000 rpm for 15 min per wash), one time with 45 mL DI water and three times with 45 mL of methanol then dried in an air oven at 60 °C followed by drying under vacuum.

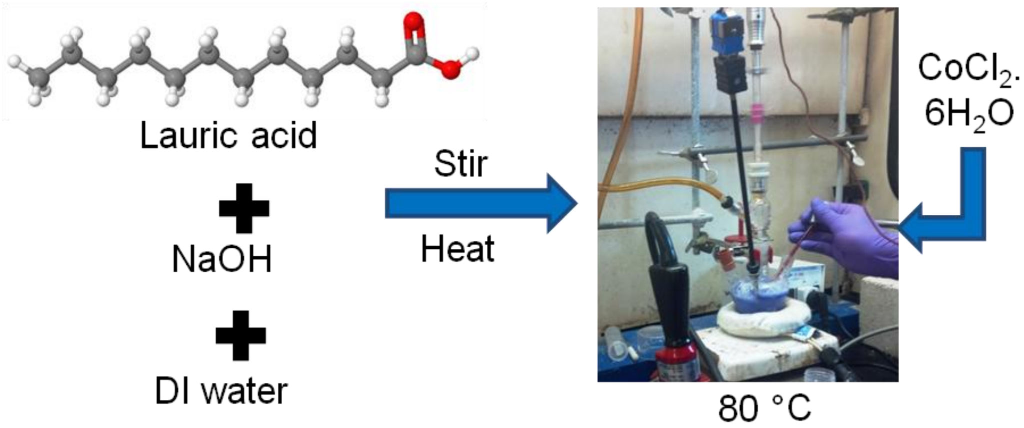

Figure 7.1 Schematic of preparation of cobalt(II) laurate.

7.2.2 Cobalt Nanowires Synthesis

In a typical synthesis, cobalt (II) laurate (2.07 g, 4.5 mmol), $RuCl_3$ (0.0037 g, 0.018 mmol), Hexadecylamine (HDA) (0.5810 g, 2.4 mmol) and 60 mL of 1, 2-Butanediol were introduced inside a teflon enclosure (100 mL) with the Ru/Co molar ratio fixed at 0.4%. The teflon enclosure was purged with forming gas (Ar 93% + H_2 7%) for 5 min then sealed. Afterwards, the enclosure was placed in a heated, ultrasonic water bath adjusted to 80 °C. The contents within the enclosure were then mixed for 60 min using the ultrasonic function of the water bath. The temperature of the water bath was maintained at 80 ºC throughout the mixing process. Next, the teflon enclosure was removed from the water bath and fitted within an autoclave reactor. The autoclave reactor was transferred to a furnace and heated from room temperature to 250 °C at a rate of 8 ºC per minute then maintained at 250 ºC for 75 min. Several reaction parameters such as nature of the metallic precursors, concentration of surfactant, addition of a nucleating agent ($RuCl_3$), and temperature of reaction play an important in the formation of metallic nanowires and allow to control the shape and the size of the nanostructures.

Figure 7.2 Schematic illustration of Co nanowires synthesis process.

7.2.3 Purification and Characterizations

After cooling to room temperature, the black powder consisting of cobalt nanowires was separated from reaction fluid by centrifugation at 6000 rpm for 15 min. The powder was collected then redispersed in 30 ml toluene using an ultrasonic bath. The sample was centrifuged once again at 6000 rpm for 15 min and the toluene discarded. This purification step was repeated two more times. After the purification, cobalt nanowires were dried in a vacuum oven at 50 °C then stored within a glove box with Ar atmosphere.

The transmission electron microscopy (TEM) images were recorded on a JEOL 1200 EX electron microscope at 120 kV. The nanowires samples were prepared evaporating the toluene dispersion on carbon-coated copper grids. High resolution TEM images were obtained with a Hitachi H-9500 high-resolution TEM at 300 kV. Lacey carbon grids were used for HRTEM investigation. Electron holography image of single-cobalt nanowire was recorded digitally at 200 kV in a JEOL JEM-2100F-LM field emission gun TEM equipped with JEOL biprism (0.6 μm diameter, 180° rotation), in a remanent field about 4 Oe. The reconstructed phase image of specimen provides a visual picture of magnetic flux in form of contours.

Powder X-ray diffraction (XRD) spectra were recorded on a Rigaku Ultima IV diffractometer with a Cu K-α wavelength X-ray source. Magnetic measurements of the metallic samples were performed using a Quantum Design MPMS magnetometer (SQUID). Angular dependent measurements were performed using VSM. The sample holder (with an angle indicator) rod is attached to the vibration exciter, and the end of it hangs down in between the pole pieces. The exciter moves the sample up and down at a set frequency. The sample rod can be rotated to 360 degrees for angular measurement of magnetic properties of the sample to the constant magnetic field.

Randomly oriented Co nanowire samples for magnetic characterization were prepared by dispersing then curing in a rapid-set epoxy resin. The other key factor to align the nanowires is the homogeneity of the magnetic field. Aligned Co nanowires were prepared by sonicating the toluene dispersion for 5 min then adding the epoxy into the Co nanowires/toluene dispersion and again sonicating for 2 min. This composite was then poured into a mold and allowed to cure under the external magnetic field of 20 kOe in an electromagnet as shown in Figure 7.3.

Figure 7.3 Electromagnet used for magnetic alignment (left). Photograph of Co nanowires-epoxy composite sample aligned in 20 kOe field (right).

In order to determine the actual magnetization of the as synthesized Co nanowires before hardening into epoxy, inductively coupled plasma mass spectrometry (ICP-MS) was used to quantitatively determine the mass of the Co metal in the nanowire samples. The Co nanowires were initially washed 3 times with toluene and dried in glove box to prevent oxidation. The dried samples were weighed in a vial then digested with 1 ml of concentrated HNO_3 at room temperature. After 1 hour, the solution was diluted down with 1% HNO_3 to the appropriate concentration for the ICP-MS analysis. The results indicate that Co nanowires contain (by weight) 85.4% of Co which was used to calibrate the magnetization values of the nanowires.

7.3 Results and Discussion

7.3.1 Morphology and Structure

The morphology of the cobalt particles prepared by the solvothermal process depends on several parameters: the nature of the cobalt precursor, the surfactant HDA concentration, the heating rate and the addition of a $RuCl_3$. Figure 7.4 shows that the aspect ratio of the Co nanowires can be controlled by varying HDA concentration in reaction and keeping other parameter constant such as ratio of [Ru]/[Co] to 0.4%. From the TEM observation Co nanowires with length of 100 to 150 nm in length and an average diameter of 22 nm were formed when 0.6 mmol of HDA were used as seen in Figure 7.4 (a). When 1.2 mmol of HDA was taken, the length of the wires was increased to 200-250 nm while diameter remains unchanged (Figure 7.4(b)). Further increase in HDA to 2.4 mmol, it led to the formation of Co nanowires with smaller average diameter of 15 nm and about 200 nm in length (Figure 7.4(c)). Upon further increasing HDA to 4.8 mmol, Co nanowires length increases to 400 nm and average diameter decreases to 10 nm (Figure 7.4(d)). The estimated aspect ratio of the Co nanowires are around 5, 10, 6.8 and 40 corresponding to HDA amount of 0.6mmol, 1.2 mmol, 2.4 mmol, 4.8 mmol respectively. It should be noted that the amount of HDA is one of the key factor in controlling the morphology of the Co nanowires under the similar reaction conditions. This observation is similar to the previous report on the effect of adding HDA surfactant on the particles size [160].

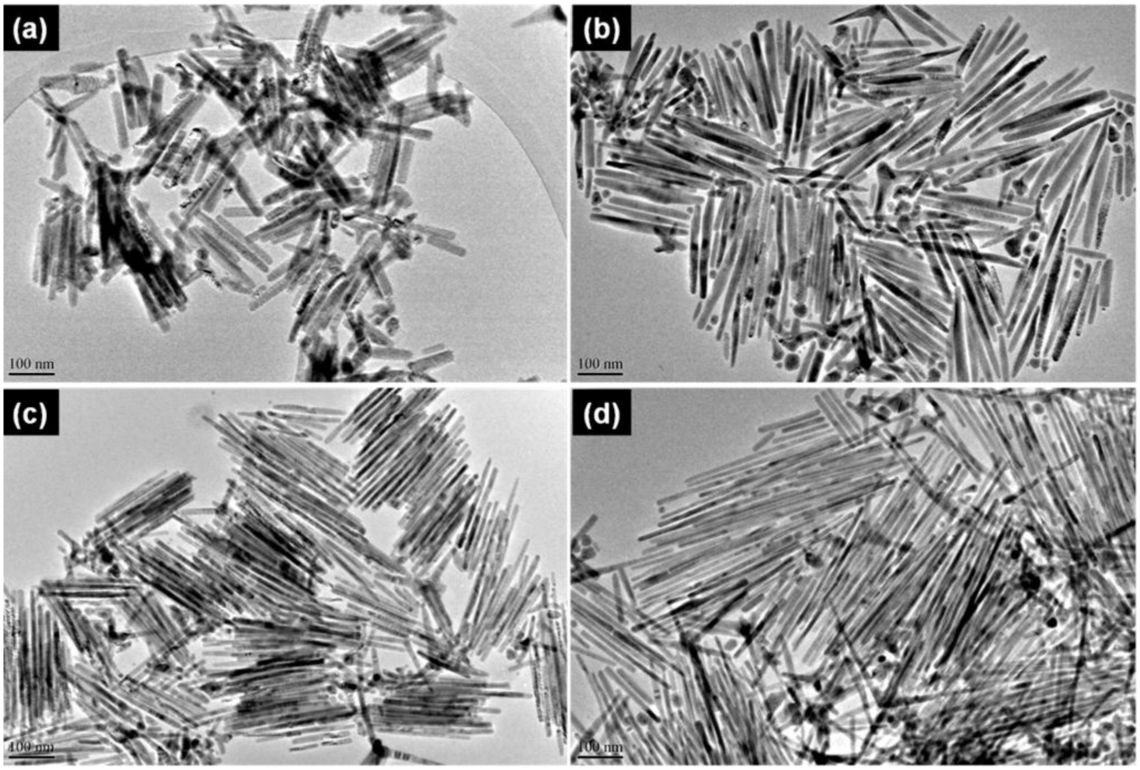

Figure 7.4 Representative TEM images of Co nanowires synthesized with (a) 0.6 mmol HDA, (b) 1.2 mmol HDA, (c) 2.4 mmol HDA, and (d) 4.8 mmol HDA. Scale bar denotes 100 nm.

In this study we report on the possibility of varying the morphology of Co nanowires by playing upon the concentration of the ruthenium chloride ($RuCl_3$) precursor that acts as nucleating agent. Ruthenium chloride was added in the medium to control the nucleation step. An approach consists in varying the relative concentration of the ruthenium precursor, as previously applied in chapter 6 for anisotropic $Co_{80}Ni_{20}$ nanowires where the final shape of the particles is expected to depend on the seed concentration in the medium. The ratio of [Ru]/[Co] was changed by varying Ru concentration in range of 0% which is without adding catalyst, 0.4%, 0.8%, 1.2% and 1.6% in the experiments while using HDA concentration to 2.4 mmol and other parameter constant.

When no catalyst was added into the experiment reduction does not occur at 250 °C for 75 minutes a purple supernatant solution was obtained. From the TEM observation intermediate phase Co nanowires with length of 50-100 nm in length and an average diameter of ~ 16 nm were formed when no catalyst were used as seen in Figure 7.5 (a). When without adding catalyst into the reaction and was maintained at 250 ºC for 150 minutes the solution turned to black indicating the cobalt reduction and co-searchin shape nanowires was observed as seen in Figure 7.5(b). By adding catalysts reduction takes place at 250 °C in 75 minutes. When adding Ru concentration to 0.4%, the isolated nanowires with average length of ~ 200 nm and average diameter of ~ 15 nm was obtained (Figure 7.5(c)). Upon further increasing Ru concentrations to 0.8%, 1.2% and 1.6% mmol, it led to the formation of isolated Co nanowires with almost no change in morphology (Figure 7.5(d-f)). In the general scheme describing the formation of cobalt nanorods by the polyol process, the role of the small amount of ruthenium is to generate in situ small metal seeds for the cobalt growth [161]. The final shape of the particles is expected to depend on the seed concentration in the medium. It should be noted that the amount of $RuCl_3$ is also one of the key factor in achieving isolated Co nanowires under the similar reaction conditions. This observation is similar to the previous report on the effect of adding a nucleating agent on the particles size [157].

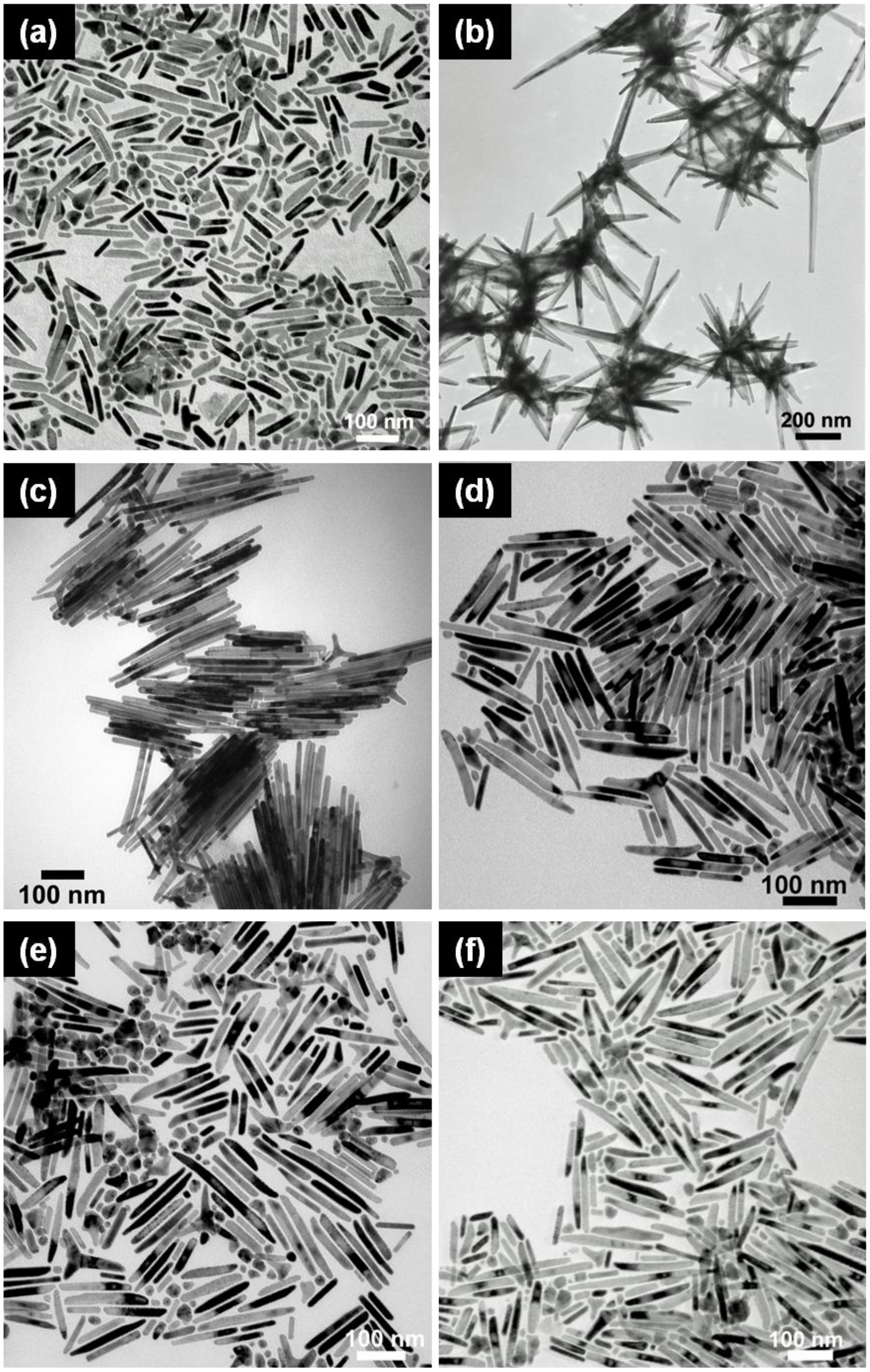

Figure 7.5 Representative TEM images of Co nanowires synthesized with (a)-(b) 0.0%, (c) 0.4%, (d) 0.8%, (e) 1.2%, and (f) 1.6% [Ru]/[Co] molar ratio by varying $RuCl_3$ amount.

Figure 7.6 shows the morphology of the Co nanowires synthesized with optimized condition via a solvothermal chemical process. As shown in Figure 7.6(a)-(b), the Co nanowires using 2.4 mmol HDA, and 0.4 % $RuCl_3$ have cylinder shapes with ellipsoidal tips. The wires have typical size about 200 to 300 nm in length and an average diameter of 15 nm from the TEM observation. The high resolution TEM results (Figure 7.6(c)) indicate that each wire is a single crystal with the c-axis (002), or the easy magnetization direction, along the long axis of the wire. The magnetic holography image (Figure 7.6(d)) reveals a single-domain structure and confirms the magnetization orientation along the long axis. This magnetocrystalline configuration, coupled with the shape of high aspect ratio, favors a coherent rotation of the magnetization process and thus should lead to large coercivity of the nanowire assemblies.

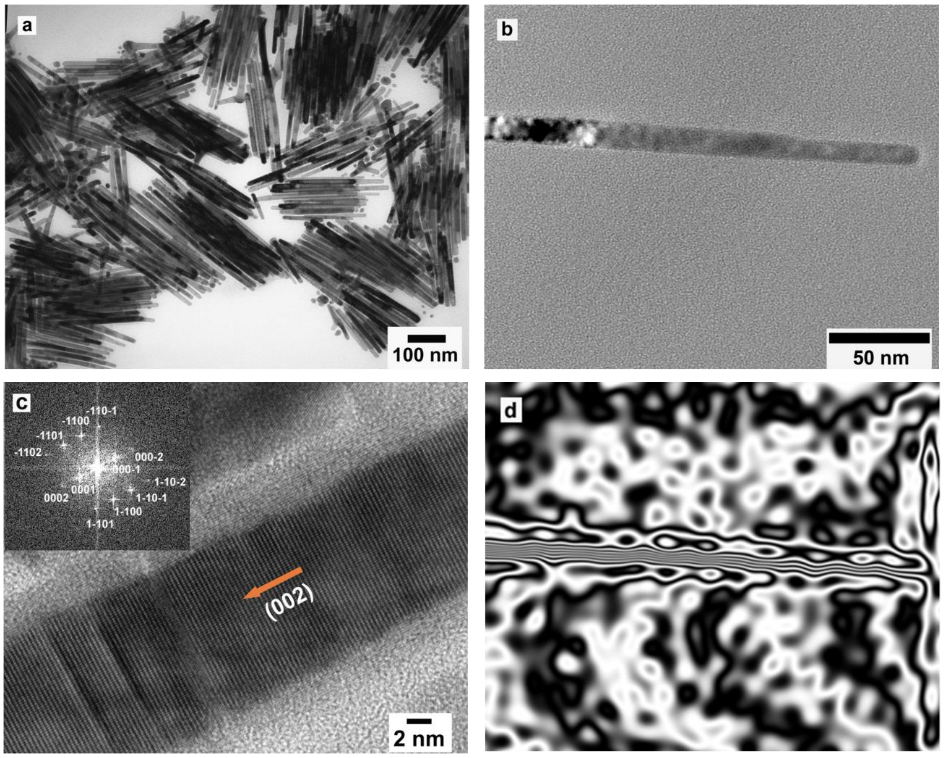

Figure 7.6 (a) Bright-field TEM image of the Co nanowires, (b) Bright-field TEM image of an end-tip single Co nanowire, (c) High resolution TEM image of a single Co nanowire in [11-20] zone axis. Inset the corresponding numerical FFT pattern, and (d) Hologram of a single Co nanowire (with the same magnification as b).

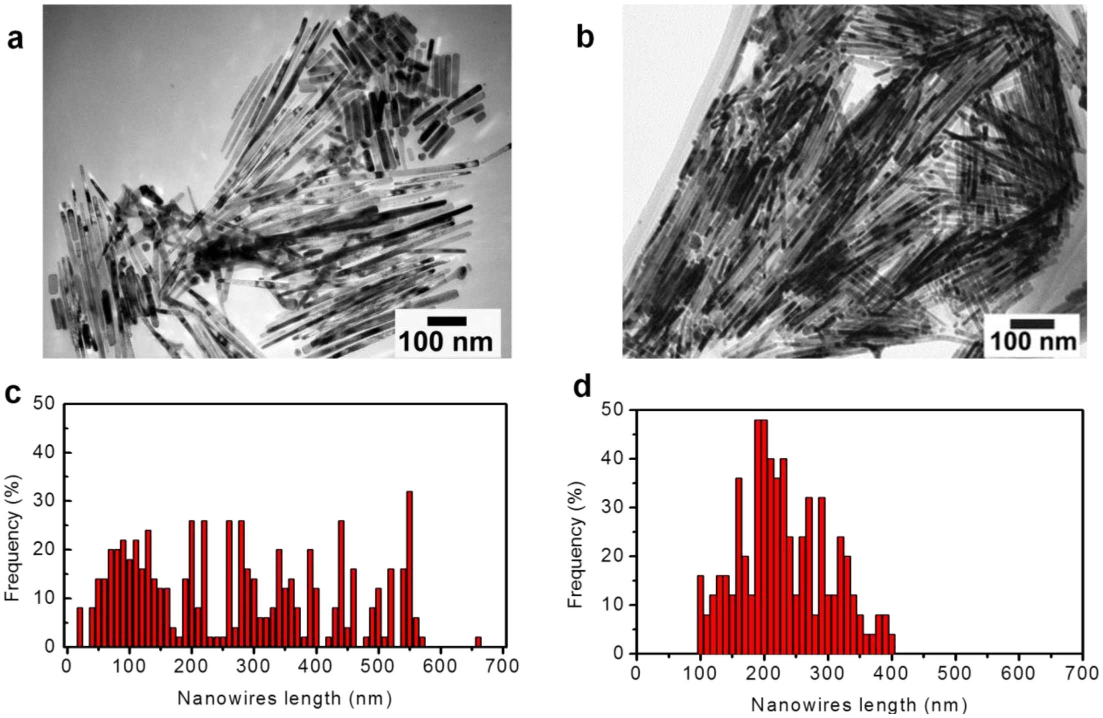

Figure 7.7 TEM images of the Co nanowires corresponding to samples (a) and (b) respectively, (c-d) the histograms of the Co nanowires showing their length distributions of the samples shown in (a) and (b) respectively obtained using statistical analysis of ~ 600 nanowires each.

To further understand the effect of morphology on the coercivity and magnetization hysteresis in the nanowire systems, we compared two groups of samples prepared using same optimized conditions, one with more uniform morphology and one with less uniform morphology. Figure 7.7 shows the details of the two representative samples morphology. Histogram analysis (Figure 7.7(c)-(d)) shows that the major difference in morphology of the two groups of nanowires is the length distribution. The first group has the length range from 10 nm to 600 nm and the second group from 100 nm to 400 nm.

Figure 7.8 HRSEM images shows the effect of the magnetic field alignment of Co nanowires dispersed in a toluene solution without any epoxy resin deposited in the form of the thin layer of Co on a copper foil. It can be observed that the alignment of the wires is visible along axis parallel to the applied field H as shown in Figure 7.8(a). High magnification SEM image of the selected area showed the alignments of parallel nanowires with their long axis parallel to the applied field (Figure 7.8(b)).

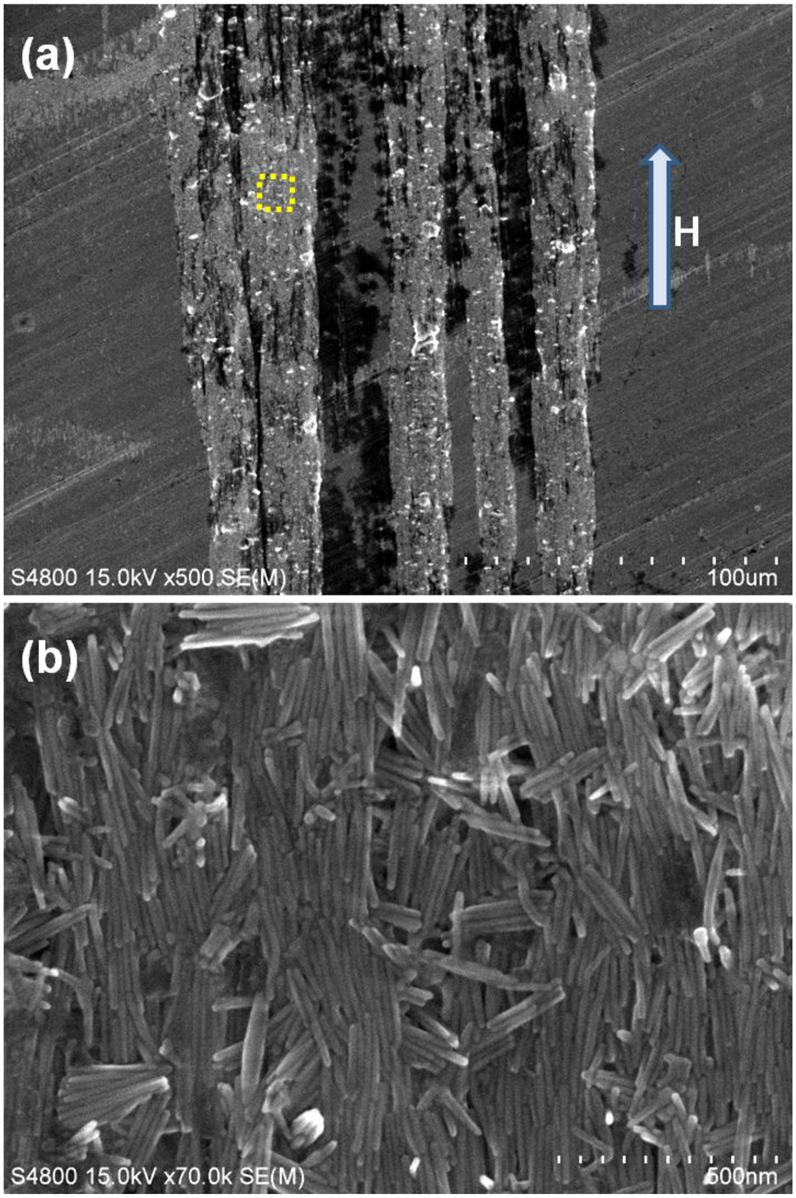

Figure 7.8 (a) High Resolution SEM images of the large area of aligned Co nanowires and (b) High magnification HRSEM image of selected area highlighted by yellow square dashed box of the Co nanowires in (a).

Figure 7.9(a) shows the X-ray diffraction pattern of a randomly oriented Co nanowire assembly show the metallic HCP phase. Figure 7.9(b) is the X-ray diffraction (XRD) pattern of the aligned wires along the magnetic field direction. One can see clearly from the XRD pattern that all the wires were aligned with their c-axis (002) parallel to the magnetic field direction, while all other diffraction peaks disappear.

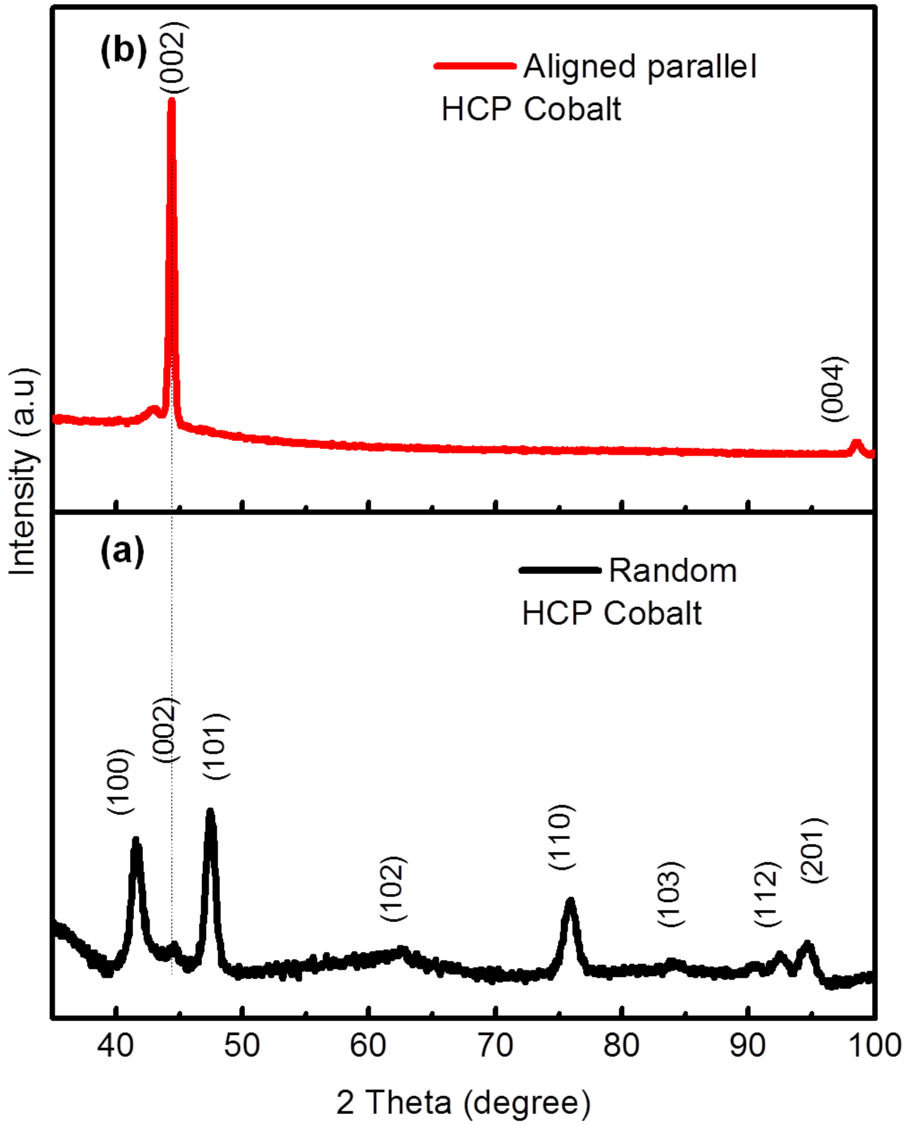

Figure 7.9 (a) X-ray diffraction pattern of randomly oriented assembly of Co nanowires, and (b) parallel oriented aligned Co nanowires in epoxy.

7.3.2 Magnetic Properties

In this section first the magnetic properties of randomly oriented powder and the magnetic properties of the samples with the aligned nanowires at room temperature. Next, compares the magnetization of aligned nanowires with the Stoner-Wohlfarth model which is related to magnetization reversal mode via coherent rotation. Finally, high temperature magnetic properties of Co nanowires were discussed.

7.3.2.1 Room Temperature Magnetic Properties

Figure 7.10 shows the magnetic hysteresis loop at room temperature of a randomly oriented Co nanowire assembly. Significant coercivity exceeding 6.5 kOe is observed, attributed to the magnetocrystalline anisotropy and the shape anisotropy. Although bulk Co material has an anisotropy field of 7.6 kOe, it is practically difficult to obtain a coercivity value of 6.5 kOe for any bulk cobalt materials. Shape anisotropy has played a substantial role in magnetic hardening of the nanowire assembly. Another character of the magnetization loop shown in Figure 7.10 is the remanent magnetization ratio, M_r/M_S (ratio of the remanent magnetization over the saturation magnetization). According to the Stoner-Wohlfarth model [10], in a randomly oriented single-domain particle system, the M_r/M_S ratio is 0.5, which is exactly the situation observed in Figure 7.10. A corresponding parameter that also reflects the degree of the orientation (alignment) of the domains is the “squareness” of the loop in the second quadrant, measured by the ratio of the area covered by the loop curve (demagnetization curve) and the area of the rectangular M_rH_C. As expected, the loop of the randomly oriented system has a modest “squareness” (0.60).

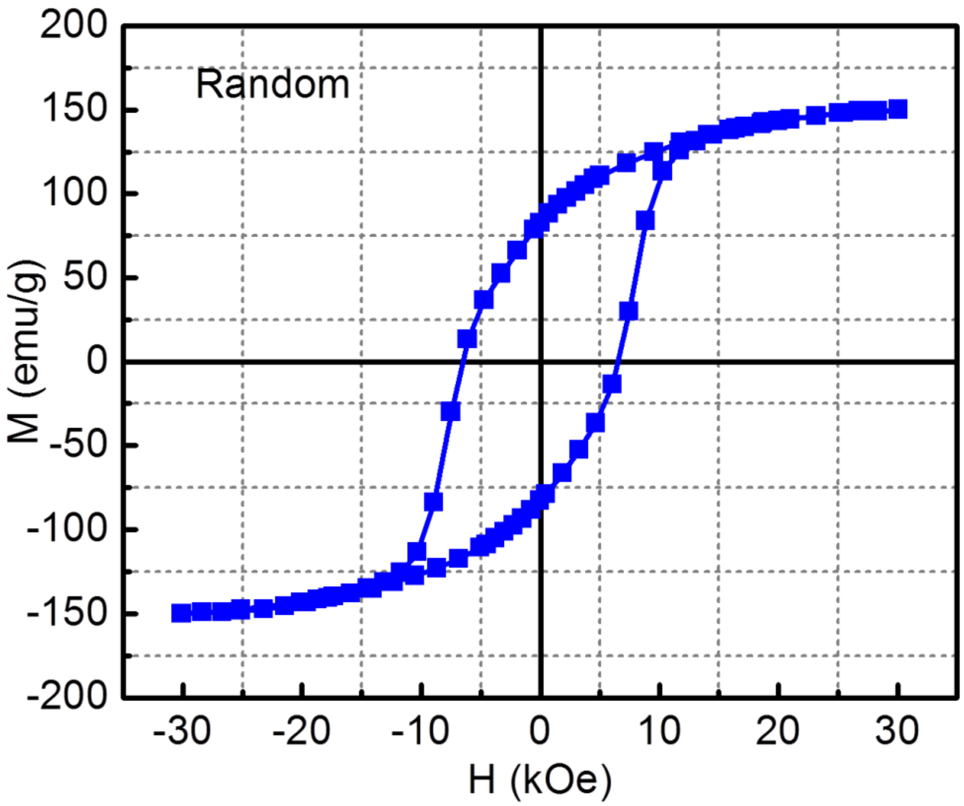

Figure 7.10 Hysteresis loop of a randomly oriented Co nanowires assembly at 300 K.

A change was observed in the hysteresis loop when the nanowires were aligned in a magnetic field (Figure 7.11). As shown in Figure 7.11, the room-temperature coercivity of the magnetically aligned sample has increased to about 12.5 kOe, a record high coercivity value for cobalt material at room temperature, which is nearly double that of the randomly oriented sample (Figure 7.10). The remanent magnetization of the aligned sample also increased greatly, leading to the remanent magnetization ratio M_r/M_S of 0.92, which is an almost doubled value compared to the randomly aligned system (while the saturation magnetization remained unchanged). Consequently, the “squareness” of the loop is significantly increased (to 0.78). This change is a typical Stoner-Wohlfarth behavior of a single-domain particle system upon magnetic alignment [10]. Based on the model, for an ideal single-domain particle system with identical magnetic properties of the particles, the magnetically aligned assemblies will gain coercivity and remanence values twice that of the corresponding systems that are randomly oriented. This “sharp” behavior has been rarely observed in actual hard magnetic materials for the reason that identical single-domain particles are difficult to prepare experimentally. The present results also support the statement that total anisotropy field of the nanowire system is the sum of magnetocrystalline anisotropy field and shape anisotropy field (14.4 kOe in total, at room temperature). From theoretical point of view, the Co nanowire assemblies studied here deserve further systematic investigations.

To further understand the effect of morphology on the coercivity and magnetization hysteresis in the nanowire systems, we compared two groups of samples, one with more uniform morphology and one with less uniform morphology as shown above in Figure 7.7. Magnetization measurements did not show a noticeable difference in coercivity. However one can find an obvious difference in the ‘‘squareness’’ (0.66 and 0.78 respectively). This difference has not been trivial in view of the energy product. In fact, the squareness of the demagnetization curves has the same important effect as the remanent magnetization and coercivity on the energy product. The striking feature is that the small difference in the squareness has led to about a 25% difference in energy product of the two groups of samples. It is understood that in nanostructured ferromagnet systems, morphology uniformity plays an important role in magnetic reversal process.

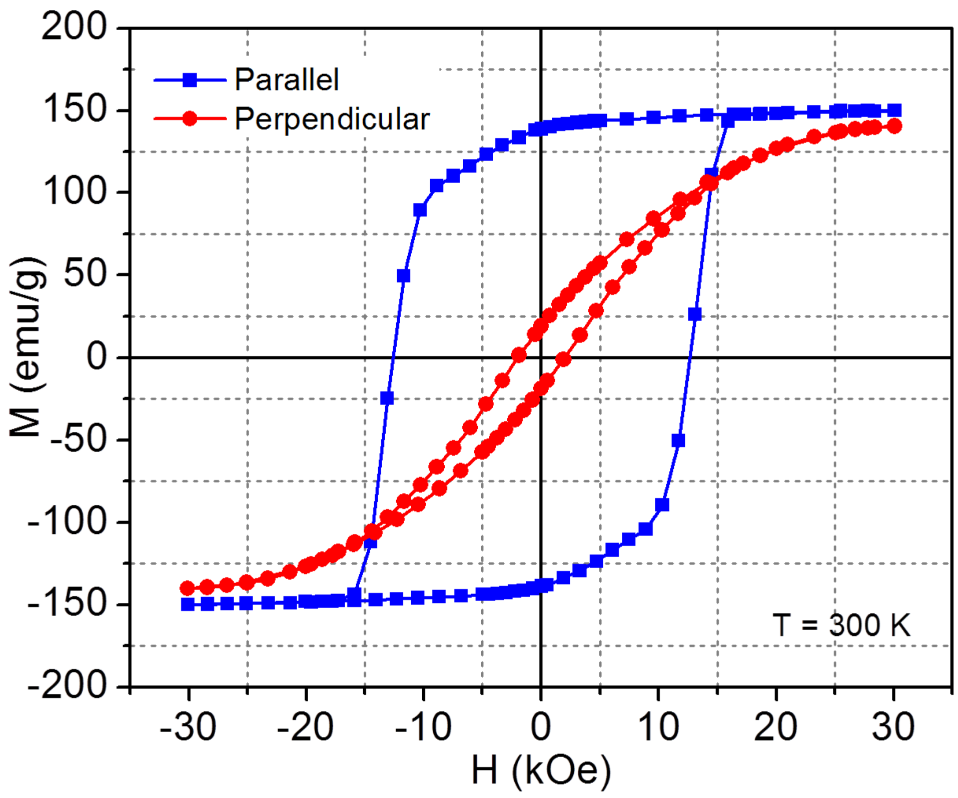

Figure 7.11 Hysteresis loops of aligned Co nanowires in epoxy (along parallel and perpendicular direction) at 300 K.

From an application point of view, the Co nanowire system may be even more intriguing as a potential rare-earth-free high-temperature permanent magnet based on its extremely high Curie temperature and the stability of the Co nanorod morphology up to elevated temperatures revealed by a recent study [125]. In Figure 7.12 the energy product of the aligned nanowires in epoxy is estimated based on a 100 percent volume fraction of closely packed Co nanowires using the theoretical density of 8.92 g/cm^3 containing closely packed nanowires and have obtained a $(BH)_{max}$ value up to 44 MGOe. Although this result does not reflect any effects that can potentially reduce the energy density of a bulk magnet such as packing factor, demagnetization or dipolar interactions [162], the Co nanowires of this type can potentially be ideal building blocks for high performance bonded magnets, consolidated magnets as well as thin film magnets with both isotropic and anisotropic magnetic structures.

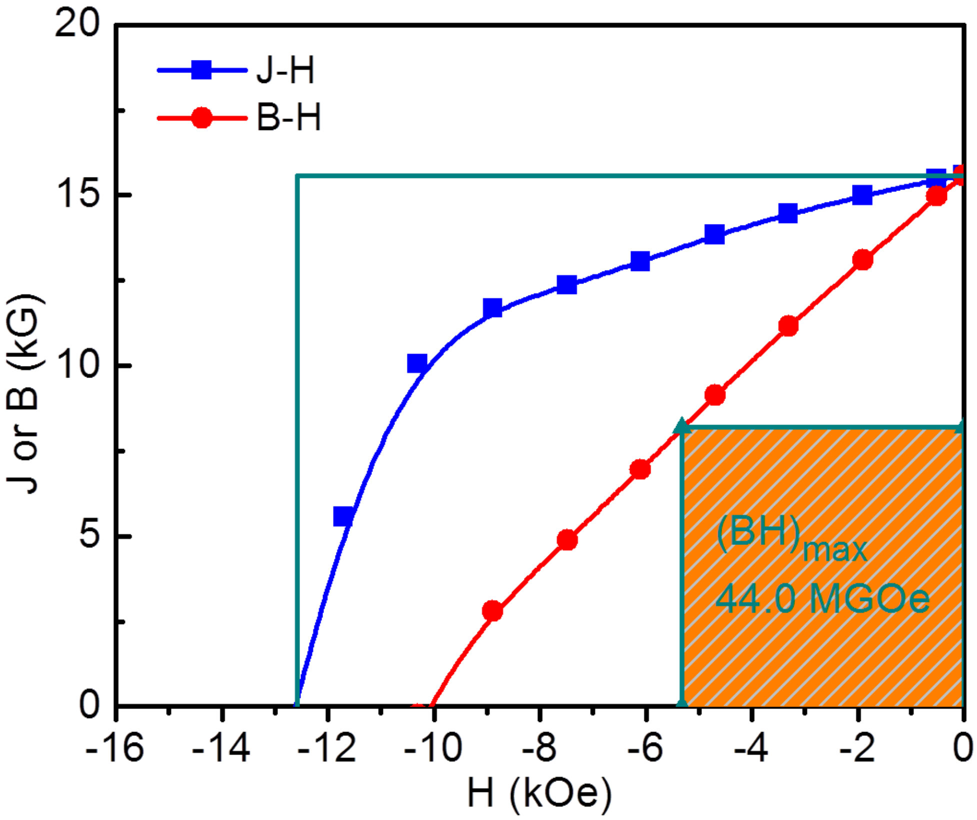

Figure 7.12 Second quadrant B-H curves for the aligned Co nanowires in epoxy (along the easy-axis) at 300 K.

7.3.2.2 Angular Dependence of Coercivity

In the case of a single domain structure, the Stoner-Wohlfarth model (i.e. coherent rotation) has been essentially considered to interpret the magnetization reversal mechanism in nanowire arrays. This classical model assumes the nanowires to be elongated non-interacting particles, where the parallel coercivity, H_C // (applied field parallel to the wire axis) is simply evaluated considering the demagnetizing factors of a prolate spheroid. An alternative way to obtain information about the actual rotational magnetization reversal mechanism is the study of the angular dependence of magnetic properties, particularly of coercivity, H_C, and remanence, M_r.

Recent analytical models [12] have calculated the angular dependence of three main idealized modes of magnetization reversal process: coherent rotation mode (C) with all the spins rotating simultaneously, the curling wall mode (Cur), in which spins reverse progressively via propagation of a vortex-like (curling) domain wall (these two modes have been discussed in Chapter 1), and the transverse wall mode (T) in which spins reverse progressively via propagation of a transverse domain wall.

In order to analyze the actual magnetization reversal processes in the framework of the models discussed above, the full angular dependence of hysteresis loops was measured in a aligned Co nanowires sample in epoxy by sample holder rotation technique in head assembly with constant magnetic field using VSM. The experimental coercivity can be compared with the expected evolution assuming possible coherent reversal mode. It has shown that the magnetic properties of Co nanowire arrays are strongly dependent upon the direction of crystalline structure and c-axis (002) of hcp phase. To obtain a good agreement with experiments the magnetocrystalline anisotropy with an anisotropy constant of 5.0 x 10^5 J/m^3, which corresponds to a parallel easy axis (002), is considered. Figures 7.13 illustrates the experimental and fitting curves for aligned nanowire arrays (D ~ 15 nm, L ~ 200 nm) with textures in the (002).

The classical angular dependence of the nucleation field for a coherent magnetization reversal was calculated by Stoner-Wohlfarth, a general expression for the $H^C(\alpha)$, of a reversed domain can be established as given in equation (1.27). For the Co wires with the HCP structure and the c-axis parallel to the wire long axis a theoretical total anisotropy field up to 14.4 kOe at room temperature is expected provided that the Stoner-Wohlfarth model applies. Regarding the lack of perfect fitting of coercivity for angles close to 0º and 90º, it is due to the limitations of the model as well as the fact that it does not consider interactions with surrounding wires and also misalignment of nanowires.

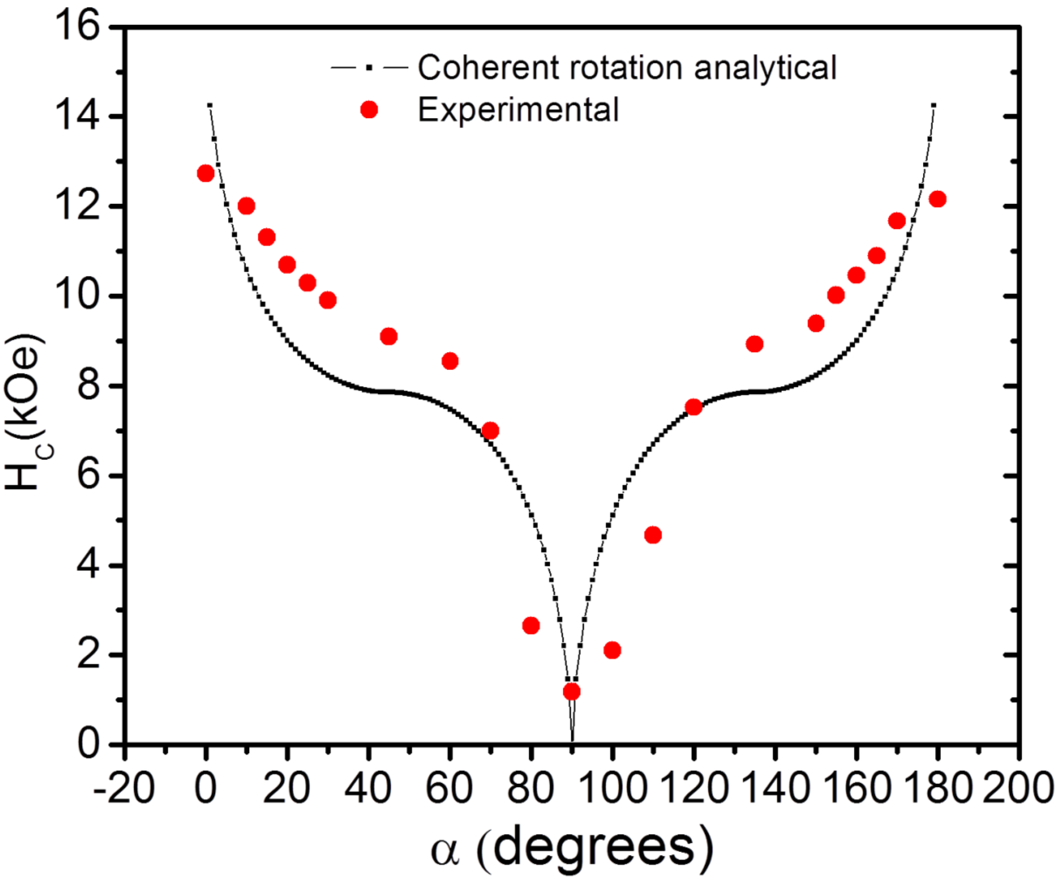

Figure 7.13 Experimental (red circles) and calculated angular dependence of coercivity for arrays of ~ 15 nm diameter and ~ 200 nm length Co nanowires with c-axis (002) hcp-phase texture.

7.3.2.3 High Temperature Magnetic Properties

Three sets of samples were prepared for high temperature magnetic measurements. Sample 1: deposition of randomly oriented magnetic nanowires on silicon without applying external magnetic field. Sample 2: a few drops of a Co nanowires suspension in toluene were deposited on copper foil and the toluene was removed by evaporation under the application of an external magnetic field. Sample 3: Aligned Co nanowires-epoxy composites. The high temperature magnetic measurement was performed using PPMS with VSM option. Before measurement both samples on VSM holder were covered with high temperature cement. The cobalt nanowires are ferromagnetic at room temperature with coercivity of 6.5 kOe, 7.4 kOe and 12.2 kOe for the samples 1, 2, and 3 respectively. The difference of H_C is essentially due to a alignment of the particles. The magnetic characteristics have been improved due to orientation of the nanowires in the sample 3 which increases coercivity compared to those of partially aligned and non-oriented nanowires in sample 2 and 1. As shown in Figure 7. 14 and 7.15 for sample 1 and sample 2, the hysteresis loops measured from temperature range 305 K - 650 K. As shown in Figure 7.16 for sample 3, the hysteresis loops are measured for a temperature range 305 K - 400 K due to thermal decomposition limit of epoxy resin.

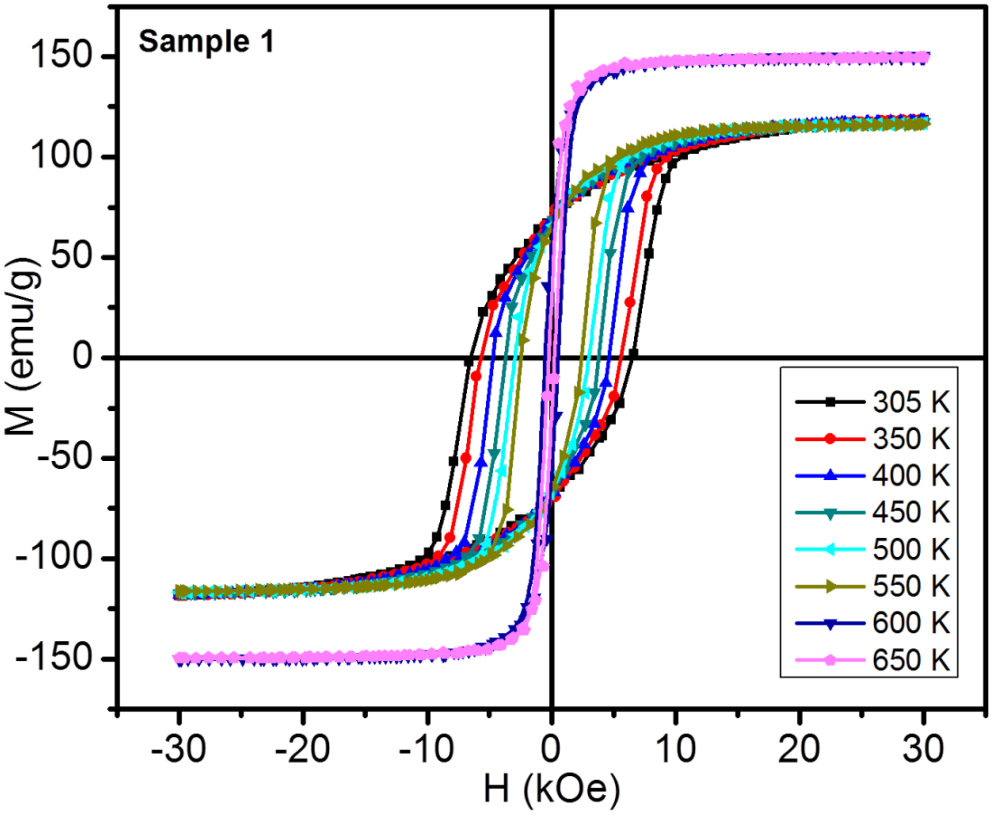

Figure 7.14 Hysteresis loops of a randomly oriented Co nanowire assembly measured at range of 305 K - 650 K.

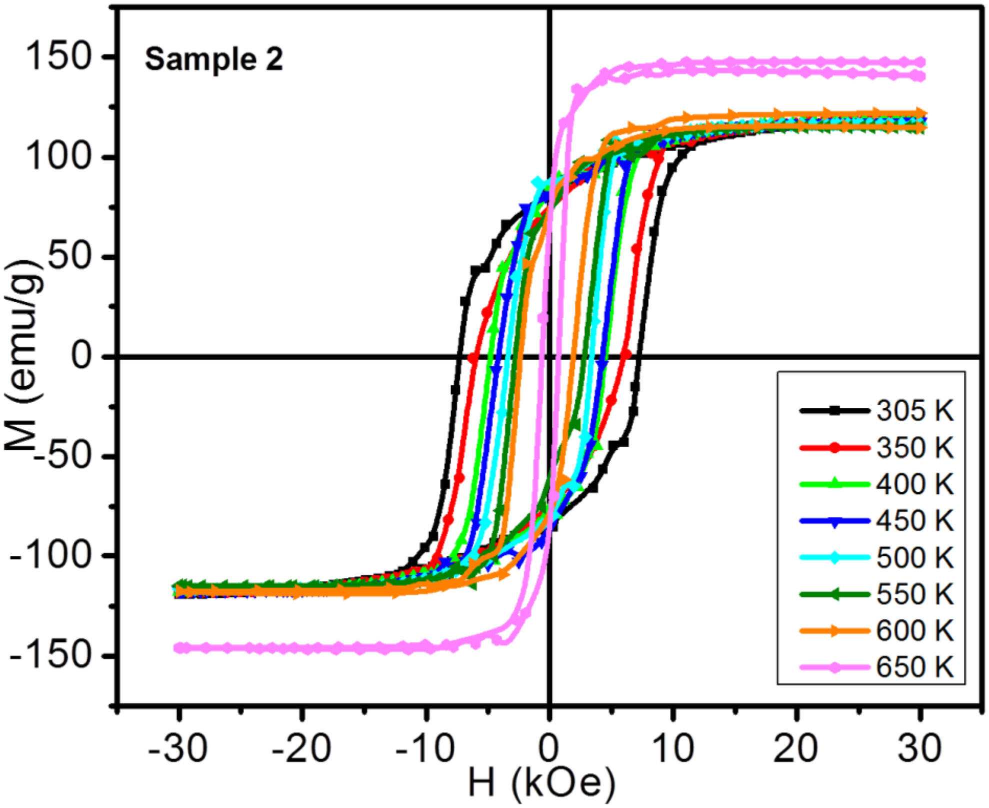

Figure 7.15 Hysteresis loops of a partially oriented Co nanowire assembly measured at range of 305 K - 650 K.

The coercivity, H_C of the sample 1 and sample 2 follows the same linear behavior (decreases) over the temperature range 305 K-500 K. This dependence can be accounted due to the temperature dependence of magnetocrystalline anisotropy. Temperature dependence variation of H_C for sample 1 and sample 2 is shown in Figure 7.17(a). At 500 K, 46% of the room temperature coercivity is preserved corresponding to the shape anisotropy contribution only. The magneto-crystalline anisotropy of single crystalline cobalt is usually described by an anisotropy energy as equation 2.16 in section 2.1.3.2 at 300K with K_1 and K_2 for HCP Co given in Table 2-1. The value of K_1 changes sign at 520 K and K_2 decreases to 0.4×10^5 J/m^3 at 600 K [163]. The coercivity of sample 3 at 350 K decreases to 9.9 kOe from 12.2 kOe at 305 K. At 400 K, H_C decreases to 7.5 kOe in sample 3 as shown in Figure 7.16.

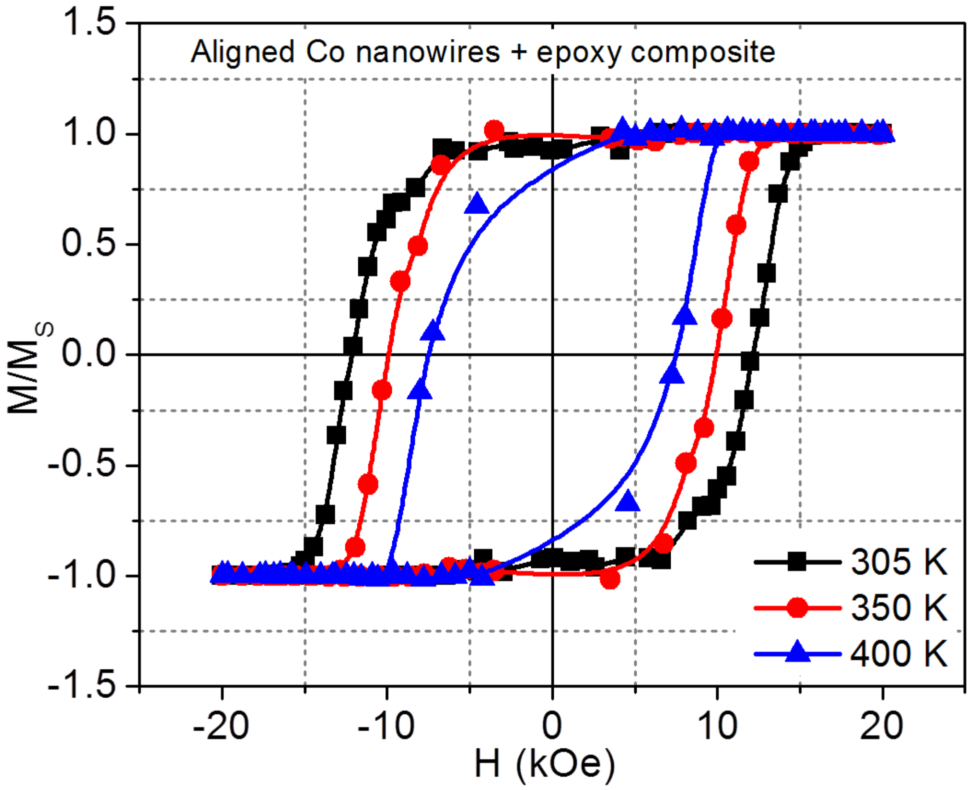

Figure 7.16 Hysteresis loops of a oriented Co nanowire assembly in epoxy measured at range of 305 K - 400 K.

The temperature dependence of the saturation magnetization is presented in Figure 7.17(a). The saturation magnetization M_S of sample 1 and 2 is 118 emu/g. Such a low value (compared to the bulk value of 165 emu/g) is due to the surface oxidation of the wires and by the remaining organic matter. In the case of sample 2, the saturation magnetization M_S is stable up to 600 K; M_S decreases by less than 3% from 305 to 600 K. At 650 K, a jump of the magnetization is observed corresponding to an increase of 22% with respect to the room temperature magnetization value. For the sample 1, the saturation magnetization of the cobalt nanowires varies only slightly up to 550 K but also a jump of the magnetization is observed at 600 K for sample 1 and at 650 K for Sample 2. The magnetization jump can be explained as decomposition of remaining metal-organics at the surfaces of the Co nanowires that reduces the cobalt-oxide layer and causes the more of added metallic cobalt. This phenomenon was also observed by K. Ait Atmane et al. [125]. In the case of sample 1, sintering of the wires interferes with the intrinsic magnetic properties of the Co nanowires. On the other hand, in the case of sample 2, the wires are structurally stable in shape at least up to 600 K. The value of the coercivity at 550 K is 2.5 kOe in sample 1 and 2.4 kOe at 600 K in sample 2 as seen in Figure 7.17(b) which thus corresponds to the contribution of the shape anisotropy. Coercivity as a function of temperature dependence for sample 1 and 2 is listed in Table 7-1.

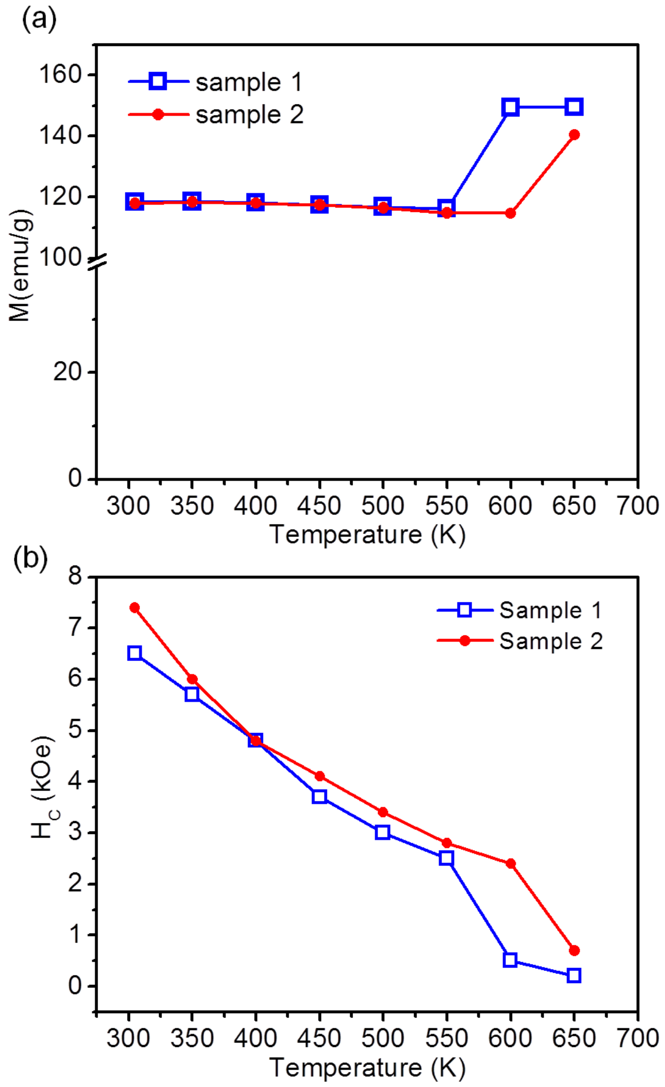

Figure 7.17 (a) M_S, and (b) H_C as a function of temperature as for sample 1 and sample 2.

Table 7-1 Coercivity as a function of temperature dependence.

Temperature (K)	H_C (kOe) **Sample 1**	H_C (kOe) **Sample 2**
305	6.5	7.4
350	5.7	6.0
400	4.8	4.8
450	3.7	4.1
500	3.0	3.4
550	2.5	2.8
600	0.5	2.4
650	0.2	0.7

With respect to high temperature magnetic properties, the present study shows that the temperature dependence of the Co magneto-crystalline anisotropy (K_{MC}) is a real limitation. K_{MC} not only vanishes around 550 K but becomes negative above this temperature, which as a consequence, leads to magnetic properties which are very sensitive to the temperature. Nevertheless, the materials are rather resilient to high temperatures up to 600 K and are competitive with the other existing types of permanent magnetic materials. Rare earth based NdFeB magnets cannot be operated at temperature above 400 K because of irreversible losses. Co nanowires have similar temperature coefficient for H_C as $SmCo_5$ and can be operated at same elevated temperature up to 523 K.

7.4 Conclusions

In summary, record high room-temperature coercivity has been developed in nanocrystalline Co metal material with high aspect ratio, synthesized through a carefully controlled chemical solvothermal process, which resulted in high energy product in the material.

Shape anisotropy provides the basis of the enhanced coercivity, the orientation and uniformity of the single-domain nanocrystals are essential for achieving high magnetic energy density. Present experiments show that Co nanowires with diameters of ~ 15 nm and an average length of 200 nm have a record high coercivity of 12.5 kOe at room temperature, leading to an energy product of ~ 44 MGOe. In this chapter, analytical models describing the magnetization reversal of the Co nanowires was presented. These models are based on the demagnetized factor approximation and on the supposition of coherent reversal inside nanowire. Despite multiple limitations, these models are widely used in the literature and may provide valuable information about the nature of the magnetization reversal. High temperature stability of Co nanowires at 550 K showed that 38% of the room temperature coercivity is preserved. This value corresponds to the contribution of the shape anisotropy to the global anisotropy since at 550 K the magnetocrystalline contribution has vanished. Ferromagnetic nanowires of this type are ideal building blocks for future bonded, consolidated and thin film magnets with high energy density and high thermal stability.

Chapter 8

Exchange Bias in Oxidized Co Nanowires

8.1 Introduction

Magnetic properties of metallic nanowires may be strongly affected by their oxidation. Indeed when they get in contact with air, they may oxidize until passivation occurs and thus be covered with a finite sized shell of oxide. The consequences are twofold: (i) the moment of the objects will be reduced due to a decrease of the magnetic volume and (ii) the hysteresis cycle can be biased due to the Exchange Bias effect (see Section 1.9). Exchange-bias has been found in a variety of different systems with FM/AFM interfaces, including core-shell nanoparticles [164-166], thin film systems [167-169, 27], and other lithographed nanostructures [170-172]. Nevertheless, only a few reports were found on the EB coupling in core-shell nanowires [173-175]. In the case of core-shell nanowires, EB arises due to the interfacial exchange coupling between FM core/AFM shell. An important aspect is the directional properties of EB. This chapter focuses on the consequences of the exchange bias on the magnetic properties of Co/CoO core-shell nanowires. In particular, temperature and angle dependent magnetic measurements were then investigated to study the EB and magnetization reversal phenomenon. The angular dependence of H_{EB} and the coercivity H_C was used to demonstrate that in general H_{EB} does not have simple $\cos \theta$ dependence while having its maxima at $\theta = 30°$. H_{EB} is strongly affected by the spin orientations at the interface between the FM and AFM. We attribute this behavior to the non collinear spin orientations at the interface of magnetic easy axes of the FM core and the AFM shell. The results of angular dependence measurements of H_C show that the magnetization reversal mechanism can be considered within the framework of the coherent rotation model. The temperature dependence of the H_C was found to have an oscillatory behavior.

8.2 Experimental

Single crystalline Co nanowires with a diameter of ~ 15nm and length of ~ 200 nm have been synthesized as describe in section 7.2 by a solvothermal method. The as-synthesized Co nanowires are susceptible to oxidation when exposed to air. In order to perform magnetic characterizations, the nanowires are collected by centrifugation, washed several times with toluene thus it form shells of native oxides (CoO) on the Co nanowire surface which can be excellent sample for angular dependence investigation of exchange bias in nanostructures.

The transmission electron microscopy (TEM) images were recorded on a JEOL 1200 EX electron microscope at an accelerating voltage of 120 kV. The nanowires samples were prepared evaporating the toluene dispersion on carbon-coated copper grids. High resolution TEM images were obtained with a Hitachi H-9500 high-resolution TEM with an accelerating voltage of 300 kV. Lacey carbon grids were used for HRTEM investigation. For Raman measurements spectra were obtained at room temperature using a Thermo Fisher Scientific DXR Raman microscope equipped with a DXR 532 nm excitation laser and high resolution grating for 532 nm laser. Dried powder sample were put under a 50× objective (Olympus BH-2 microscope), which allows the laser beam to focus on a small selected area of the sample surface, and the backscattered Raman signal was collected. The magnetic properties of the core-shell nanowires were measured using a quantum design magnetic properties measurement system (MPMS). The aligned sample was prepared by hardening Co nanowires in epoxy resin which has been described in detail in section 7.2.3 of chapter 7. For the angular dependence of magnetic property the aligned Co nanowires sample was field cooled from 300 to 10 K in 50 kOe along the long axis of the nanowires and measured at 10 K and 300 K (RT) by increasing a temperature, under a maximum field of 30 kOe applied. The sample was then removed at 300 K and rotated to a new angle θ, and the field cooling procedure and measurements were repeated.

8.3 Results and Discussion

8.3.1 Morphology and Structure

Figure 8.1(a) shows the transmission electron microscopy (TEM) image of an assembly of Co nanowires with diameter of ~ 15 nm and length of ~ 200 nm. The electron diffraction pattern from a larger sample area (Figure 8.1(b)) shows well defined rings corresponding to the highly crystalline Co core and CoO shell.

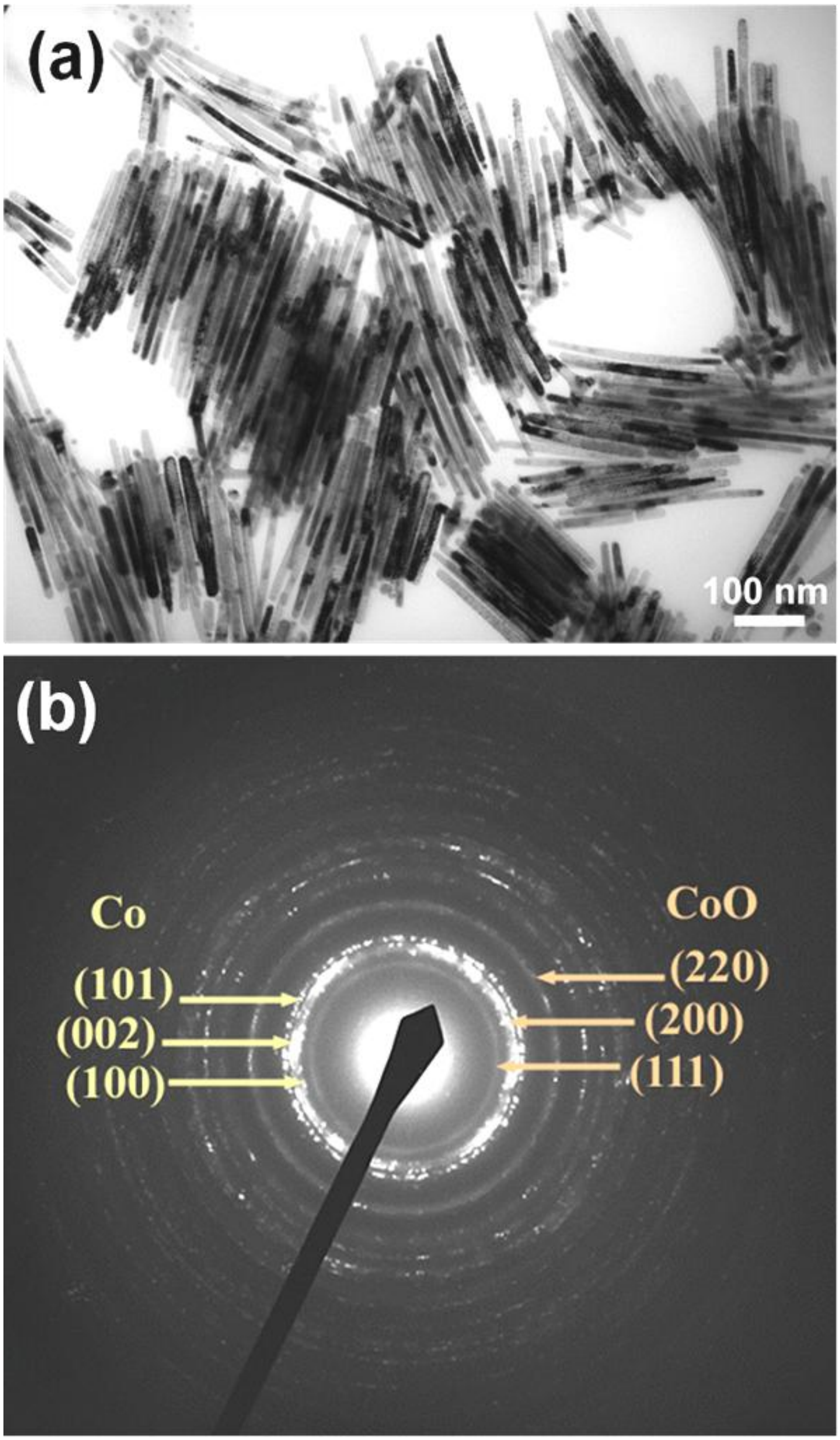

Figure 8.1 (a) Bright-field TEM image, and (b) selected area electron diffraction pattern of Co/CoO core-shell nanowires.

The high resolution transmission electron microscopy (HRTEM) image (Figure 8.2(a)) of a nanowire reveals that the core is single crystalline with the c-axis (002) or the easy magnetization axis of hcp cobalt, oriented along the long axis of the nanowire. By careful observation it can also be seen that there is variation in contrast along the edge of the nanowire, which provides some insight into the formation of CoO shell. The thin oxide shell has a diameter of ~ 1.5 nm and is composed of randomly oriented small crystallites. The representative Fast Fourier Transform (FFT) pattern of the HRTEM image shown in Figure 8.2(b) consists of diffraction spots from two sets of reflections, hcp Co core and fcc CoO shell and they are overlapped. Diffraction spots encircled in yellow correspond to the hcp core viewed along the [11-20] zone axis. The orange encircled diffraction spots are from a fcc CoO structure imaged along the [110] zone axis. The FFT pattern analysis yield lattice constants of Co, a = 0.251 nm, c = 0.407 nm and CoO, a = 0.426 nm in agreement to reported literature [173]. Therefore, we conclude that the core-shell structure arises from a metallic hcp Co core covered with a 1-2 nm polycrystalline fcc CoO shell.

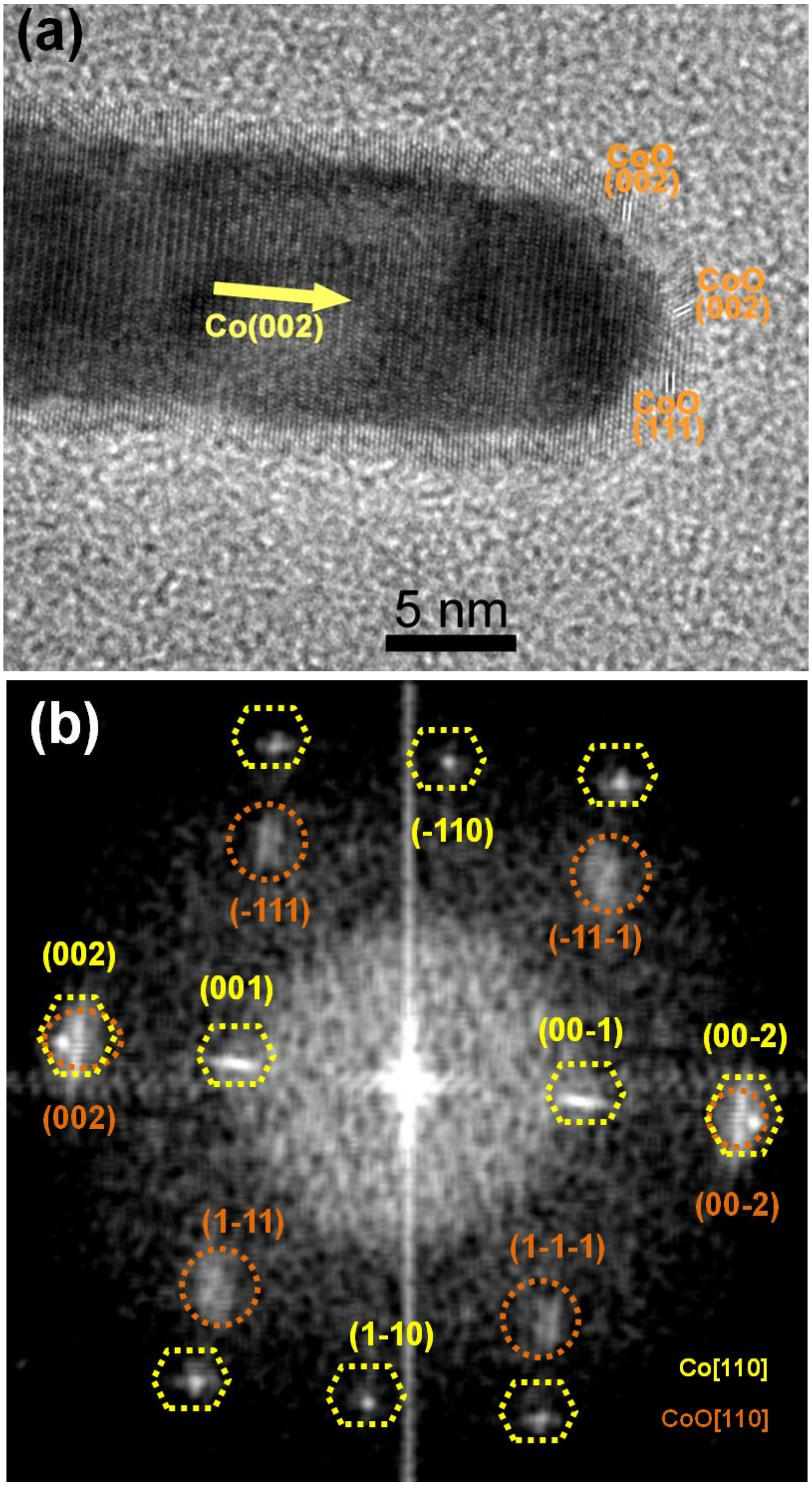

Figure 8.2 (a) HRTEM image, and (b) corresponding numerical FFT pattern of Co/CoO core-shell nanowires.

It is well known that Raman spectroscopy is one of the most effective ways to observe nanostructured CoO phase. Raman-scattering spectra collected from the powder sample (Figure 8.3) show first-order peaks, at ~ 474,~ 515, ~ 612 and ~ 681 cm^{-1}, with mode symmetry assignments to A_{1g}, F_{2g}, and E_g, respectively. The spectra confirm the presence of oxidized cobalt in the form of CoO [176, 177]. It should be noted that Co_3O_4 phase was not found from Raman spectra.

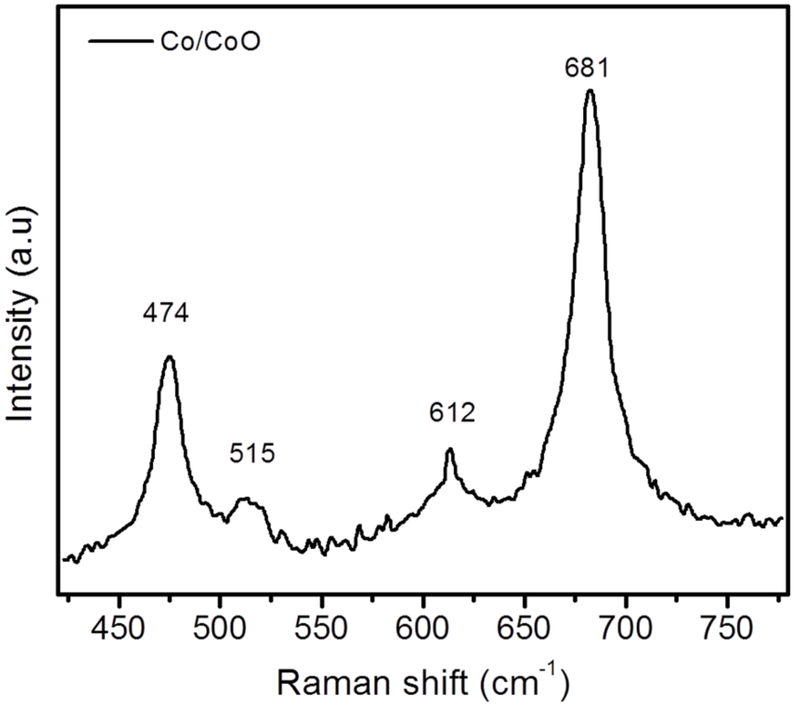

Figure 8.3 Raman spectra of Co/CoO core-shell nanowires.

8.3.2 Magnetic Properties

8.3.2.1 Low Temperature Magnetic Properties

The magnetic properties of the core-shell nanowires were measured using a quantum design magnetic properties measurement system (MPMS). Figure 8.4 displays the magnetic hysteresis loops measured at 300 K-10 K without field cooling (ZFC) for randomly oriented and after field cooling (FC) in 50 kOe from 300 K for randomly oriented and the aligned nanowires. The aligned sample was prepared by hardening Co nanowires in epoxy resin which has been described in detail elsewhere (section 7.2.3). Figure 8.4(b) shows that the FC loop is shifted opposite to the cooling field direction indicating an FC-induced unidirectional magnetic anisotropy. On the other hand no EB effect is observed in ZFC loop as seen in Figure 8.4(a). Figure 8.4(c-d) illustrates the M (H) measurements performed by applying field parallel and perpendicular to the nanowires axis. The effect of magnetic alignment shows a change in the squareness of the magnetic hysteresis loops and it leads to an enhanced remanence and coercivity combined with the influence of the shape anisotropy. A loop shift along the negative field axis is observed in both the parallel and perpendicular directions of the applied magnetic field (Figure 8.4(c-d)), which is interpreted as arising from the EB coupling.

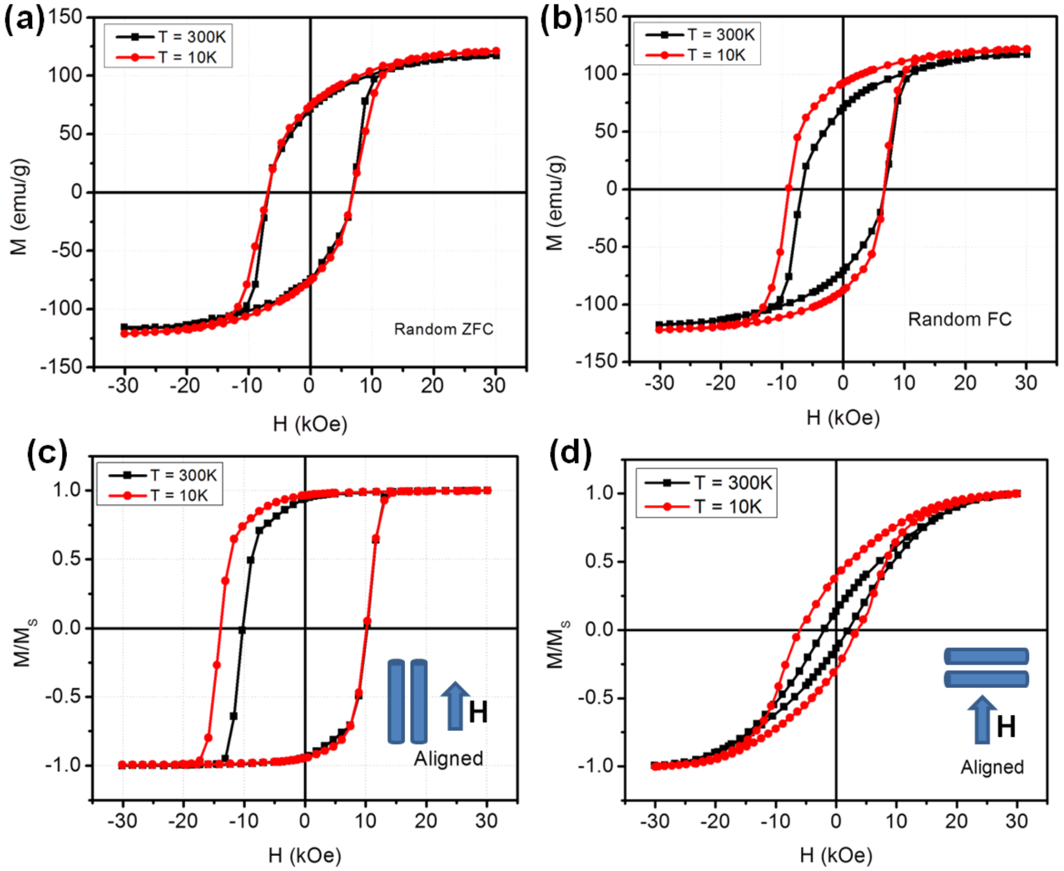

Figure 8.4 Hysteresis loops of Co/CoO core-shell nanowires (a) randomly oriented zero field cooling, (b) randomly oriented with 50 kOe field cooling, (c) parallel to the c-axis with 50 kOe field cooling and, (d) perpendicular to the c-axis with 50 kOe field cooling.

In order to understand the effect of the surface oxide shell on the magnetic properties, the H_C and H_{EB} as a function of temperature is summarized in Figure 8.5. It was measured under FC of 50 kOe while increasing temperature from 10 to 300 K. The coercive field values of parallel aligned (blue solid circle) and randomly oriented (blue solid circle) sample is shown in Figure 8.5(a-b). The coercivity is defined by $H_C = -(H_{C2}-H_{C1})/2$, where H_{C1} and H_{C2} are the left and right coercive fields, respectively. It can be observed that the temperature dependence of the coercivity in Co/CoO core-shell nanowires is non-monotonous and has noticeable oscillatory behavior. Initially, H_C decreases to a minimum at 100 K, then rises to a maximum at 200 K, and finally decreases again at 300 K for both randomly oriented and aligned sample. The most important feature is the increase in the coercive field to 13.5 kOe at T_N = 200 K. Such temperature dependence oscillatory behavior of coercivity is uncommon and is not observed in unidirectional Co/CoO bilayers [168] and Co/CoO nanoparticles [166] systems. Although, similar temperature dependencies of H_C as in the present study of Co/CoO nanowires with an epitaxial relation of the FM core and the AFM shell has been observed in few systems such as MnF_2/Fe films [178], macroporous Co/CoO nanoparticles [179] and Co/CoO [173], Ni/NiO [180], CoNi/CoO [181] nanorods.

The variation of H_{EB} with temperature for both aligned and randomly oriented samples is shown in Figure 8.5(c). The EB effect strongly depends on temperature, disappearing above the so-called blocking temperature (T_{EB}). The T_{EB} value correspond to ~ 150 K, which is below the bulk T_N of CoO (293 K), in close agreement with previously reported works [167, 170]. The T_N of bulk CoO (293 K) may decrease down to 150 K for a ~ 2 nm thick CoO shell due to finite size effect of AFM grains [182]. The exchange-bias field is defined by $H_{EB} = (H_{C1}+H_{C2})/2$, where H_{C1} and H_{C2} are the left and right coercive fields. The H_{EB} for aligned Co nanowires reaches 2.0 kOe at 10 K. The major source of magnetic anisotropy should switch from the AFM (CoO) shell to the FM (Co) core upon rising temperature. Thus, only AFM moments with high magnetic anisotropy, which are stable at low temperature, will only contribute to H_{EB}.

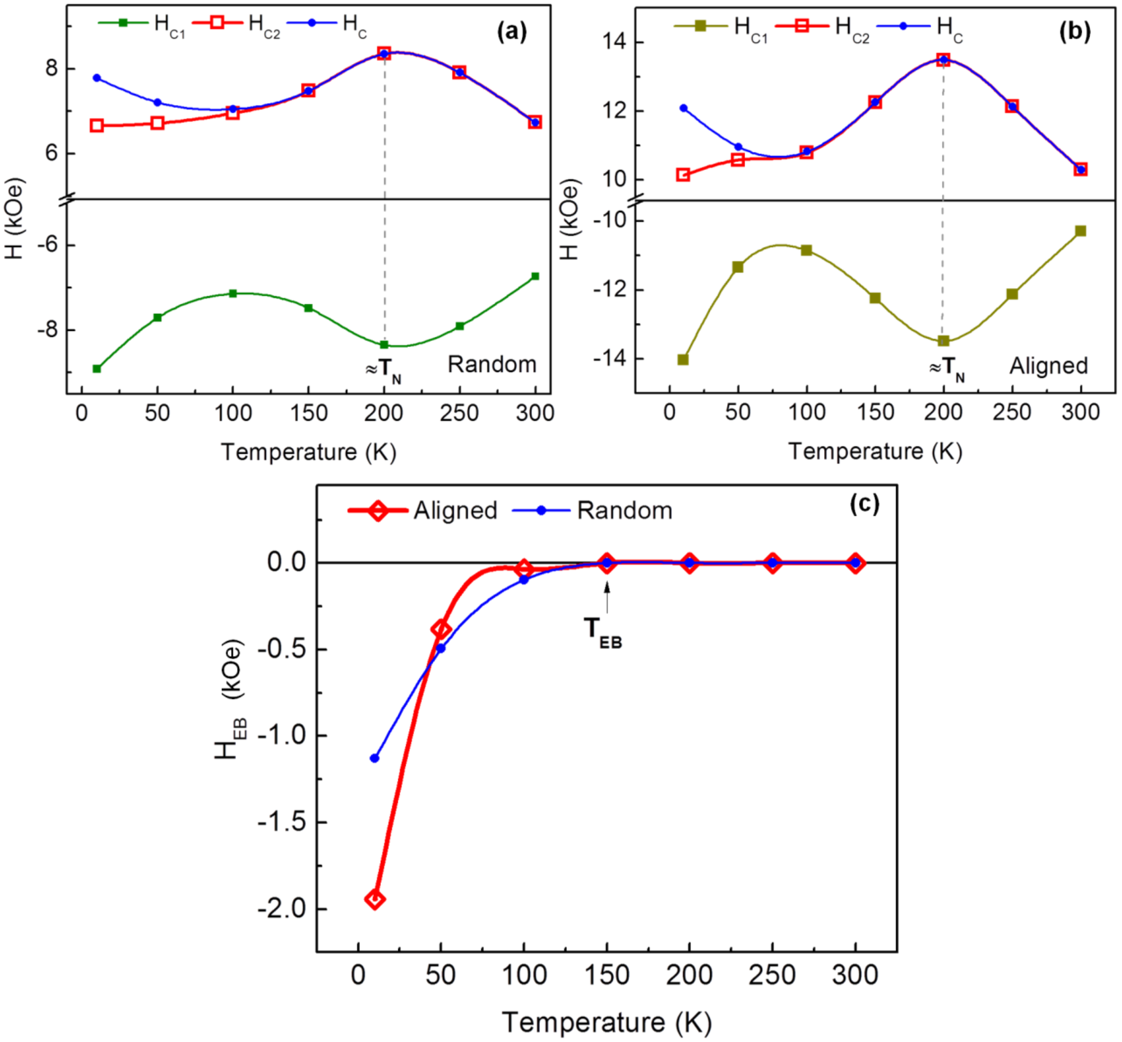

Figure 8.5 Temperature dependence of (a)-(b) coercivity H_C, and (c) exchange bias H_{EB} measured with the field cooling 50 kOe parallel to the nanowire axis and randomly oriented nanowires.

It is possible the minimum in H_C at 100 K is due to blocked AFM moments which act as nucleation points and promote the magnetization reversal of the wires as observed by Maurer et al. [173]. The temperature where the EB vanishes (T = 150 K) is the temperature limit of pinned interface moments, and then above AFM moments become thermally unstable which will affect the distribution of nucleation/pinning sites of FM. Therefore, the peak in the H_C at intermediate temperature T = 200 K can be associated with competing FM and AFM spin interactions in nanowires depending on the degree of crystallographic orientation between core and shell. The decrease in H_C at higher temperatures above T_N is presumably due the significant decrease of all anisotropy contributions in both the core and the shell.

8.3.2.2 Angular Dependence Magnetic Properties

To understand FM and AFM spin interactions on crystallographic orientation between core and shell of nanowires, directional properties of H_{EB} and H_C were further investigated. For the angular dependent measurement, the aligned Co nanowires sample was field cooled from 300 to 10 K in 50 kOe along the long axis of the nanowires.

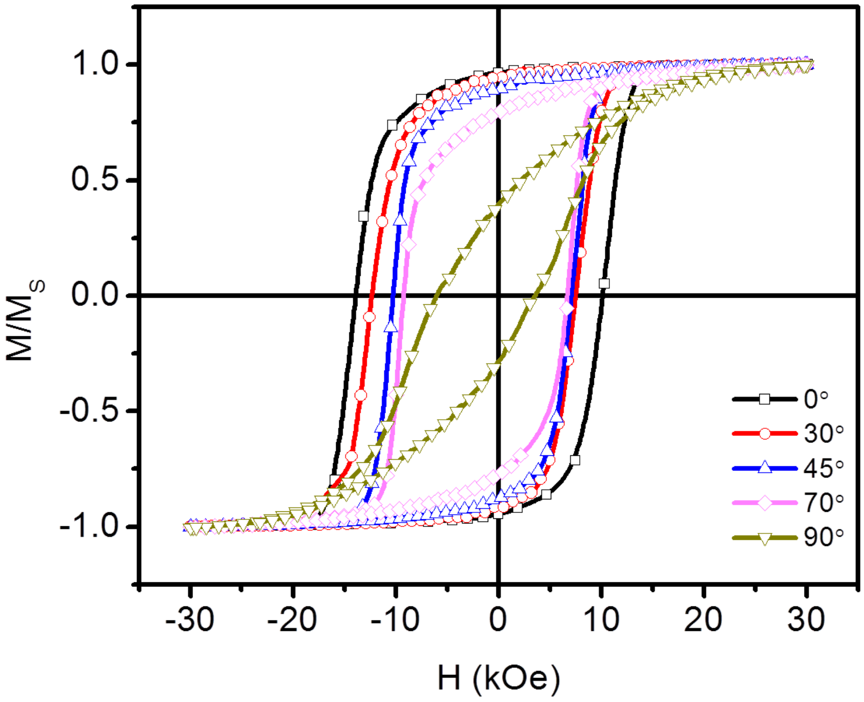

Figure 8.6 . Experimental angular dependent hysteresis loops of Co/CoO nanowires measured at 10 K.

For θ = 0°, external magnetic field (H_{app}) was applied along the field cooling direction. For further angular dependent measurements, the direction of H_{FC} and H_{app} was kept same while the sample was rotated by varying angles θ = 30°, 45°, 60°, 70° and 90°. Figure 8.6 show the corresponding hysteresis loops at 10 K as function of θ, and the resulting angular dependence of H_{EB}, M_r/M_S and H_C extracted from the hysteresis loops are plotted in Figure 8.7. We observed that the magnetization reversal in the nanowire arrays is markedly sensitive to variation in θ. Figure 8.7(a) and (b) clearly shows that there is a decrease in M_r/M_S and H_C with increasing θ until $\theta \leq 90°$. This is accompanied by a gradual change in the squareness of hysteresis loops. Typical hard axis hysteresis loops with minimum H_C is obtained for θ = 90°, where the applied field is perpendicular to the long axis of the nanowires. This behavior is consistent with the coherent rotation reversal mode based on the Stoner–Wohlfarth model [10].

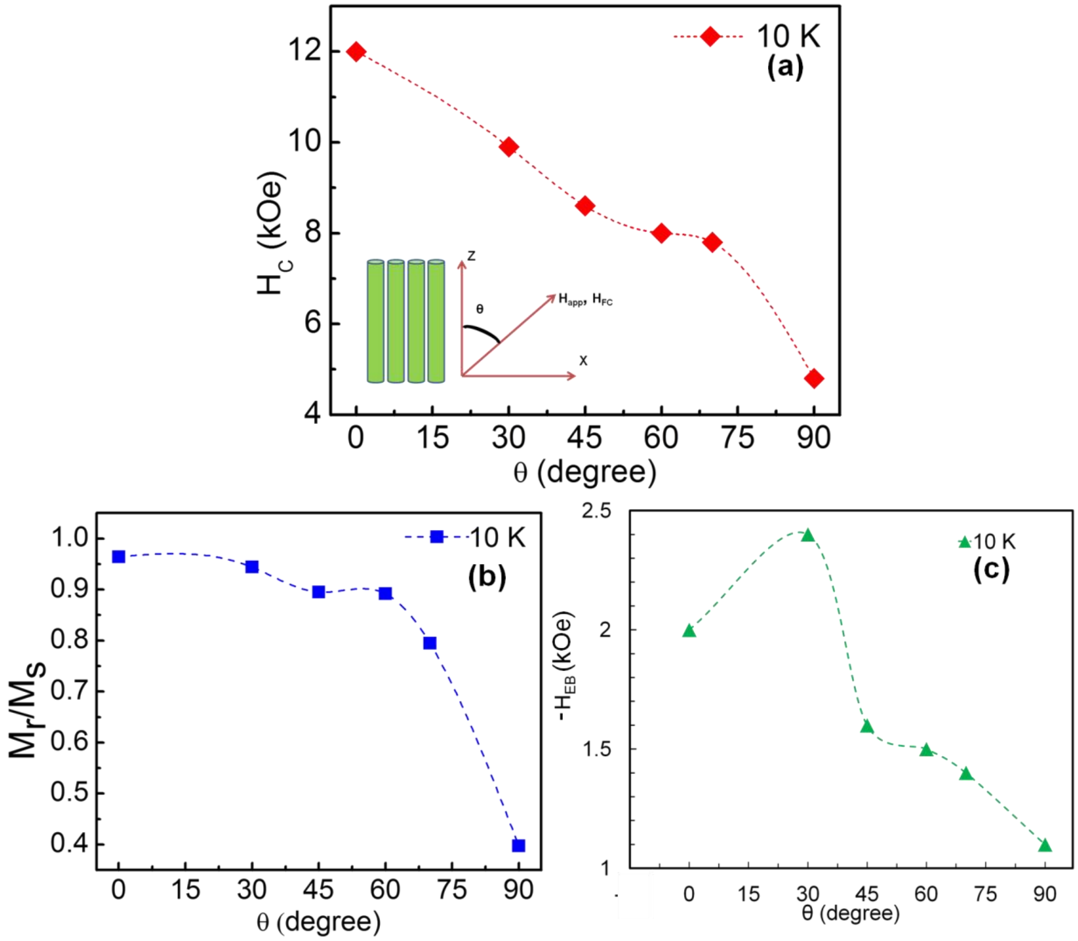

Figure 8.7 Experimental angular dependent extracted from hysteresis loops, (a) coercivity, (b) remanence to saturation magnetization ratio and, (c) exchange bias of Co/CoO nanowires measured at 10 K.

Further analysis of Figure 8.7(c) reveals a wide range of interesting observations. With increasing θ, H_{EB} increases until at θ = 30° where it reaches a maximum. It should be noted that at its maximum, the shift in the hysteresis loops is H_{EB} = 2.4 kOe, which is 400 Oe larger than the maximum shift obtained for θ = 0. Furthermore, a finite shift of H_{EB} = 1.1 kOe is observed in the hysteresis loop for θ = 90°. It has been widely believed that the largest and least values of H_{EB} are expected at θ = 0° and θ = 90° [183]. Instead the largest value of H_{EB} is located at θ = 30° indicating H_{EB} does not have simple cosθ dependence. It is also clear that the orientation (i.e., sign) of EB remains in the same direction for the entire range of θ. Interestingly, we also note that H_{EB} is symmetric about θ = 90°. This may be attributed to the shape symmetry in the geometry of the nanowires due to which the competing anisotropies in this system are identical for θ and θ+90°. The crystallographic c-axis (002) in the core is collinear with the long axis of the nanowires. Oxide shell on the Co surface appears polycrystalline with crystallographic orientation (002) and (111) on the nanowire facet. In the bulk CoO, paramagnetic to antiferromagnetic transition is accompanied by a cubic to monoclinic crystallographic distortion below T_N with a large tetragonal distortion along the cube edges with c/a < 1 and a small deformation along ⟨111⟩ [184]. As a consequence, a pseudocubic structure with two CoO units per cell is formed and the spins align collinearly along <110> in AFM state [184, 185]. We hypothesize that the spin orientation in the AFM shell is similar. In addition, stress at the interface of FM/AFM will result such that spins are not collinear to the c-axis of the FM core and AFM shell. This misalignment of FM and AFM spins at the interface certainly has strong impact on the magnetic properties

8.4 Conclusion

In summary, we have studied the temperature and angular dependence of the H_{EB} and H_C in exchange-coupled FM/AFM, Co core - CoO shell nanowires. HRTEM observation reveals single crystalline Co core with (002) crystallographic orientation along the length is covered with randomly oriented crystallites of CoO oxide shell. Temperature dependence of EB have shown the apparent T_{EB} ~ 150 K, well below the T_N of bulk CoO (293 K) with high H_{EB} of 2 kOe. The temperature dependence of the H_C was found to be non-monotonous with oscillatory behavior. H_{EB} and H_C have unidirectional and uniaxial characteristics with same symmetry but different angular dependence. H_{EB} is strongly affected by the spin orientations at the interface between the FM and AFM. The angular dependence of EB have maxima at 30°. This behavior is attributed to non collinear spins of magnetic easy axis of Co core and CoO shell. Manipulation and control of the EB provides tunable source of anisotropy in the nanowires which leads to a better understanding of the EB effect thereby leading to advancement in the applications of Co nanowires in future permanent magnets and recording media.

Chapter 9

Summary and Conclusions

Permanent magnets are essential components in modern technologies, being employed in a huge number of large-scale and emerging applications, such as electronic devices, hard drives, automobiles, wind turbines, and electric vehicles. Since their introduction in the late 60s, rare-earth (RE)-based compounds have been produced as the strongest permanent magnets. Nowadays they account for the largest production volume in value of permanents magnets. The rare-earth compounds, however, have also some disadvantages as permanent magnets, for instance the relatively low magnetization and limited thermal stability compared to ferromagnetic 3d transition metal like Fe, Co, Ni and their alloys. Extensive research in recent years in magnetic nanoparticles especially in magnetic nanowires and nanorods has renewed the interests in developing high coercivity in transition metal nanocrystals based on shape anisotropy.

This dissertation focuses on the synthesis and characterization of magnetic nanostructures of 3d transition metal with high aspect ratio. Their bimetallic alloys, and ferrites are also investigated. The main objective of this work has been to emphasize the role of magnetocrystalline anisotropy and shape anisotropy in the high aspect ratio magnetic nanostructure.

The $CoFe_2O_4$ nanocrystals with size in a broad range (from 20 to 60 nm), narrow size distributions, and controlled shape and stoichiometry have been synthesized via one step hydrothermal method. The evolution of the magnetic properties was studied as a function of the particles size and shape, with particular attention to those determining the best performance in view of a possible application for the realization of permanent magnets. In particular, we focused on the analysis of H_C, remnant magnetization, M_r, and the maximum energy product, $(BH)_{max}$. We found that at room temperature single crystalline 40 nm nanoparticles exhibit the best magnetic properties, and the highest $(BH)_{max}$ is observed for nanoparticles with average size of ~ 40 nm. This is also the highest $(BH)_{max}$ ever reported for randomly oriented cobalt-ferrite nanoparticles (2.0 MGOe).

Mesoporous iron and iron oxides nanowires/nanorods with well-controlled morphology and composition were prepared by a novel method using fluidization reduction technique. The synthesis consists of producing α-FeOOH nanowires by a hydrothermal method using $FeCl_3$ salt. The iron hydroxide nanowires were then converted into the mesoporous iron oxides nanowire arrays and eventually to mesoporous α-Fe nanorods in the presence of forming gas using a fluidized bed reactor. The as-prepared Fe based mesoporous nanowires/nanorods exhibited high specific surface area. The effect of shape anisotropy was observed with the alignment of nanowires/nanorods in magnetic field. These porous nanowires/nanorods may find important applications in the future for magnetic recording media, gas, and heavy metal ion adsorbents, catalysts, hydrogen and Li ion storage.

FeCo nanocrystals were prepared by reductive decomposition chemical solution method in presence of surfactant. By adjusting the synthesis parameters, such as the initial precursor concentration, reducing agent amount, heating rate and surfactants ratio, the morphology can be controlled. Magnetic properties of these nanocrystals are size and shape dependent. By adjusting the parameters of synthesis condition, the highest M_S of 92 emu/g and coercive force up to 1.2 kOe were obtained at room temperature for the $Fe_{60}Co_{40}$ nanowires of lengths of 60-140 nm and diameters of 4-8 nm.

CoNi nanowires were synthesized using so called-polyol method. By varying the catalyst concentration in proper ranges, the effect of synthetic parameters on controlling cobalt-nickel particles with different shapes such as dumbbells, rods or wires is demonstrated. The influence of the catalyst concentration on the morphology and magnetic properties were studied. The coercivity of the CoNi nanowires depends on the morphology of nanocrystals. The highest coercive force of 2.9 kOe was obtained for 50x200 nm nanowires with $Co_{80}Ni_{20}$ composition when synthesized in flask. $Co_{95}Ni_5$ nanowires have also synthesized using cobalt and nickel sterate precursor in BEG by solvothermal process. The experimental coercivity of 4.1 kOe and Ms of 129 emu/g were obtained for randomly oriented at room temperature. After performing magnetic field alignment the coercivity increases to 5.1 kOe for the parallel oriented nanowires assembly.

Cobalt nanowires with high aspect ratio have been synthesized via a solvothermal chemical process. Shape anisotropy provides the basis of the enhanced coercivity, and the orientation and uniformity of the single-domain nanocrystals are essential for achieving high magnetic energy density. Present experiments show that Co nanowires with diameters of ~ 15 nm and an average length of 200 nm have a record high coercivity of 12.5 kOe at room temperature, leading to an energy product of ~ 44 MGOe. These excellent properties suggest that composite materials based on these wires could be used to fabricate permanent magnet materials. Experimental data on the angular dependence of coercivity have been compared with analytical calculations. Temperature is also an important parameter that modifies the effective magnetic anisotropy. I have studied their high temperature behavior (up to 500 K) and I propose that these materials could compete with existing permanent magnetic materials at high temperature (up to 300 °C).

Such nanowires are prone to oxidation which has proved to strongly affect their magnetic properties at low temperature ($T < 200$ K). I have shown by HRTEM that a CoO shell forms around the wires. This shell orders anti-ferromagnetically at 200 K and strongly modifies the magnetic properties of the wires at low temperatures via the exchange bias effect. In addition, stress at the interface of FM/AFM will result such that spins are not collinear to the c-axis of the FM core and AFM shell. This misalignment of FM and AFM spins at the interface certainly has strong impact on the magnetic properties.

This work opens the way to three main research orientations: 1) effect of shape of the nanowires on magnetic properties 2) the role of the geometry in the magnetization reversal, 3) the influence of the oxidation on their magnetic properties.

Appendix A

Units and Dimensions

Table A.1 Conversion factors for common magnetic terms in CGS and SI units [13].

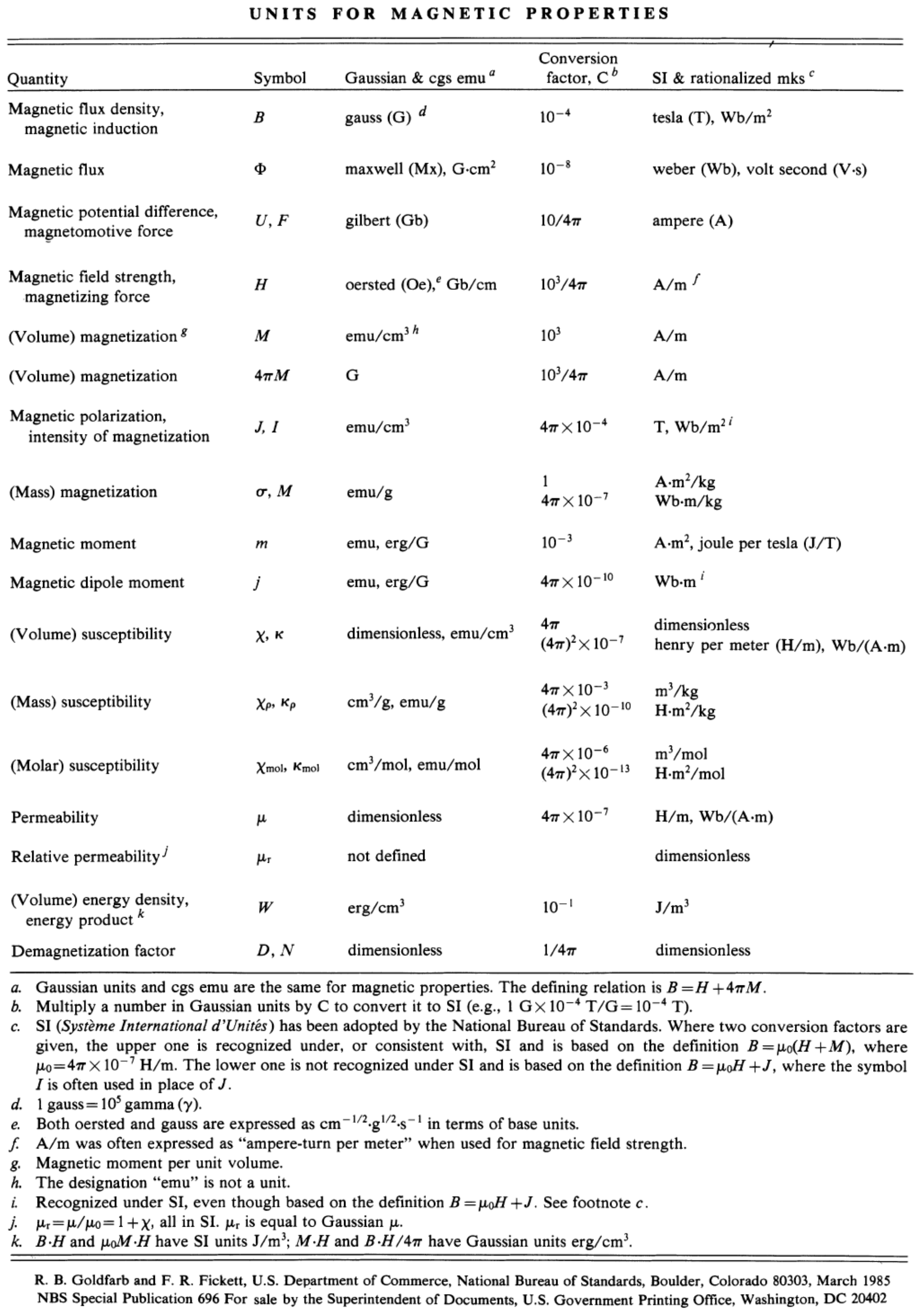

UNITS FOR MAGNETIC PROPERTIES

Quantity	Symbol	Gaussian & cgs emu [a]	Conversion factor, C [b]	SI & rationalized mks [c]
Magnetic flux density, magnetic induction	B	gauss (G) [d]	10^{-4}	tesla (T), Wb/m^2
Magnetic flux	Φ	maxwell (Mx), G·cm^2	10^{-8}	weber (Wb), volt second (V·s)
Magnetic potential difference, magnetomotive force	U, F	gilbert (Gb)	$10/4\pi$	ampere (A)
Magnetic field strength, magnetizing force	H	oersted (Oe),[e] Gb/cm	$10^3/4\pi$	A/m [f]
(Volume) magnetization [g]	M	emu/cm^3 [h]	10^3	A/m
(Volume) magnetization	$4\pi M$	G	$10^3/4\pi$	A/m
Magnetic polarization, intensity of magnetization	J, I	emu/cm^3	$4\pi \times 10^{-4}$	T, Wb/m^2 [i]
(Mass) magnetization	σ, M	emu/g	1 $4\pi \times 10^{-7}$	A·m^2/kg Wb·m/kg
Magnetic moment	m	emu, erg/G	10^{-3}	A·m^2, joule per tesla (J/T)
Magnetic dipole moment	j	emu, erg/G	$4\pi \times 10^{-10}$	Wb·m [i]
(Volume) susceptibility	χ, κ	dimensionless, emu/cm^3	4π $(4\pi)^2 \times 10^{-7}$	dimensionless henry per meter (H/m), Wb/(A·m)
(Mass) susceptibility	χ_ρ, κ_ρ	cm^3/g, emu/g	$4\pi \times 10^{-3}$ $(4\pi)^2 \times 10^{-10}$	m^3/kg H·m^2/kg
(Molar) susceptibility	$\chi_{\mathrm{mol}}, \kappa_{\mathrm{mol}}$	cm^3/mol, emu/mol	$4\pi \times 10^{-6}$ $(4\pi)^2 \times 10^{-13}$	m^3/mol H·m^2/mol
Permeability	μ	dimensionless	$4\pi \times 10^{-7}$	H/m, Wb/(A·m)
Relative permeability [j]	μ_r	not defined		dimensionless
(Volume) energy density, energy product [k]	W	erg/cm^3	10^{-1}	J/m^3
Demagnetization factor	D, N	dimensionless	$1/4\pi$	dimensionless

a. Gaussian units and cgs emu are the same for magnetic properties. The defining relation is $B = H + 4\pi M$.

b. Multiply a number in Gaussian units by C to convert it to SI (e.g., $1\ \mathrm{G} \times 10^{-4}\ \mathrm{T/G} = 10^{-4}\ \mathrm{T}$).

c. SI (*Système International d'Unités*) has been adopted by the National Bureau of Standards. Where two conversion factors are given, the upper one is recognized under, or consistent with, SI and is based on the definition $B = \mu_0(H + M)$, where $\mu_0 = 4\pi \times 10^{-7}$ H/m. The lower one is not recognized under SI and is based on the definition $B = \mu_0 H + J$, where the symbol I is often used in place of J.

d. 1 gauss $= 10^5$ gamma (γ).

e. Both oersted and gauss are expressed as cm$^{-1/2}$·g$^{1/2}$·s^{-1} in terms of base units.

f. A/m was often expressed as "ampere-turn per meter" when used for magnetic field strength.

g. Magnetic moment per unit volume.

h. The designation "emu" is not a unit.

i. Recognized under SI, even though based on the definition $B = \mu_0 H + J$. See footnote *c*.

j. $\mu_r = \mu/\mu_0 = 1 + \chi$, all in SI. μ_r is equal to Gaussian μ.

k. $B \cdot H$ and $\mu_0 M \cdot H$ have SI units J/m^3; $M \cdot H$ and $B \cdot H/4\pi$ have Gaussian units erg/cm^3.

R. B. Goldfarb and F. R. Fickett, U.S. Department of Commerce, National Bureau of Standards, Boulder, Colorado 80303, March 1985
NBS Special Publication 696 For sale by the Superintendent of Documents, U.S. Government Printing Office, Washington, DC 20402

Appendix B

Research Accomplishments

Awards

- College of Science Dissertation Fellowship, University of Texas at Arlington (UTA) 2015.
- DOE ARPA-E award to attend REPM 2014 workshop at Annapolis, MD 2014.
- Scharff Award Scholarship, Department of Physics, UTA 2013.
- The 5th IEEE Magnetics Society Summer School Award, SRM University, Chennai, India 2012.

Publications

1. Gandha, K.; Elkins, K.; Poudyal, N.; Liu, J. P., Synthesis and characterization of $CoFe_2O_4$ nanoparticles with high coercivity. J. Appl. Phys. 2015, 117 (17), 17A736.
2. Gandha, K.; Tsai, P.; Chaubey, G.; Poudyal, N.; Elkins, K.; Cui, J.; Liu, J. P., Synthesis and characterization of FeCo nanowires with high coercivity. Nanotechnology 2015, 26 (7), 075601.
3. Gandha, K.; Elkins, K.; Poudyal, N.; Liu, X.; Liu, J. P., High Energy Product Developed from Cobalt Nanowires. Sci. Rep. 2014, 4.
4. Gandha, K.; Poudyal, N.; Qiang, Z.; Liu, J. P., Effect of $RuCl_3$ on Morphology and Magnetic Properties of CoNi Nanowires. IEEE Trans. Magn. 2013, 49 (7), 3273-3276.
5. Poudyal, N; Gandha, K.; Elkins, K.; Liu, J.P., Anisotropic SmCo5/FeCo core/shell nanocomposite chips prepared via electroless coating. AIMS Mater. Sci., 2015, 2(3): 294-302.
6. Poudyal, N.; Elkins, K.; Gandha, K.; Liu, J.P., FeCo Coating on SmCo5 Nanochips by a Sonochemical Method. IEEE Trans. Magn. , 2015, vol. PP, no.99, pp.1-1
7. Ma, Y.; Liu, X.; Gandha, K.; Vuong, N. et al., Preparation and magnetic properties of MnBi-based hard/soft composite magnets" J. Appl. Phys., 2014,115 (7), 17A755-1.
8. Poudyal, N.; Elkins, K.; Gandha, K.; Liu, J. P., Synthesis and Processing of Hard Magnetic Nanoparticles Rare Earth and Future Permanent Magnets and Their Applications Aug 2014.
9. Gandha, K.; Elkins, K.; Poudyal, N.; Liu, J. P., Fabrication of mesoporous Fe-based nanowires/nanorods by fluidized bed reduction of α-FeOOH nanowires. Submitted to Journal.

10. Gandha, K.; Elkins, K.; Poudyal, N.; Liu, J. P., Temperature and Angular Dependence of Coercivity and Exchange Bias of Co/CoO Core-Shell Nanowires. Submitted to Journal.

Conference Presentations

1. Structure and magnetic properties of Co/CoO core-shell nanowires, APS March Meeting San Antonio, TX, USA March 2015.

2. Synthesis and characterization of $CoFe_2O_4$ nanoparticles with high coercivity, 59th MMM meeting, Honolulu, Hawaii, USA November 2014.

3. Synthesis of Fe Nanowires via a Novel Approach,Texas Society of Microscopy (TSM) Irving, TX, USA April 2014 & APS March Meeting Denver, CO, USA March 2014

4. Synthesis and characterization of ferromagnetic FeCo nanowires 58th MMM meeting, Denver, CO, USA November 2013

5. Synthesis and Characterization of CoNi and FeCo Nanowires with High Coercivity, Texas Society of Microscopy (TSM) Irving, TX, USA April 2013 & APS March Meeting Baltimore, MD, USA March 2013.

6. Effect of $RuCl_3$ on morphology and magnetic properties of CoNi nanowires, Joint MMM-Intermag, Chicago, IL, USA November 2012.

.

References

[1] S. Goudsmit, G. Uhlenbeck, Physica, 6 (1926) 273-290.

[2] G.E. Uhlenbeck, S. Goudsmit, Naturwissenschaften, 13 (1925) 953-954.

[3] W. Heisenberg, Z. Physik, 38 (1926) 411-426.

[4] P.A.M. Dirac, Proceedings of the Royal Society of London A: Mathematical, Physical and Engineering Sciences, 112 (1926) 661-677.

[5] C.M. Hurd, Contemporary Physics, 23 (1982) 469-493.

[6] B.D. Cullity, C.D. Graham, Ebooks Corporation., John Wiley & Sons, Hoboken, 2009, pp. 564 p.

[7] J.M.D. Coey, Magnetism and magnetic materials, Cambridge University Press, Cambridge, 2010.

[8] R.C. O'Handley, Modern magnetic materials : principles and applications, Wiley, New York, 2000.

[9] R. Krahne, G. Morello, A. Figuerola, C. George, S. Deka, L. Manna, Physics Reports, 501 (2011) 75-221.

[10] E.C. Stoner, E.P. Wohlfarth, Philosophical Transactions of the Royal Society of London A: Mathematical, Physical and Engineering Sciences, 240 (1948) 599-642.

[11] E.H. Frei, S. Shtrikman, D. Treves, Physical Review, 106 (1957) 446-455.

[12] I.S. Jacobs, C.P. Bean, Physical Review, 100 (1955) 1060-1067.

[13] H.-B. Braun, Physical Review Letters, 71 (1993) 3557-3560.

[14] U. Nowak, R.W. Chantrell, E.C. Kennedy, Physical Review Letters, 84 (2000) 163-166.

[15] F.E. Luborsky, Journal of Applied Physics, 32 (1961) S171-S183.

[16] A. Thiaville, Journal of Magnetism and Magnetic Materials, 182 (1998) 5-18.

[17] A. Thiaville, Physical Review B, 61 (2000) 12221-12232.

[18] R. Skomski, J.M.D. Coey, Permanent magnetism, Institute of Physics Pub., Bristol, UK ; Philadelphia, PA, 1999.

[19] R. Skomski, H. Zeng, M. Zheng, D.J. Sellmyer, Physical Review B, 62 (2000) 3900-3904.

[20] C. Tannous, J. Gieraltowski, European Journal of Physics, 29 (2008) 475.

[21] P. Landeros, S. Allende, J. Escrig, E. Salcedo, D. Altbir, E.E. Vogel, Applied Physics Letters, 90 (2007) 102501.

[22] J. Escrig, J. Bachmann, J. Jing, M. Daub, D. Altbir, K. Nielsch, Physical Review B, 77 (2008) 214421.

[23] A. Aharoni, Journal of Applied Physics, 82 (1997) 1281-1287.

[24] W.H. Meiklejohn, C.P. Bean, Physical Review, 102 (1956) 1413-1414.

[25] W.H. Meiklejohn, C.P. Bean, Physical Review, 105 (1957) 904-913.

[26] J. Nogués, I.K. Schuller, Journal of Magnetism and Magnetic Materials, 192 (1999) 203-232.

[27] J. Nogués, J. Sort, V. Langlais, V. Skumryev, S. Suriñach, J.S. Muñoz, M.D. Baró, Physics Reports, 422 (2005) 65-117.

[28] M. Kiwi, Journal of Magnetism and Magnetic Materials, 234 (2001) 584-595.

[29] A.E. Berkowitz, K. Takano, Journal of Magnetism and Magnetic Materials, 200 (1999) 552-570.

[30] R.L. Stamps, Journal of Physics D: Applied Physics, 33 (2000) R247.

[31] S.S.P. Parkin, N. More, K.P. Roche, Physical Review Letters, 64 (1990) 2304-2307.

[32] P. Grünberg, R. Schreiber, Y. Pang, M.B. Brodsky, H. Sowers, Physical Review Letters, 57 (1986) 2442-2445.

[33] B. Dieny, V.S. Speriosu, S.S.P. Parkin, B.A. Gurney, D.R. Wilhoit, D. Mauri, Physical Review B, 43 (1991) 1297-1300.

[34] P. Bruno, C. Chappert, Physical Review Letters, 67 (1991) 1602-1605.

[35] W. Brodkorb, W. Haubenreisser, physica status solidi (a), 3 (1970) 333-341.

[36] K. Nishioka, C. Hou, H. Fujiwara, R.D. Metzger, Journal of Applied Physics, 80 (1996) 4528-4533.

[37] L.H. Lewis, F. Jiménez-Villacorta, Metallurgical and Materials Transactions A, 44 (2013) 2-20.

[38] D. Jiles, Acta Materialia, 51 (2003) 5907-5939.

[39] D. Niarchos, G. Giannopoulos, M. Gjoka, C. Sarafidis, V. Psycharis, J. Rusz, A. Edström, O. Eriksson, P. Toson, J. Fidler, JOM, 1-11.

[40] J.M.D. Coey, Magnetics, IEEE Transactions on, 47 (2011) 4671-4681.

[41] C.N.R. Rao, F.L. Deepak, G. Gundiah, A. Govindaraj, Progress in Solid State Chemistry, 31 (2003) 5-147.

[42] R.G. Hobbs, N. Petkov, J.D. Holmes, Chemistry of Materials, 24 (2012) 1975-1991.

[43] M. Kwiat, S. Cohen, A. Pevzner, F. Patolsky, Nano Today, 8 (2013) 677-694.

[44] M. Law, J. Goldberger, P. Yang, Annual Review of Materials Research, 34 (2004) 83-122.

[45] P.I. Yu, L.G. Vivas, A. Asenjo, A. Chuvilin, O. Chubykalo-fesenko, M. Vázquez, EPL (Europhysics Letters), 102 (2013) 17009.

[46] L.G. Vivas, M. Vázquez, V. Vega, J. García, W.O. Rosa, R.P. del Real, V.M. Prida, Journal of Applied Physics, 111 (2012) 07A325.

[47] F. Dumestre, B. Chaudret, C. Amiens, M.-C. Fromen, M.-J. Casanove, P. Renaud, P. Zurcher, Angewandte Chemie, 114 (2002) 4462-4465.

[48] P. Narayan, S.C. Girija, N. Vikas, R. Chuan-bing, Y. Kazuaki, J.P. Liu, Nanotechnology, 19 (2008) 355601.

[49] X. Peng, L. Manna, W. Yang, J. Wickham, E. Scher, A. Kadavanich, A.P. Alivisatos, Nature, 404 (2000) 59-61.

[50] T.S. Ahmadi, Z.L. Wang, T.C. Green, A. Henglein, M.A. El-Sayed, Science, 272 (1996) 1924-1925.

[51] N.R. Jana, Chemical Communications, (2003) 1950-1951.

[52] X. Peng, J. Wickham, A.P. Alivisatos, Journal of The American Chemical Society, 120 (1998) 5343-5344.

[53] V.G. Harris, Y. Chen, A. Yang, S. Yoon, Z. Chen, A.L. Geiler, J. Gao, C.N. Chinnasamy, L.H. Lewis, C. Vittoria, E.E. Carpenter, K.J. Carroll, R. Goswami, M.A. Willard, L. Kurihara, M. Gjoka, O. Kalogirou, Journal of Physics D: Applied Physics, 43 (2010) 165003.

[54] Y. Zhang, G.S. Chaubey, C. Rong, Y. Ding, N. Poudyal, P.-c. Tsai, Q. Zhang, J.P. Liu, Journal of Magnetism and Magnetic Materials, 323 (2011) 1495-1500.

[55] Z.J. Huba, E.E. Carpenter, Journal of Applied Physics, 111 (2012) 07B529.

[56] C. Feldmann, Solid State Sciences, 7 (2005) 868-873.

[57] P. Toneguzzo, G. Viau, O. Acher, F. Guillet, E. Bruneton, F. Fievet-Vincent, F. Fievet, Journal of Materials Science, 35 (2000) 3767-3784.

[58] G. Viau, F. Fiévet-Vincent, F. Fiévet, Solid State Ionics, 84 (1996) 259-270.

[59] G.S. Chaubey, C. Barcena, N. Poudyal, C. Rong, J. Gao, S. Sun, J.P. Liu, Journal of the American Chemical Society, 129 (2007) 7214-7215.

[60] P. Toneguzzo, O. Acher, G. Viau, F. Fiévet-Vincent, F. Fiévet, Journal of Applied Physics, 81 (1997) 5546-5548.

[61] G. Viau, P. Toneguzzo, A. Pierrard, O. Acher, F. Fiévet-Vincent, F. Fiévet, Scripta Materialia, 44 (2001) 2263-2267.

[62] H. Hayashi, Y. Hakuta, Materials, 3 (2010) 3794.

[63] J.R. Heath, F.K. LeGoues, Chemical Physics Letters, 208 (1993) 263-268.

[64] V.K. LaMer, R.H. Dinegar, Journal of the American Chemical Society, 72 (1950) 4847-4854.

[65] V.K.L. Mer, Industrial & Engineering Chemistry, 44 (1952) 1270-1277.

[66] I.M. Lifshitz, V.V. Slyozov, Journal of Physics and Chemistry of Solids, 19 (1961) 35-50.

[67] C. Wagner, Z. Elektrochem, 65 (1961) 581-591.

[68] T. Sugimoto, Advances in Colloid and Interface Science, 28 (1987) 65-108.

[69] N. Wang, Y. Cai, R.Q. Zhang, Materials Science and Engineering: R: Reports, 60 (2008) 1-51.

[70] J.D. Holmes, K.P. Johnston, R.C. Doty, B.A. Korgel, Science, 287 (2000) 1471.

[71] T. Hanrath, B.A. Korgel, Journal of the American Chemical Society, 124 (2002) 1424-1429.

[72] R.K. Joshi, J.J. Schneider, Chemical Society Reviews, 41 (2012) 5285-5312.

[73] R.L. Penn, J.F. Banfield, Geochimica et cosmochimica acta, 63 (1999) 1549-1557.

[74] K. Gandha, K. Elkins, N. Poudyal, X. Liu, J.P. Liu, Scientific reports, 4 (2014) 5345.

[75] K. Gandha, N. Poudyal, Z. Qiang, J.P. Liu, Magnetics, IEEE Transactions on, 49 (2013) 3273-3276.

[76] Y. Cedeño-Mattei, O. Perales-Pérez, Microelectronics Journal, 40 (2009) 673-676.

[77] B.H. Liu, J. Ding, Z.L. Dong, C.B. Boothroyd, J.H. Yin, J.B. Yi, Physical Review B, 74 (2006) 184427.

[78] Q. Song, Y. Ding, Z.L. Wang, Z.J. Zhang, The Journal of Physical Chemistry B, 110 (2006) 25547-25550.

[79] C. Cannas, A. Musinu, G. Piccaluga, D. Fiorani, D. Peddis, H.K. Rasmussen, S. Mørup, The Journal of Chemical Physics, 125 (2006) 164714.

[80] R.M. Bozorth, E.F. Tilden, A.J. Williams, Physical Review, 99 (1955) 1788-1798.

[81] L. Stichauer, G. Gavoille, Z. Simsa, Journal of Applied Physics, 79 (1996) 3645-3650.

[82] H. Zeng, J. Li, J.P. Liu, Z.L. Wang, S. Sun, Nature, 420 (2002) 395-398.

[83] J. Park, K. An, Y. Hwang, J.-G. Park, H.-J. Noh, J.-Y. Kim, J.-H. Park, N.-M. Hwang, T. Hyeon, Nat Mater, 3 (2004) 891-895.

[84] G.C.P. Leite, E.F. Chagas, R. Pereira, R.J. Prado, A.J. Terezo, M. Alzamora, E. Baggio-Saitovitch, Journal of Magnetism and Magnetic Materials, 324 (2012) 2711-2716.

[85] Q.A. Pankhurst, J. Connolly, S.K. Jones, J. Dobson, Journal of Physics D: Applied Physics, 36 (2003) R167.

[86] G.V.M. Jacintho, A.G. Brolo, P. Corio, P.A.Z. Suarez, J.C. Rubim, The Journal of Physical Chemistry C, 113 (2009) 7684-7691.

[87] Z. Zi, Y. Sun, X. Zhu, Z. Yang, J. Dai, W. Song, Journal of Magnetism and Magnetic Materials, 321 (2009) 1251-1255.

[88] Y. Yu, A. Mendoza-Garcia, B. Ning, S. Sun, Advanced Materials, 25 (2013) 3090-3094.

[89] Y. Lee, J. Lee, C.J. Bae, J.G. Park, H.J. Noh, J.H. Park, T. Hyeon, Advanced Functional Materials, 15 (2005) 503-509.

[90] N. Hanh, O.K. Quy, N.P. Thuy, L.D. Tung, L. Spinu, Physica B: Condensed Matter, 327 (2003) 382-384.

[91] R.P. Chaudhary, S.K. Mohanty, A.R. Koymen, Carbon, 79 (2014) 67-73.

[92] Y.C. Wang, J. Ding, J.B. Yi, B.H. Liu, T. Yu, Z.X. Shen, Applied Physics Letters, 84 (2004) 2596-2598.

[93] C.N. Chinnasamy, B. Jeyadevan, K. Shinoda, K. Tohji, D.J. Djayaprawira, M. Takahashi, R.J. Joseyphus, A. Narayanasamy, Applied Physics Letters, 83 (2003) 2862-2864.

[94] M.V. Limaye, S.B. Singh, S.K. Date, D. Kothari, V.R. Reddy, A. Gupta, V. Sathe, R.J. Choudhary, S.K. Kulkarni, The Journal of Physical Chemistry B, 113 (2009) 9070-9076.

[95] G.B. Ji, S.L. Tang, S.K. Ren, F.M. Zhang, B.X. Gu, Y.W. Du, Journal of Crystal Growth, 270 (2004) 156-161.

[96] S.W. da Silva, T.F.O. Melo, M.A.G. Soler, E.C.D. Lima, M.F. da Silva, P.C. Morais, Magnetics, IEEE Transactions on, 39 (2003) 2645-2647.

[97] M.A.G. Soler, T.F.O. Melo, S.W. da Silva, E.C.D. Lima, A.C.M. Pimenta, V.K. Garg, A.C. Oliveira, P.C. Morais, Journal of Magnetism and Magnetic Materials, 272–276, Part 3 (2004) 2357-2358.

[98] M.A.G. Soler, E.C.D. Lima, S.W. da Silva, T.F.O. Melo, A.C.M. Pimenta, J.P. Sinnecker, R.B. Azevedo, V.K. Garg, A.C. Oliveira, M.A. Novak, P.C. Morais, Langmuir, 23 (2007) 9611-9617.

[99] G. Shemer, E. Tirosh, T. Livneh, G. Markovich, The Journal of Physical Chemistry C, 111 (2007) 14334-14338.

[100] Y. Melikhov, J.E. Snyder, D.C. Jiles, A.P. Ring, J.A. Paulsen, C.C.H. Lo, K.W. Dennis, Journal of Applied Physics, 99 (2006) 08R102.

[101] T. Bala, C.R. Sankar, M. Baidakova, V. Osipov, T. Enoki, P.A. Joy, B.L.V. Prasad, M. Sastry, Langmuir, 21 (2005) 10638-10643.

[102] T. Ohmori, H. Takahashi, H. Mametsuka, E. Suzuki, Physical Chemistry Chemical Physics, 2 (2000) 3519-3522.

[103] Y. Yang, H. Ma, J. Zhuang, X. Wang, Inorganic Chemistry, 50 (2011) 10143-10151.

[104] A.S. Arico, P. Bruce, B. Scrosati, J.-M. Tarascon, W. van Schalkwijk, Nat Mater, 4 (2005) 366-377.

[105] A.F. Rebolledo, S. Laurent, M. Calero, A. Villanueva, M. Knobel, J.F. Marco, P. Tartaj, ACS Nano, 4 (2010) 2095-2103.

[106] J. Kim, J.E. Lee, S.H. Lee, J.H. Yu, J.H. Lee, T.G. Park, T. Hyeon, Advanced Materials, 20 (2008) 478-483.

[107] S. Sun, C.B. Murray, D. Weller, L. Folks, A. Moser, Science, 287 (2000) 1989-1992.

[108] T.M. Whitney, P.C. Searson, J.S. Jiang, C.L. Chien, Science, 261 (1993) 1316-1319.

[109] P. Panigrahi, R. Pati, Physical Review B, 76 (2007) 024431.

[110] H. Zeng, R. Skomski, L. Menon, Y. Liu, S. Bandyopadhyay, D.J. Sellmyer, Physical Review B, 65 (2002) 134426.

[111] K. Nielsch, F. Müller, A.P. Li, U. Gösele, Advanced Materials, 12 (2000) 582-586.

[112] Huang, L. Li, X. Luo, Zhu, Li, The Journal of Physical Chemistry C, 112 (2008) 1468-1472.

[113] J.R. Morber, Y. Ding, M.S. Haluska, Y. Li, J.P. Liu, Z.L. Wang, R.L. Snyder, The Journal of Physical Chemistry B, 110 (2006) 21672-21679.

[114] R. Han, W. Li, W. Pan, M. Zhu, D. Zhou, F.S. Li, Scientific reports, 4 (2014) 7493.

[115] A. Fernández-Pacheco, L. Serrano-Ramón, J.M. Michalik, M.R. Ibarra, J.M. De Teresa, L. O'Brien, D. Petit, J. Lee, R.P. Cowburn, Sci. Rep., 3 (2013).

[116] Y. Cudennec, A. Lecerf, Journal of Solid State Chemistry, 179 (2006) 716-722.

[117] F. Jiao, J.-C. Jumas, M. Womes, A.V. Chadwick, A. Harrison, P.G. Bruce, Journal of the American Chemical Society, 128 (2006) 12905-12909.

[118] Y.H. Tan, J.A. Davis, K. Fujikawa, N.V. Ganesh, A.V. Demchenko, K.J. Stine, Journal of materials chemistry, 22 (2012) 6733-6745.

[119] D. Ciuculescu, F.d.r. Dumestre, M. Comesaña-Hermo, B. Chaudret, M. Spasova, M. Farle, C. Amiens, Chemistry of Materials, 21 (2009) 3987-3995.

[120] Q. Han, Z. Liu, Y. Xu, H. Zhang, Journal of Crystal Growth, 307 (2007) 483-489.

[121] C. Terrier, M. Abid, C. Arm, S. Serrano-Guisan, L. Gravier, J.P. Ansermet, Journal of Applied Physics, 98 (2005) 086102.

[122] L. Mohaddes-Ardabili, H. Zheng, S.B. Ogale, B. Hannoyer, W. Tian, J. Wang, S.E. Lofland, S.R. Shinde, T. Zhao, Y. Jia, L. Salamanca-Riba, D.G. Schlom, M. Wuttig, R. Ramesh, Nat Mater, 3 (2004) 533-538.

[123] Y. Soumare, C. Garcia, T. Maurer, G. Chaboussant, F. Ott, F. Fiévet, J.-Y. Piquemal, G. Viau, Advanced Functional Materials, 19 (2009) 1971-1977.

[124] W.-S. Lin, H.-M. Lin, H.-H. Chen, Y.-K. Hwu, Y.-J. Chiou, Journal of Nanomaterials, 2013 (2013) 6.

[125] K. Ait Atmane, F. Zighem, Y. Soumare, M. Ibrahim, R. Boubekri, T. Maurer, J. Margueritat, J.-Y. Piquemal, F. Ott, G. Chaboussant, F. Schoenstein, N. Jouini, G. Viau, Journal of Solid State Chemistry, 197 (2013) 297-303.

[126] Y. Soumare, A. Dakhlaoui-Omrani, F. Schoenstein, S. Mercone, G. Viau, N. Jouini, Solid State Communications, 151 (2011) 284-288.

[127] N. Chakroune, G. Viau, C. Ricolleau, F. Fievet-Vincent, F. Fievet, Journal of materials chemistry, 13 (2003) 312-318.

[128] M. Almasi Kashi, A. Ramazani, S. Doudafkan, A.S. Esmaeily, Appl. Phys. A, 102 (2011) 761-764.

[129] X.J. Luo, W.B. Xia, J.L. Gao, S.Y. Zhang, Y.L. Li, S.L. Tang, Y.W. Du, Journal of Applied Physics, 113 (2013) 17B908.

[130] L. Li, Journal of Applied Physics, 79 (1996) 4578-4580.

[131] L.M. A, S.B. A, Y.L. B, H.Z. C, D.J. Sellmyerc, Journal of Nanoscience and Nanotechnology, 1 (2001) 149-152.

[132] P.S. Fodor, G.M. Tsoi, L.E. Wenger, Journal of Applied Physics, 91 (2002) 8186-8188.

[133] S.L. Tang, W. Chen, M. Lu, S.G. Yang, F.M. Zhang, Y.W. Du, Chemical Physics Letters, 384 (2004) 1-4.

[134] S. Alikhanzadeh-Arani, M. Almasi-Kashi, A. Ramazani, Current Applied Physics, 13 (2013) 664-669.

[135] G.H. Yue, L.S. Wang, X. Wang, Y.Z. Chen, D.L. Peng, Journal of Applied Physics, 105 (2009) 074312.

[136] D.-H. Qin, Y. Peng, L. Cao, H.-L. Li, Chemical Physics Letters, 374 (2003) 661-666.

[137] G.H. Lee, S.H. Huh, J.W. Jeong, S.H. Kim, B.J. Choi, H.-C. Ri, B. Kim, J.H. Park, Journal of Applied Physics, 94 (2003) 4179-4183.

[138] M. Wen, X. Meng, B. Sun, Q. Wu, X. Chai, Inorganic Chemistry, 50 (2011) 9393-9399.

[139] S. Thongmee, H.L. Pang, J. Ding, J.Y. Lin, Journal of Magnetism and Magnetic Materials, 321 (2009) 2712-2716.

[140] P.S. Nair, K.P. Fritz, G.D. Scholes, Small, 3 (2007) 481-487.

[141] Y. Bao, W. An, C.H. Turner, K.M. Krishnan, Langmuir, 26 (2010) 478-483.

[142] V.F. Puntes, K.M. Krishnan, A.P. Alivisatos, Science, 291 (2001) 2115-2117.

[143] H.W. Jamie, C. Huaqiang, Nanotechnology, 19 (2008) 305605.

[144] Y. Xia, Y. Xiong, B. Lim, S.E. Skrabalak, Angewandte Chemie International Edition, 48 (2009) 60-103.

[145] V. Privman, D.V. Goia, J. Park, E. Matijević, Journal of Colloid and Interface Science, 213 (1999) 36-45.

[146] M.P. Morales, S. Veintemillas-Verdaguer, M.I. Montero, C.J. Serna, A. Roig, L. Casas, B. Martínez, F. Sandiumenge, Chemistry of Materials, 11 (1999) 3058-3064.

[147] A. Azizi, S.K. Sadrnezhaad, A. Hasani, Journal of Magnetism and Magnetic Materials, 322 (2010) 3551-3554.

[148] W.O. Rosa, L.G. Vivas, K.R. Pirota, A. Asenjo, M. Vázquez, Journal of Magnetism and Magnetic Materials, 324 (2012) 3679-3682.

[149] X.-Z. Li, X.-W. Wei, Y. Ye, Materials Letters, 63 (2009) 578-580.

[150] Z. Zhang, D.A. Blom, Z. Gai, J.R. Thompson, J. Shen, S. Dai, Journal of the American Chemical Society, 125 (2003) 7528-7529.

[151] M. Hu, B. Lin, S. Yu, Nano Res., 1 (2008) 303-313.

[152] L.-P. Zhu, H.-M. Xiao, S.-Y. Fu, European Journal of Inorganic Chemistry, 2007 (2007) 3947-3951.

[153] P.-C. Chang, Z. Fan, D. Wang, W.-Y. Tseng, W.-A. Chiou, J. Hong, J.G. Lu, Chemistry of Materials, 16 (2004) 5133-5137.

[154] D.-E. Zhang, X.-M. Ni, X.-J. Zhang, H.-G. Zheng, Journal of Magnetism and Magnetic Materials, 302 (2006) 290-293.

[155] Q. Liu, X. Guo, T. Wang, Y. Li, W. Shen, Materials Letters, 64 (2010) 1271-1274.

[156] D. Ung, Y. Soumare, N. Chakroune, G. Viau, M.J. Vaulay, V. Richard, F. Fiévet, Chemistry of Materials, 19 (2007) 2084-2094.

[157] D. Ung, G. Viau, C. Ricolleau, F. Warmont, P. Gredin, F. Fiévet, Advanced Materials, 17 (2005) 338-344.

[158] Y. Lee, C. Park, H. Choi, B. Koo, C. Lee, Met. Mater. Int., 14 (2008) 117-121.

[159] S. Kulkarni, M. Alurkar, A. Kumar, Applied Catalysis A: General, 142 (1996) 243-254.

[160] K.-S. Cho, D.V. Talapin, W. Gaschler, C.B. Murray, Journal of the American Chemical Society, 127 (2005) 7140-7147.

[161] M. Pousthomis, E. Anagnostopoulou, I. Panagiotopoulos, R. Boubekri, W. Fang, F. Ott, K. Atmane, J.-Y. Piquemal, L.-M. Lacroix, G. Viau, Nano Res., 8 (2015) 2231-2241.

[162] I. Panagiotopoulos, W. Fang, F. Ott, F. Boué, K. Aït-Atmane, J.-Y. Piquemal, G. Viau, Journal of Applied Physics, 114 (2013) 143902.

[163] F. Ono, Journal of the Physical Society of Japan, 50 (1981) 2564-2572.

[164] M. Feygenson, Y. Yiu, A. Kou, K.-S. Kim, M.C. Aronson, Physical Review B, 81 (2010) 195445.

[165] M.P. Proenca, C.T. Sousa, A.M. Pereira, P.B. Tavares, J. Ventura, M. Vazquez, J.P. Araujo, Physical Chemistry Chemical Physics, 13 (2011) 9561-9567.

[166] S. Chandra, H. Khurshid, M.-H. Phan, H. Srikanth, Applied Physics Letters, 101 (2012) 232405.

[167] S. Maat, K. Takano, S.S.P. Parkin, E.E. Fullerton, Physical Review Letters, 87 (2001) 087202.

[168] A.K. Suszka, O. Idigoras, E. Nikulina, A. Chuvilin, A. Berger, Physical Review Letters, 109 (2012).

[169] F. Radu, M. Etzkorn, R. Siebrecht, T. Schmitte, K. Westerholt, H. Zabel, Physical Review B, 67 (2003) 134409.

[170] D. Tripathy, A.O. Adeyeye, N. Singh, R.L. Stamps, Nanotechnology, 20 (2009) 015304.

[171] S. Laureti, S.Y. Suck, H. Haas, E. Prestat, O. Bourgeois, D. Givord, Physical Review Letters, 108 (2012) 077205.

[172] D. Tripathy, A.O. Adeyeye, K. Chakrabarti, N. Singh, Journal of Applied Physics, 107 (2010) 09D705.

[173] T. Maurer, F. Zighem, F. Ott, G. Chaboussant, G. André, Y. Soumare, J.-Y. Piquemal, G. Viau, C. Gatel, Physical Review B, 80 (2009) 064427.

[174] M.P. Proenca, J. Ventura, C.T. Sousa, M. Vazquez, J.P. Araujo, Physical Review B, 87 (2013) 134404.

[175] O. Kazakova, B. Daly, J.D. Holmes, Physical Review B, 74 (2006).

[176] H.C. Choi, Y.M. Jung, I. Noda, S.B. Kim, The Journal of Physical Chemistry B, 107 (2003) 5806-5811.

[177] J.B. Yi, J. Ding, Journal of Magnetism and Magnetic Materials, 303 (2006) e160-e164.

[178] C. Leighton, M.R. Fitzsimmons, A. Hoffmann, J. Dura, C.F. Majkrzak, M.S. Lund, I.K. Schuller, Physical Review B, 65 (2002).

[179] I.N. Krivorotov, H. Yan, E. Dan Dahlberg, A. Stein, Journal of Magnetism and Magnetic Materials, 226–230, Part 2 (2001) 1800-1802.

[180] H.-C. Hsu, C.-C. Lo, Y.-C. Tseng, Journal of Applied Physics, 111 (2012) 063919.

[181] S. Liébana-Viñas, U. Wiedwald, A. Elsukova, J. Perl, B. Zingsem, A.S. Semisalova, V. Salgueiriño, M. Spasova, M. Farle, Chemistry of Materials, 27 (2015) 4015-4022.

[182] K. Takano, R.H. Kodama, A.E. Berkowitz, W. Cao, G. Thomas, Physical Review Letters, 79 (1997) 1130-1133.

[183] T. Ambrose, R.L. Sommer, C.L. Chien, Physical Review B, 56 (1997) 83-86.

[184] W. Jauch, M. Reehuis, H.J. Bleif, F. Kubanek, P. Pattison, Physical Review B, 64 (2001).

[185] W. Jauch, M. Reehuis, Physical Review B, 65 (2002) 125111.

Biographical Information

Kinjal Gandha earned her B. S. degree in Physics at Sardar Patel University, Vallabh Vidyanagar, Gujarat, India in 2005. She completed her M. S. in 2007 at Sardar Patel University, Gujarat, India. She started her PhD studies with Prof. J. Ping Liu at University of Texas at Arlington in 2011. Her thesis research was focused on the Synthesis and Magnetic Properties of High-Aspect Ratio Nanocrystals. She is the author of 6 papers (4 published, 2 submitted). She received a college of science dissertation fellowship award from University of Texas at Arlington in 2015. She wants to explore and contribute more in this area while pursuing her career in a related field.